

PATIENT DOSES AND IMAGE QUALITY
IN INTERVENTIONAL NEURORADIOLOGY

By

NIKOLAOS A. GKANATSIOS

A DISSERTATION PRESENTED TO THE GRADUATE SCHOOL
OF THE UNIVERSITY OF FLORIDA IN PARTIAL FULFILLMENT
OF THE REQUIREMENTS FOR THE DEGREE OF
DOCTOR OF PHILOSOPHY

UNIVERSITY OF FLORIDA

1998

ACKNOWLEDGEMENTS

I would like to gratefully acknowledge the following who have helped me throughout my graduate work:

- Dr. Walter Huda, my advisor, for his invaluable guidance, time and patience throughout the course of this research and the preparation of this dissertation. I am very grateful for his continuous advice and suggestions throughout my graduate work.
- My Ph.D. committee members, Prof. James S. Tulenko, Dr. Wesley E. Bolch, Dr. Janice C. Honeyman, Dr Keith R. Peters and Dr. Irvine F. Hawkins, for reviewing my progress and guiding me through my Ph.D. research.
- Ms. Lynn Rill, for her valuable time evaluating all the radiographic images and for her review and comments on the manuscript.
- Mr. Dennis Pinner from Toshiba America Medical Systems, for his valuable insights into understanding the imaging equipment and for providing me with the requested information and documentation on the imaging system.
- The Department of Radiology, for giving me the graduate assistantship to pursue my graduate studies, and for all the resources they made available for me throughout my graduate research.
- My beloved parents, Anastasia and Argyrios Gkanatsios, for their love, encouragement, and support throughout all my endeavors. They are the ones who made this possible for me.

TABLE OF CONTENTS

| | |
|---|------|
| ACKNOWLEDGEMENTS | ii |
| LIST OF TABLES | vi |
| LIST OF FIGURES | viii |
| ABSTRACT | xi |
| CHAPTERS | |
| 1 INTRODUCTION | 1 |
| Interventional Neuroradiology | 1 |
| Patient Dosimetry | 2 |
| Dose Monitoring Systems | 4 |
| Image Quality | 5 |
| Purpose of This Work | 6 |
| 2 LITERATURE REVIEW | 8 |
| Introduction | 8 |
| Interventional Neuroradiologic Procedures | 8 |
| Deterministic Radiation Effects | 9 |
| Stochastic Radiation Effects | 12 |
| Dosimetry | 13 |
| Surface Dose | 13 |
| Energy Imparted | 15 |
| Effective Dose | 18 |
| Image Quality | 21 |
| Image Contrast | 21 |
| Image Noise | 23 |
| Spatial Resolution | 26 |
| Imaging Technique Factors | 27 |
| Tube Potential | 28 |
| Input Exposure to the Image Receptor | 29 |
| Magnification | 30 |
| 3 SURFACE DOSES | 32 |

| | |
|---|-----------|
| Neuroradiologic Imaging..... | 32 |
| Clinical Practice..... | 32 |
| Imaging Equipment | 33 |
| Operation..... | 35 |
| Imaging Techniques | 36 |
| The Patient Dosimetry System | 38 |
| System Description..... | 38 |
| Calibration | 40 |
| Evaluation..... | 42 |
| Data Acquisition..... | 45 |
| Fluoroscopy | 47 |
| X-Ray Beam Localization | 47 |
| Surface Doses | 48 |
| Surface Dose Rates..... | 49 |
| Fluoroscopic Times and Intervals..... | 51 |
| Radiography..... | 53 |
| X-Ray Beam Localization | 53 |
| Surface Doses | 54 |
| Surface Dose Rates..... | 54 |
| Radiographic Frames..... | 56 |
| Conclusions..... | 57 |
| 4 ENERGY IMPARTED AND EFFECTIVE DOSE IN NEURORADIOLOGY | 60 |
| Introduction..... | 60 |
| Method..... | 62 |
| Energy Imparted | 62 |
| Adult Effective Doses..... | 66 |
| Pediatric Effective Dose | 69 |
| Adult Patient Doses | 71 |
| Energy Imparted | 71 |
| Effective Doses..... | 74 |
| Pediatric Patient Doses | 75 |
| Energy Imparted | 76 |
| Effective Doses..... | 79 |
| Discussion..... | 80 |
| Conclusions..... | 83 |
| 5 IMAGE QUALITY..... | 86 |
| Image Acquisition..... | 86 |
| Phantom Description | 86 |
| Acquisition of Digitally Subtracted Images | 88 |
| Dosimetry and Image Quality..... | 94 |
| Dosimetry | 94 |
| Image Quality Evaluation..... | 95 |
| Precision of Measurements..... | 96 |

| | |
|--|-----|
| Results..... | 97 |
| Tube Voltage | 97 |
| Image Intensifier Input Exposure | 100 |
| Geometric Object Magnification | 102 |
| Discussion..... | 107 |
| Patient Surface Dose..... | 107 |
| Energy Imparted | 110 |
| Image Quality | 113 |
| Conclusions..... | 114 |
| 6 CONCLUSIONS | 116 |
| Patient Dosimetry | 116 |
| Surface Doses | 116 |
| Effective Doses..... | 117 |
| Image Quality | 119 |
| Future Work..... | 120 |
| BIBLIOGRAPHY | 122 |
| BIOGRAPHICAL SCHETCH..... | 131 |

LIST OF TABLES

| <u>Table</u> | <u>page</u> |
|--|-------------|
| 2-1. Deterministic Effects of the Skin after Single-Fraction Irradiation | 11 |
| 3-1. List of the Input Signals Interfaced to the PEMNET Dosimetry System from the Toshiba Neurobiplane Imaging Unit..... | 40 |
| 3-2. Experimental Arrangements for Evaluating the Patient Dosimetry System..... | 44 |
| 3-3. Summary of the Ratios of the Measured to Calculated Surface Doses, X_M/X_C , Obtained During Testing of the Accuracy of the Patient Exposure System | 45 |
| 4-1. Computed α and β Coefficients and Half-Value Layers for X-Ray Beams as a Function of Tube Voltage | 64 |
| 4-2. Backscatter Fractions of Radiation Exposure at Different Tube Voltages | 65 |
| 4-3. Patient Thickness and Area of Exposure Corresponding to the Head Region of Different Age Groups | 66 |
| 4-4. Patient Thickness and Area of Exposure Corresponding to the Trunk Region of Different Age Groups | 67 |
| 4-5. Values of Effective Dose per Unit Energy Imparted, E/ε in mJ/Sv, for Different Body Projections as a Function of Tube Voltage..... | 70 |
| 4-6. Standard Patient Mass for Different Age Groups | 70 |
| 5-1. Iodine Contrast Concentration in Each Vessel of the Vessel Insert | 89 |
| 5-2. Imaging Techniques During Tube Voltage Experiments | 92 |
| 5-3. Imaging Techniques During Geometric Object Magnification Experiments | 93 |
| 5-4. Score Describing the Visibility of Each Iodine Contrast Concentration | 95 |
| 5-5. Tube Voltage Dependency at 120 μ R/frame | 98 |
| 5-6. Tube Voltage Dependency at 440 μ R/frame | 98 |

| | | |
|-------|--|-----|
| 5-7. | Image Intensifier Input Exposure Dependency..... | 102 |
| 5-8. | Geometric Object Magnification Dependency at 120 $\mu\text{R}/\text{frame}$ | 104 |
| 5-9. | Geometric Object Magnification Dependency at 440 $\mu\text{R}/\text{frame}$ | 104 |
| 5-10. | Comparison of the Effects of Tube Voltage, Input Exposure and Geometric Magnification on the Surface Dose for a Range of Changes in Threshold Iodine Concentration at 120 $\mu\text{R}/\text{frame}$ | 108 |
| 5-11. | Comparison of the Effects of Tube Voltage, Input Exposure and Geometric Magnification on the Surface Dose for a Range of Changes in Threshold Iodine Concentration at 440 $\mu\text{R}/\text{frame}$ | 108 |
| 5-12. | Comparison of the Effects of Tube Voltage, Input Exposure and Geometric Magnification on the Energy Imparted for a Range of Changes in Threshold Iodine Concentration at Low Input Exposures | 111 |
| 5-13. | Comparison of the Effects of Tube Voltage, Input Exposure and Geometric Magnification on the Energy Imparted for a Range of Changes in Threshold Iodine Concentration at High Input Exposures..... | 111 |

LIST OF FIGURES

| <u>Figure</u> | <u>page</u> |
|---|-------------|
| 1-1. Unsubtracted image (left) where anatomical details are mixed with diagnostic information. Digitally subtracted angiogram (right) where anatomical information has been subtracted to allow easier visualization of vasculature. | 2 |
| 2-1. Key parameters that affect patient dose and image quality in x-ray imaging. | 28 |
| 3-1. Histogram of surface dose contribution at different x-ray tube voltages from frontal plane (black bars) and lateral plane (gray bars) fluoroscopy for an average interventional neuroradiologic procedure. | 37 |
| 3-2. Histogram of surface dose contribution at different x-ray tube voltages from frontal plane (black bars) and lateral plane (gray bars) radiography for an average interventional neuroradiologic procedure. | 38 |
| 3-3. Calibration setup of the frontal plane (left) and lateral plane (right) using an RSD RS-235 anthropomorphic head phantom. | 42 |
| 3-4. Sample page from the PEMNET database showing all recorded information for the frontal imaging plane. | 46 |
| 3-5. Histogram distribution of surface doses for 175 patients from frontal plane (black bars) and lateral plane (gray bars) fluoroscopy. | 49 |
| 3-6. Histogram distribution of surface dose rates for 175 patients from frontal plane (black bars) and lateral plane (gray bars) fluoroscopy. | 50 |
| 3-7. Histogram distribution of fluoroscopic times to 175 patients from frontal plane (black bars) and later plane (gray bars) fluoroscopy. | 52 |
| 3-8. Histogram distribution of fluoroscopic intervals for 175 patients from frontal plane (black bars) and lateral plane (gray bars) fluoroscopy. | 53 |
| 3-9. Histogram distribution of surface doses for 175 patients from frontal plane (black bars) and lateral plane (gray bars) radiography. | 55 |
| 3-10. Histogram distribution of surface dose rates for 175 patients from frontal plane (black bars) and lateral plane (gray bars) radiography. | 56 |

| | | |
|-------|---|----|
| 3-11. | Histogram distribution of the number of radiographic frames for 175 patients from frontal plane (black bars) and lateral plane (gray bars) radiography..... | 57 |
| 3-12. | Histogram distribution of the total surface doses to 175 patients from frontal plane (black bars) and later plane (gray bars) fluoroscopy and radiography combined..... | 59 |
| 4-1. | Values of ω as a function of water phantom thickness for tube voltages of 60 kVp, 80 kVp and 100 kVp. | 63 |
| 4-2. | Effective dose as a function of patient mass for one joule of uniform whole body irradiation. | 71 |
| 4-3. | Histogram distribution of energy imparted to patients from use of fluoroscopy during interventional neuroradiologic procedures. | 72 |
| 4-4. | Histogram distribution of energy imparted to patients from radiographic acquisitions during interventional neuroradiologic procedures. | 73 |
| 4-5. | Histogram distribution of the total energy imparted to patients undergoing diagnostic angiographic and therapeutic embolization neuroradiologic procedures. | 75 |
| 4-6. | Histogram distribution of the total effective dose to patients from biplane neuroradiologic examinations. | 76 |
| 4-7. | Energy imparted as a function of patient mass from fluoroscopy during interventional neuroradiologic procedures on pediatric patients. Line shows the linear fit between energy imparted and patient mass. | 77 |
| 4-8. | Energy imparted as a function of patient mass from radiographic acquisitions during interventional neuroradiologic procedures on pediatric patients. Line shows the linear fit between energy imparted and patient mass. | 78 |
| 4-9. | Energy imparted as a function of patient mass from interventional neuroradiologic procedures on pediatric patients. Line shows the linear fit between energy imparted and patient mass. | 79 |
| 4-10. | Effective dose as a function of patient mass from interventional neuroradiologic procedures on pediatric patients. Line shows the linear fit between effective dose and patient mass. | 80 |
| 4-11. | Comparison of E/ϵ values vs. patient age as determined by Equation (4.4) and by using the dosimetry data from Hart et al. (1996a). | 84 |
| 5-1. | Schematic diagram of the acrylic phantom with the <i>vessel</i> and <i>blank</i> inserts used to simulate small vessels for the purpose of evaluating image quality in neuroradiology. | 87 |

| | | |
|-------|---|-----|
| 5-2. | Experimental setup for DSA acquisitions..... | 90 |
| 5-3. | Position of the two ionization chambers relative to the vessel insert (left). Subtracted image (right). | 90 |
| 5-4. | Surface dose and energy imparted as a function of tube voltage..... | 99 |
| 5-5. | Threshold iodine concentration as a function of tube voltage. The circles correspond to the 120 $\mu\text{R}/\text{frame}$ and have been fitted to $kVp^{2.07}$. The squares correspond to the 440 $\mu\text{R}/\text{frame}$ and have been fitted to $kVp^{1.56}$ | 100 |
| 5-6. | Surface dose and energy imparted as a function of image intensifier input exposure at 70 kVp. | 101 |
| 5-7. | Threshold iodine concentration as a function of image intensifier input exposure for a constant video level at 70 kVp..... | 103 |
| 5-8. | Surface dose and energy imparted as a function of image intensifier input exposure at 70 kVp. | 105 |
| 5-9. | Threshold iodine concentration as a function of geometric object magnification at 70 kVp..... | 106 |
| 5-10. | Change in surface dose versus change in threshold iodine concentration with tube voltage input exposure and magnification. | 109 |
| 5-11. | Change in energy imparted versus change in threshold iodine concentration with tube voltage input exposure and magnification. | 112 |

Abstract of Dissertation Presented to the Graduate School
of the University of Florida in Partial Fulfillment of the
Requirements for the Degree of Doctor of Philosophy

PATIENT DOSES AND IMAGE QUALITY
IN INTERVENTIONAL NEURORADIOLOGY

By

Nikolaos A. Gkanatsios

December, 1998

Chairman: James S. Tulenko

Cochairman: Walter Huda

Major Department: Nuclear and Radiological Engineering

Diagnostic and therapeutic interventional neuroradiologic procedures involve imaging of catheter manipulation and vascular anomalies of the brain and generally require extensive use of x-ray radiation. Knowledge of the surface dose allows one to estimate the probability of inducing deterministic effects, whereas the corresponding value of effective dose is related to the patient stochastic risk. Modification of key imaging parameters (i.e., tube voltage, input exposure to the image receptor and geometric magnification) impact on patient doses and image quality, with the latter being defined as the lowest concentration of iodine in a vessel that may be visually detected in the radiographic image. A dosimetry system was installed on a biplane neuroradiologic imaging system to determine the doses to patients undergoing interventional neuroradiologic procedures. The dosimetry system computed surface doses on the basis of selected technique factors and information about patient location relative to the x-ray

tube. The energy imparted to the patient, ϵ , was determined using the surface dose, x-ray beam quality (i.e., kVp and HVL), exposure area and thickness of the patient and was converted into the corresponding value of effective dose, E . Values of surface dose and E were obtained for 175 patients, consisting of 149 adults and 26 pediatrics. Median values of surface doses to the head region were 1.2 Gy in the frontal plane and 0.62 Gy in the lateral plane. Median values of the effective doses were 36 mSv for adult patients and 44 mSv for pediatric patients. An acrylic phantom with 1-mm diameter vessels filled with iodine contrast was used to evaluate the effects of varying imaging parameters on signal detection and patient doses during digital subtraction angiography. Reducing the x-ray tube voltage offered the largest improvement in image quality for a given increase in patient dose. Increasing the image intensifier input exposure beyond 250 $\mu\text{R}/\text{frame}$ provided very little improvement in image quality, and this II exposure level should not be exceeded in interventional neuroradiologic imaging. A linear relationship was observed between magnification and threshold concentration, which offers significant patient benefits when surface doses are not expected to exceed the threshold doses for the induction of deterministic effects.

CHAPTER 1 INTRODUCTION

Interventional Neuroradiology

Neuroradiology is a multi-imaging science, which utilizes all imaging modalities (i.e., plain film, digital radiography, computed tomography, magnetic resonance imaging, nuclear medicine, etc) to accomplish a complete diagnosis of human neurology. Neuroradiology can be distinguished as *conventional* or *interventional* neuroradiology. Conventional neuroradiology uses modalities such as plain film radiography, computed tomography (CT), magnetic resonance imaging (MRI) and ultrasound (US) to diagnose neurologic abnormalities. Interventional neuroradiology studies the vasculature and blood kinetics of the brain by means of catheterization performed with the transfemoral artery technique. Interventional neuroradiologic procedures can be further distinguished as *diagnostic angiographic* or *therapeutic embolization* procedures. The imaging portion of any interventional neuroradiologic procedure is accomplished by use of digital subtraction angiography (DSA). In digital subtraction angiography, a mask image is being subtracted from an image enhanced with injected iodinated contrast to isolate vasculature structures from the rest of the anatomy as shown in Figure 1-1.

Interventional neuroradiologic procedures often involve long fluoroscopic exposure times and the acquisition of a large number of radiographic images. As a result, there is a possibility of induction of deterministic radiation effects such as skin erythema and epilation. It is also important to determine the stochastic risks involved in such

procedures in both adult and pediatric patients. Modification of key imaging parameters (i.e., tube voltage, input exposure to the image receptor and geometric magnification) impact on image quality and patient doses from interventional neuroradiologic procedures. The effects of these parameters on image quality and patient doses should be quantified and optimized in order to ensure adequate diagnostic image quality and reduced patient doses.

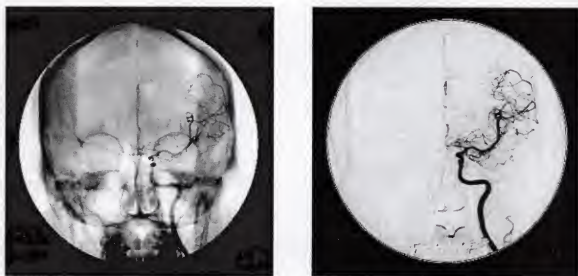


FIGURE 1-1: Unsubtracted image (left) where anatomical details are mixed with diagnostic information. Digitally subtracted angiogram (right) where anatomical information has been subtracted to allow easier visualization of vasculature.

Patient Dosimetry

The surface dose is the dosimetric quantity that measures the dose absorbed in the surface of an irradiated region from radiation exposures. The surface dose accounts for the energy absorbed in the skin and can predict the possibility of inducing deterministic injuries from high dose interventional radiologic procedures (i.e., cardiac catheterization, abdominal interventional or neurointerventional procedures). Deterministic injuries

associated with interventional neuroradiologic procedures primarily consist of injuries induced to the skin of the patient such as skin erythemas and epilations. Knowledge of surface doses may also provide information on the probability of deterministic injuries to the lens of the eye from interventional neuroradiologic procedures.

The effective dose, E , is a dosimetric parameter, which takes into account the doses received by all irradiated radiosensitive organs. The effective dose is able to account for nonuniform irradiation of different organs and tissues in the body and can be used as an indicator of the stochastic radiation risk associated with radiologic x-ray examinations. Determining effective doses for radiologic examinations by measurement or calculation is generally very difficult. By contrast, the energy imparted, ϵ , to the patient may be obtained from the x-ray exposure-area product incident on the patient. As energy imparted is approximately proportional to the effective dose for any given x-ray radiographic view, the availability of E/ϵ ratios (Huda and Gkanatsios, 1997) for common radiographic projections provides a convenient way for estimating effective doses. Such ratios primarily depend on the projection employed (body region irradiated and x-ray beam orientation) and secondarily on the tube potential and beam filtration.

The effective dose as a dose descriptor in diagnostic radiology enables a direct comparison of the detriment associated with different radiologic procedures. Expressing patient doses in terms of the effective dose provides a consistent method of reporting doses from diagnostic radiologic examinations. Effective doses in interventional neuroradiology can simply be compared to other radiologic doses (i.e., computed tomography, nuclear medicine, cardiac catheterization procedures, etc.). The use of the effective dose also permits an estimate of patient risk to be obtained by using current

stochastic risk factors (ICRP, 1991; UNSCEAR, 1993; NAS, 1990). Use of such stochastic risk factors with the effective doses computed for interventional neuroradiologic procedures will provide useful information on the stochastic risks to patients undergoing such high dose procedures.

Dose Monitoring Systems

A radiation monitoring system which provides feedback of dosimetric information could play a role in ensuring that patient exposures are as low as reasonably achievable (ALARA, ICRP, 1982). The benefits of a radiation monitoring system include identification of individual patients who may be at risk for the induction of deterministic radiation effects (Wagner *et al.*, 1994), provision of a formal record of the patient exposure as well as an increase in the radiologist's awareness of potential high patient doses. In addition, the radiation monitoring system can serve as a powerful tool to empirically investigate the tradeoffs between patient dose and corresponding image quality when radiographing appropriate phantoms.

Use of modern on-line dosimetry systems on today's advanced x-ray imaging equipment provides the necessary tools for fast and accurate acquisition of dosimetry data on patients undergoing complex radiologic procedures. A patient dosimetry system (PEMNET*) was installed in 1995 in the neuroradiology suite at the Department of Radiology at Shands Hospital of the University of Florida. The patient dosimetry system monitored both frontal and lateral imaging planes and recorded the amount of radiation

* Clinical Microsystems, Arlington, VA

received by patients undergoing interventional neuroradiologic procedures along with additional dosimetric information to help to compute effective doses.

Image Quality

The purpose of any radiographic image (analog or digital) is to provide the observer with adequate diagnostic information to detect and identify or rule out an abnormality and then to interpret its meaning and determine its cause. The ability of a radiographic image to convey this information to the observer depends on the quality of the image, which can be described in terms of contrast, noise and resolution. Image quality is very critical in interventional neuroradiologic procedures. The ability to visualize small and low contrast objects is of paramount importance, where neurovascular instruments may be as small as 200 μm and where vessel sizes are as small as 100 μm . The produced images require high contrast, low noise and high resolution, which can be achieved with high radiation doses. Any dose reduction strategy must always ensure that image quality is not compromised and patients do not suffer any adverse clinical consequences as a result of inadequate visualization of catheters or vasculature.

Ways to improve detection of small vessels during interventional neuroradiologic procedures using digital subtraction angiography (DSA) include the variation of major imaging parameters such as tube voltage and image intensifier input exposure, as well as use of geometric object magnification. Although these parameters affect image quality, they also influence patient surface doses and effective doses. Further study is necessary to improve our understanding of how technique parameters affect patient doses and to what extent they can improve image quality.

Purpose of This Work

Following the installation of the patient dosimetry system on the interventional neurobiplane suite at Shands Hospital of the University of Florida, dosimetry data on patients undergoing interventional neuroradiologic procedures were stored in a patient database for later analysis and evaluation. Dosimetric information on 149 adult patients and 26 pediatric patients who underwent interventional neuroradiologic procedures was recorded in the database. Seventeen of 149 adult patients and ten of the 26 pediatric patients recorded in the database underwent therapeutic embolization procedures.

In this work, the dosimetry data to the adult and pediatric patients recorded by the patient dosimetry system are analyzed to compute surface doses to the patients' head region from interventional neuroradiologic procedures. Surface doses are then considered to assess the risk of deterministic effects to patients who undergo such interventional procedures, as well as similar high dose radiologic procedures.

Information on the x-ray beam qualities (kVp and HVL) recorded by the patient dosimetry system with patient thickness and the x-ray beam exposure area are used to compute the energy imparted to these patients from recorded values of entrance skin exposures. Values of energy imparted are then converted to patient effective dose, E , using E/ϵ conversion factor corresponding to the projections and body regions irradiated during interventional neuroradiologic procedures. Values of E/ϵ for the postero-anterior (PA) projections of the abdomen, chest and cervical spine and for the PA and lateral (LAT) views of the head are obtained from radiation dosimetry data computed using Monte Carlo calculations on an adult anthropomorphic phantom (Hart *et al.*, 1994a).

This method is extended to determine effective doses to pediatric patients who differ in mass from the adult sized phantoms used in current patient dose assessment procedures.

Manipulation of the tube voltage, input exposure to the image receptor and geometric object magnification impact on patient doses and image quality, with the latter being defined as the lowest concentration of iodine in a vessel that may be visually detected in the radiographic image. The effects of these imaging parameters on signal detection and the corresponding changes in patient doses are investigated in this work.

The results of this work provide the radiologic community with a variety of information on patient surface doses, energy imparted and effective doses. Such information will help to evaluate the risks of deterministic and stochastic effects to patients undergoing interventional neuroradiologic or similar high dose radiologic procedures. The results on how imaging parameters (i.e., tube voltage, image intensifier input exposure and geometric object magnification) affect image quality will help to improve image quality and reduce patient doses, thus providing improved patient care to the healthcare community.

CHAPTER 2 LITERATURE REVIEW

Introduction

Interventional Neuroradiologic Procedures

During diagnostic neuroradiologic procedures, all initial angiograms performed on a given vessel territory constitute complete coverage of arterial, capillary and venous phases. Subsequent examinations of that vessel with various alterations in positioning (projection), magnification, and contrast injection are performed to specifically evaluate the visualized or anticipated pathology. As a result, these are limited to arterial phase for aneurysms, capillary phase for tumors, and venous phase for study of venous patency. In therapeutic neuroradiologic procedures, a complete diagnostic angiographic procedure is followed by the introduction of embolic agents into the vasculature from a location next to the vascular abnormality. Such embolic agents might consist of gelatin sponge or polyvinyl alcohol for short-term occlusions or detachable balloons, metallic coils and cyanoacrylates for long-term occlusions. Subsequent evaluation of the pathology during embolization continues until a satisfactory occlusion of the vascular abnormality has been achieved.

During all neuroradiologic procedures, frontal fluoroscopy is used in the truncal and thoracic regions to visualize catheter placement. Biplane fluoroscopy of the head

region is used for target position verification. Most DSA image acquisitions are performed using biplane acquisitions with only occasional use of single plane acquisitions. Single (frontal) plane imaging is primarily used to evaluate aneurysm neck origin with either standard DSA imaging or with rotational digital angiography (DA). Due to the nature of neuroradiologic procedures, good image quality, long fluoroscopic times and a significant number of angiographic images are required to evaluate any visualized pathology. Thus, neuroradiologic procedures result in high patient doses, primarily absorbed over the head region of the patient. This suggests the possibility of induction of deterministic radiation effects such as skin erythema and epilation (Huda and Peters, 1994; Shope, 1996).

Deterministic Radiation Effects

Deterministic or non-stochastic effects of ionizing radiation include the types of injuries resulting from whole-body or local exposures to radiation that cause sufficient cell damage or cell killing to substantial numbers or proportions of cells to impair function in the irradiated tissues or organs (ICRP, 1977). Since a given number or proportion of cells must be affected, there is a threshold dose below which the number or proportion of cells affected is insufficient for the defined deterministic injury to occur (ICRP, 1984). The threshold dose depends on the level of injury or the sensitivity of the tissues or organs being irradiated (Field and Upton, 1985). Any increase in dose above the threshold increases the level of injury, since fewer cells will survive at increased radiation dose. The effect will also increase with increased dose rate. Increased dose rate

will accelerate cell damage without allowing enough time for more effective cell repair or repopulation (ICRP, 1991).

The doses that result in the clinical appearance of deterministic effects are generally of the order of a few Gray to tens of Gray. The time at which the effect becomes noticeable may range from a few hours to some years after exposure, depending on the type of effect and the characteristics of the irradiated tissue. The levels of radiation exposure and the irradiated tissues involved in interventional neuroradiology raise concern for deterministic effects of the skin and eyes. Table 2-1 lists the skin effects, threshold doses and time of observation of the expected effect after irradiation (Wagner *et al.*, 1994). An early transient erythema may be observed a few hours after irradiation at skin absorbed doses in excess of 2 Gy, with a main erythema appearing about 10 days later, when skin doses exceed 6 Gy. A temporary epilation may be observed three weeks after an absorbed dose of 3 Gy to the skin surface with a permanent condition resulting at doses above 7 Gy. The concern to the eye involves small opacities on the lens of the eye, which may occur at doses of the order of about 1-2 Gy (Merriam and Focht, 1957; NAS, 1990). More severe cases of cataracts occur at thresholds above 5-6 Gy with a latent period of about a year after irradiation.

Deterministic effects will often have a more severe impact on children, since tissues are actively growing in comparison to adults (UNSCEAR, 1993). Additional deterministic effects that have been observed from irradiation during childhood include effects on growth and development, hormonal deficiencies, organ dysfunctions and effects on intellectual and cognitive functions. From current data available (UNSCEAR, 1993), there is no evidence that the threshold of deterministic effects to the skin and eyes

are any different for children or adults. Although the brain is most sensitive to radiation insults during the first four years after birth when rapid growth and development of the brain takes place, single doses in excess of 10 Gy have to be administered to the brain during childhood before any deterministic effect of neurophysiologic or neuroendocrine nature are observed.

TABLE 2-1: Deterministic Effects of the Skin after Single-Fraction Irradiation

| Deterministic Effect | Dose Threshold (Gy) | Onset Time | Peak Time |
|-----------------------------|----------------------------|-------------------|------------------|
| Early transient erythema | 2 | hours | ~24 hours |
| Temporary epilation | 3 | ~3 weeks | -- |
| Main erythema | 6 | ~10 days | ~2 weeks |
| Permanent epilation | 7 | ~3 weeks | -- |
| Dry desquamation | 10 | ~4 weeks | ~5 weeks |
| Invasive fibrosis | 10 | -- | -- |
| Dermal atrophy | 11 | >14 weeks | -- |
| Telangiectasia | 12 | >52 weeks | -- |
| Moist desquamation | 15 | ~4 weeks | ~5 weeks |
| Late erythema | 15 | ~6-10 weeks | -- |
| Dermal necrosis | 18 | >10 weeks | -- |
| Secondary ulceration | 20 | >6 weeks | -- |

SOURCE: Wagner *et al.*, 1994.

Stochastic Radiation Effects

Unlike the deterministic effects, stochastic effects are those for which the probability of an effect occurring is a function of dose without threshold and its severity of the effect is dose-independent (ICRP, 1977). Stochastic effects can be categorized as *somatic* (carcinogenic) effects and *hereditary* (genetic) effects, which may occur from injury to one or a small number of cells. Since a single cell may be enough to initiate the effect, there is a finite probability that the effect will occur however small the dose. Thus, stochastic effects are normally assumed to have no dose threshold below which the effect cannot possibly occur.

Since a stochastic effect may occur at any level of radiation exposure, the exposure should be kept as low as reasonably achievable (ICRP, 1977). Unnecessary exposures should be avoided, necessary exposures should be optimized to provide the maximum benefit to the patient, and the total doses should be limited to the minimum amount consistent with the medical benefit to the individual patient (ICRP, 1982, 1983). In the case of optimizing medical procedures for the best dose-benefit outcome, the main concern should be the amount and type of information derived from the examination and its diagnostic value.

Whole body irradiation or its equivalent as expressed by the effective dose equivalent or effective dose can be converted to a stochastic risk estimate using a total risk factor as determined by the ICRP (1977, 1978, 1991). From the ICRP (1991) attempt to estimate absolute stochastic risks from whole-body irradiation, a risk coefficient of 5×10^{-5} cancers and genetic abnormalities per mSv of radiation dose was derived. Such a risk coefficient puts one out of 20,000 people who received a whole

body dose equivalent of 1 mSv to risk of developing a fatal cancer. This is a more conservative value from the previously derived risk coefficient of 1.65×10^{-5} (ICRP, 1978), where one out of 60,600 people who receive 1 mSv will develop a fatal cancer. In general, these risk factors need to be treated with great caution given the current uncertainties associated with the extrapolation of radiation risks from high doses to those normally encountered in diagnostic radiology (Fry, 1996; Puskin and Nelson, 1996)

Although knowledge of the pediatric effective dose associated with radiologic procedure is helpful, it is important to note that any resultant detriment will depend on the age of the exposed individual. The stochastic radiation risks of carcinogenesis and genetic effects are generally greater for children than for adults to at least a factor of two (ICRP, 1991; NCRP, 1985). These factors would need to be taken into account when converting any pediatric effective doses into a value of risk or detriment. As a result, direct comparisons of pediatric doses with those of adults need to be treated with circumspection.

Dosimetry

Surface Dose

The surface dose is the simplest and most frequent method used to measure patient doses from radiologic examinations because direct measurements on patients can be performed easily at the skin surface. The surface dose can be obtained from measurements of the skin exposure using an ionization chamber or specialized detectors attached to the skin surface during the examination (i.e., thermoluminescent chips,

fiberoptic scintillators). The surface dose may also be converted to organ doses (Jones and Wall, 1985), although such an approach may result in errors of more than 20% (Padovani *et al.*, 1987).

Although simple to obtain, the surface dose is a poor indicator of the true significance of radiation exposure to the patient because it overlooks a number of important factors. For example, in a fluoroscopic exam the surface dose does not account for changes in the depth of the radiosensitive organs, changes in the exposed field size, changes in the position of the patient, and changes in the beam qualities, overlaying exposure fields and partial exposure of organs (Wagner, 1991). More importantly, the surface dose does not account for the area of exposure or the penetrating ability of the x-ray beam as the energy of x-rays varies.

The above factors make surface dose a quantity of limited dosimetric value when estimating stochastic risks. However, the surface dose is the quantity of choice when trying to predict the occurrence of deterministic radiation effects of the skin during high dose interventional radiologic procedures. In this case, the surface dose is the dose to the organ, the skin. Vano *et al.* (1998) measured surface doses of 11-15 Gy resulting in erythematous lesions and chronic radiodermatitis from procedures in interventional cardiology. Huda and Peters (1994) computed an upper estimate of 6.6 Gy to the occipital region of the skull resulting in temporary epilation from an embolization neuroradiologic procedure. Other studies reported a range of surface doses for neurointerventional procedures. Norbash *et al.* (1996) studied twelve typical interventional neuroradiologic procedures and measured a range of 0.31-2.7 Gy to the skin surface of the head with a mean value of 1.5 Gy. Bergeron *et al.* (1994) measured

0.13-1.3 Gy with a mean value of 0.62 Gy for eight patients undergoing neurointerventional procedures. Chopp *et al.* (1980) reported an average surface dose to the head of 0.16 Gy. Gkanatsios *et al.* (1997) measured surface doses to 114 patients undergoing neurointerventional procedures and recorded doses ranging from 0.1-5.0 Gy with median values of 1.2 Gy and 0.64 Gy for the frontal and lateral planes, respectively. Although about 30 patients in the latter study exceeded the deterministic threshold of 2.0 Gy, no radiation-induced skin effects were noticed.

Energy Imparted

Although the surface dose or exposure has been popular when expressing patient radiation doses, these parameter do not take into account the x-ray beam quality (i.e., half-value layer) or the size of the irradiated area. An alternative quantity that can be used to assess patient dosimetry is the energy imparted, or integral dose (Wall *et al.*, 1979; Harrison, 1983; Huda 1984; Cameron 1992). Energy imparted is a measure of the total energy deposited in a volume (i.e., head, chest, abdomen, etc.) from exposure to x rays. The primary factors that affect energy imparted are the x-ray exposure, the area exposed, the energy of the x-ray beam, and the thickness of the exposed volume (Gkanatsios, 1995; Gkanatsios and Huda, 1997). Secondary factors affecting energy imparted are the filtration, the voltage waveform ripple, and the target angle (Shrimpton *et al.*, 1984; Gkanatsios, 1995). Energy imparted may be used to compute the associated risk from different types of radiologic examinations, optimize imaging techniques with respect to patient dose, or even estimate the effective dose to the patient.

The computation of energy imparted can be carried out with accuracy and ease (Carlsson, 1963; Huda, 1984; Shrimpton *et al.*, 1984; Gkanatsios and Huda, 1997). A number of approaches have been developed to obtain values of energy imparted from radiologic procedures (i.e., Carlsson, 1963, 1965a, 1965b; Carlsson *et al.*, 1984; Harrison, 1983; Shrimpton and Wall; 1982). Most methods calculate values of energy imparted from depth dose data or from estimates of the incident energy to the irradiated volume. Energy imparted generally depends on the x-ray beam quality, as well as the field size and irradiation geometry, which makes depth dose data of limited value in the everyday clinical setting. Monte Carlo techniques are another way to compute energy imparted, given that photon interaction cross sections and x-ray energy distributions are well known (Persliden and Carlsson, 1984; Boone 1992). However, these methods are computer intensive, time-consuming, and relatively cumbersome to use. Other simplified methods, such as the use of half-value thickness of tissue (Hummel *et al.*, 1985), also can be used to calculate values of energy imparted. The most practical approach developed to obtain values of energy imparted is the use of transmission ionization chambers, which can generate energy imparted data from an exposure-area, or air collision kerma-area product (Shrimpton *et al.*, 1984). Measurements of exposure-area product have been reported to result in an accuracy of energy imparted between 10% and 20% (Shrimpton *et al.*, 1984; Berthelsen and Caderbland, 1991). However, exposure-area product meters do not take into account patient thickness, and the incident beam may not totally irradiate the patient. Although it may be possible to overcome both these limitations, an accurate and practical method for estimating energy imparted to patients that does not rely on special instrumentation would clearly be advantageous.

Recently, Gkanatsios and Huda developed a simplified method to compute energy imparted from any radiologic procedure (Gkanatsios, 1995; Gkanatsios and Huda, 1997), which may be used with the dosimetry equipment available in most radiology departments. The method is based on Monte Carlo calculations of energy imparted from monoenergetic photons (Boone, 1992) and makes use of published diagnostic energy x-ray spectra (Tucker *et al.*, 1991). The patient is modeled as a homogenous slab of water with a specified thickness. The water equivalence of a given patient may be obtained by direct measurement of the patient or by estimating the thickness of water which results in the same x-ray technique factors when the imaging equipment is in automatic exposure control (AEC) mode. Experimental measurements needed for this computation include the entrance skin exposure, the x-ray beam qualities (kVp and HVL), as well as the exposed area and thickness of the patient, all of which may be readily measured or otherwise estimated. Gkanatsios and Huda compared this method with values of energy imparted determined using Monte Carlo techniques and anthropomorphic phantoms for a range of diagnostic examinations. At 60, 80 and 120 kVp, absolute values of energy imparted obtained using this method differed by 3%, 10% and 22% respectively, from the corresponding results of Monte Carlo computations obtained for an anthropomorphic phantom.

The assumption that energy imparted to the head and trunk can determine radiologic risk has been investigated by many researchers (Bengtsson *et al.*, 1978; Huda, 1984; Carlsson and Carlsson, 1986; Le Heron, 1992; Chapple *et al.*, 1994). It was found that there may be a valid relationship between energy imparted and radiologic risk. Although the radiosensitivities of different organs and tissues are ignored, the energy

imparted will predict associated radiologic risks as accurately as when computing doses to individual organs (Wall *et al.*, 1979; Harrison, 1983; Cameron, 1992). A reasonable linear correlation within a factor of two or three (IPSM, 1988; Huda and Bissessur, 1990) was also detected between total energy imparted and effective dose to the head and trunk. Provided that the examining view (AP, PA, LAT, etc.) and the x-ray beam qualities are known, the effective dose can be determined easily from values of energy imparted (Huda and Gkanatsios, 1997, 1998).

Effective Dose

The effective dose, E , is a dosimetric parameter, which takes into account the doses received by all irradiated radiosensitive organs. The effective dose is able to account for nonuniform irradiation of different organs and tissues in the body. Thus, the effective dose is considered a measure of the stochastic risk associated with radiologic examinations by directly comparing partial body irradiation to whole body radiation exposure (ICRP, 1977, 1991; Huda *et al.*, 1991). Although the effective dose is an occupational dose quantity based on an age profile for radiation workers, this dose descriptor is being increasingly used to quantify the amount of radiation received by patients undergoing radiologic examinations which use ionizing radiation (ICRP, 1987; NCRP, 1989; UNSCEAR, 1993).

Measurement or computation of effective doses for any x-ray examination is difficult and time consuming. An additional problem is that most measurements or calculations make use of a standard phantom based on the reference man as defined by the International Commission on Radiological Protection (ICRP, 1975). Although the

importance of patient size for medical radiation dosimetry has been recognized (Lindskoug, 1992; Chappel *et al.*, 1995), it is not obvious how to scale the effective dose computed for standard man to different sized patients, such as pediatric patients, who undergo similar examinations. These limitations impede the wider use of effective dose in radiology. Huda and Gkanatsios (1997) proposed a method to determine the effective dose, E , to patients undergoing any radiologic examination using the energy imparted to the patient, ϵ . Values of E/ϵ were obtained from the radiation dosimetry data presented for 68 x-ray projections computed using Monte Carlo calculations on an adult anthropomorphic phantom (Hart *et al.*, 1994a). The energy imparted to patients may be determined from values of the exposure-area product incident on the patient and can be combined with E/ϵ ratios (i.e., 5.0 mSv/J for a head PA view) to yield values of the patient effective dose. In addition, this method was extended to determine effective doses to patients who differ in mass from the adult sized phantoms used in current patient dose assessment procedures (Huda *et al.*, 1989b; Le Heron, 1992).

Although the computation of effective dose is cumbersome in most cases, a range of effective doses has been reported in the literature that pertain to neurointerventional procedures. Feygelman *et al.* (1992) studied ten cases and reported values ranging from 1.6-14 mSv with a mean of 6.2 mSv. Bergeron *et al.* (1994) reported an average of 1.8 mSv with a range of 0.44-3.4 mSv for a limited number of eight patients undergoing similar procedures. McParland (1998) reported a median of 7.0 mSv with a range of 2.1-20 mSv when he computed effective doses to patients undergoing cerebral angiography. A wider range was reported by Berthelson and Cederblad (1991), who computed effective doses between 3.5 mSv and 25 mSv.

Despite its popularity, the effective dose introduces some problems when used in diagnostic radiology. First, it does not account for differences between the age distribution of workers and that of the general public with regard to the determination of the appropriate organ weighting factors. The effective dose also excludes curable cancer or hereditary harm beyond the second generation. Both these factors make the effective dose a questionable quantity in risk assessment associated with diagnostic radiologic procedures (UNSCEAR, 1988; Cameron, 1992). It should also be mentioned that the effective dose applies only to low radiation doses, which generally is the case in diagnostic radiology. However, in areas like cardiology and neuroradiology, where extended diagnostic and therapeutic procedures may deliver local patient doses of several Gray, the effective dose may not be an appropriate dosimetric quantity.

Another problem with the effective dose is the uncertainties involved with its calculation. The calculation of the effective dose must include an analysis of the dose distribution within the body, which is difficult to do for radiologic procedures, particularly fluoroscopy. As an alternative, dose distributions are derived from Monte Carlo techniques using mathematical phantoms (Gibbs *et al.*, 1984; Jones and Wall, 1985; Huda *et al.*, 1991; Le Heron, 1992) or from calculations of the average organ dose in anthropomorphic phantoms (Faulkner and Harrison, 1988; Huda *et al.*, 1989a, 1989b). Such techniques, though, can only provide approximations of the true organ dose distribution. Furthermore, the selection of the "remainder" organs is problematic in dose distribution analysis and may vary for each examination. Effective dose also requires the use of a dose equivalent, which is based on the quality factor, Q , of the type of radiation

involved (ICRP, 1977), and use of organ and tissue weighting factors, w_T , (ICRP, 1991). Both these factors are considered to be biologically uncertain (Cameron, 1992).

Notwithstanding the fact that there are problems associated with converting effective doses to a corresponding detriment (Huda and Bews, 1990), there are important benefits to be gained by using effective dose to quantify patient doses in diagnostic radiology. One advantage is that the effective dose attempts to measure the risk to the patient, which is the motivation for all patient dosimetry studies in diagnostic radiology. In addition, the effective dose to a patient undergoing any examination may be compared to that of any other radiologic procedure, as well as to natural background exposure and regulatory dose limits, which are increasingly expressed using effective dose values (ICRP, 1991; NRC, 1995a, 1995b).

Image Quality

The extraction of adequate diagnostic information from radiographic images is important in radiology in order to detect and identify an abnormality and then to interpret its meaning and determine its cause. Thus the quality of the radiographic image is very important in conveying diagnostic information to the observer. Image quality can be described in terms of *contrast*, *noise* and *resolution*.

Image Contrast

Image contrast can be defined as the difference in the optical density (film) or brightness (digital) in an image between an area of interest and its surrounding background. Image contrast is determined by several factors including the characteristics

of the materials being imaged, the characteristics of the x-ray spectrum, the characteristics of the detector and display media and physical perturbations such as scattered radiation (Hasagawa, 1991). These dependencies separate image contrast into *radiographic* (subject) contrast, *detector* contrast and *display* contrast.

Radiographic contrast. Radiographic or subject contrast characterizes the differences in x-ray fluence emerging from different regions of the imaged object. Radiographic contrast depends on differences in material thickness, atomic numbers, physical density and electron density between different regions of the imaged object and their interaction with radiation.

Detector contrast. Detector contrast on the other hand, can be expressed as the ability of the imaging detector to convert differences in x-ray fluence emerging from an object to differences in optical density (film detector) or brightness (digital detector). The detector contrast can shape the radiographic contrast according to the detector's characteristic response to x-rays. Thus, detector contrast depends on the properties of the detector material, its thickness, atomic numbers, electron density and the physical process by which the detector converts x-ray fluence into an image.

Display contrast. The third component of image contrast is the display contrast, which refers to the digital display of images. Display contrast depends on the display parameters (i.e., window and level) under which the image is viewed and can be manipulated by the observer.

Other contrast dependencies. Image contrast in general, is also affected by physical perturbations such as scattered radiation, image intensifier veiling glare and the base and fog of film, all of which reduce image contrast.

Image Noise

Every radiographic image is degraded by noise superimposed on the image by random processes occurring along the imaging chain. Detection of a signal that is superimposed on noise depends on the relative magnitude of the noise compared to the signal and the ability of the observer to differentiate between the brightness distribution of the noise and that of the signal plus noise (Giger *et al.*, 1986b). The overall noise of an image consists of various noise components. The statistical nature of x-ray production and attenuation in the detector results in quantum mottle. Structure mottle, electronic noise, quantization noise, time jitter and display device noise are additional noise components in digital imaging detectors (Giger, 1985).

In digital imaging as in digital subtraction angiography, the noise components can be categorized as *static* and *non-static* noise. Static noise is independent from one frame to the next and always presents the same pattern. Thus, static noise is eliminated in digital subtraction angiography. Structure mottle is the most important static noise component in digital imaging. *Non-static* noise is frame dependent, which means that the noise pattern varies from one frame to the next. Non-static noise sources are always present in digital subtraction angiography. Significant non-static noise sources in digital imaging are the quantum mottle and electronic noise.

The primary source of noise in digital imaging is usually quantum mottle, which corresponds to random spatial fluctuations of the distribution of x-ray quanta absorbed by the detector. Since the production and attenuation of x rays are Poisson statistical processes, quantum mottle follows Poisson statistics, which makes it easily quantifiable. Consequently, increasing the exposure to the imaging detector will improve a

radiographic image by decreasing quantum mottle. Improving the attenuation properties of the imaging detector will also reduce quantum mottle of radiographic images.

Secondary sources of noise become important in radiographic imaging, when the image receptor is exposed to high enough radiation to eliminate most of the quantum mottle. Secondary noise sources in digital imaging consist of the *structure mottle*, *electronic noise*, *quantization noise* and *time jitter*.

Structure mottle. Structure mottle is the second most important noise component in single-frame digital imaging after quantum mottle, and it becomes the dominant noise source in images acquired using high x-ray fluence (Giger *et al.*, 1986b). The structure mottle is introduced to the imaging line by the image intensifier. Structure mottle depends on the physical structure of both the input and output phosphor layers. Since structure mottle is a static component of image noise, its noise pattern is constant from frame to frame. Therefore, structure mottle can be eliminated by the subtraction of two image frames as done in digital subtraction angiography. Another characteristic of structure mottle pertaining to its static nature is that structure mottle remains unchanged after frame integration.

Electronic noise. Electronic noise arises from the video camera as a form of dark current added to the exposure-dependent video signal. The magnitude of electronic noise is inversely proportional to the dynamic range of the TV camera and is relatively independent of video signal size. In order to minimize the perturbations added to a digital radiographic image by electronic noise, the video signal should be maximized when possible (Cohen *et al.*, 1982). In general, the electronic noise in a digital imaging system is quite small relative to the quantum and structure mottle (Roehrig *et al.*, 1981;

Balter *et al.*, 1984). However, electronic noise becomes a significant noise source when an object is imaged at low video levels and using low x-ray fluence. It was also demonstrated by Geiger *et al.* (1986b) that electronic noise contribution becomes substantial at spatial frequencies of about 1.0 cycles/mm.

Quantization noise. Another noise component of a digital imaging system is quantization noise. Quantization noise is the error introduced into an analog signal (i.e., TV video signal) when it is digitized. Quantization noise depends on the width of the quantization step. In general, digital imaging systems are designed to minimize quantization errors, which makes quantization noise insignificant in comparison to quantum mottle or even electronic noise (Burgess, 1984; Boon *et al.*, 1990; Rajapakshe and Shalev, 1994; Baxter *et al.*, 1997).

Time jitter. Another component of noise that may appear in digital imaging systems is time jitter (Arnold and Scheibe, 1984; Esthappan *et al.*, 1998). Time jitter is usually caused by incorrect alignment of the scanning electron beam in the television camera from one video frame to the next. Time jitter may also be caused by a variable asynchrony between the video signal and the analog-to-digital converter. In general, time jitter produces a variation in pixel position from one image frame to the next. The importance of time jitter becomes significant in digital subtraction angiography, when this spatial pixel shift changes the spatial pattern of static noise bringing up structure mottle in a digitally subtracted image. Therefore, careful design and stable electronics are required in digital imaging systems to avoid time jitter in order to eliminate structure mottle completely from digitally subtracted images.

Spatial Resolution

The third parameter used to quantify image quality in addition to contrast and noise is spatial resolution, frequently referred to as resolution. Although spatial resolution does not have as much of an impact on image quality as contrast or noise, in applications of neurointerventional imaging spatial resolution becomes somewhat more important. During interventional neuroradiologic procedures, the need to visualize tiny neurovascular instruments (i.e., catheters and guide wires) and vessels as small as 100 μm , requires high spatial resolution. The spatial resolution of an imaging system can be characterized by its modulation transfer function (MTF) (Haus, 1979; Metz and Doi, 1979) which can be obtained from measurements of the point or line spread functions. The determination of MTF of digital imaging systems, however, requires careful handling to avoid aliasing effects caused by the discrete data sampling of digital systems (Giger and Doi, 1984; Fujita *et al.*, 1985). In general, the spatial resolution of an imaging system depends on *geometric, motion, detector and digitization unsharpness*.

Geometric unsharpness. Geometric unsharpness refers to the loss of image detail due to the finite size of the radiation source (i.e., focal spot) (Hasagawa, 1991). Heat loading of the anode of an x-ray tube requires that the focal spot is large enough to dissipate the generated heat. The finite size of the focal spot creates unsharpness called penumbra at the edges of the imaged object. To limit the amount of geometric unsharpness in neurointerventional imaging, x-ray tubes with steep anode angles (i.e., 9-11 degrees) and small *effective* focal spots (i.e., 0.3 mm or 0.6 mm) are used. Another practice often used in neurointerventional imaging is the use of magnification, which also increases geometric unsharpness.

Motion unsharpness. Motion unsharpness refers to the loss of spatial resolution due to motion of the x-ray source, detector and/or object being imaged (Hasagawa, 1991). When one or more of these components move, motion unsharpness is introduced, which degrades spatial resolution. Patient motion caused by discomfort and the continuous moving of the patient's heart and diaphragm is usually the greatest concern, since source and detector can be easily secured in place. Sedation or immobilization of the patient during a radiographic procedure and short exposure times will help reduce the amount of motion unsharpness.

Detector unsharpness. Detector unsharpness refers to the loss of spatial resolution due to the finite resolving power of the detector (Hasagawa, 1991). In screen-film systems, detector unsharpness is also caused by light diffusion in the intensifier screens. Thicker intensifier screens will allow more light diffusion and create more unsharpness. In digital imaging, spatial resolution depends on the TV bandwidth and pixel size. Thus, TV systems with 1024 lines are used in neurointerventional applications. In addition, any digitization will result in loss of spatial resolution due to the inherent pixellation of a digital image in comparison to the original analog image.

Imaging Technique Factors

Patient doses and image quality are both influenced by the selection of imaging techniques. Figure 2-2 shows some key parameters along the line of an x-ray imaging system which can alter patient absorbed doses and image quality. Such parameters are the *tube voltage, tube filtration, input exposure to the imaging detector, magnification and image processing*. With the exception of image processing, an attempt to decrease

patient dose by altering one or more of these parameters will also degrade image quality. Thus, tradeoffs between varying different imaging technique factors merit investigation to find better ways to improve image quality while maintaining low patient doses.

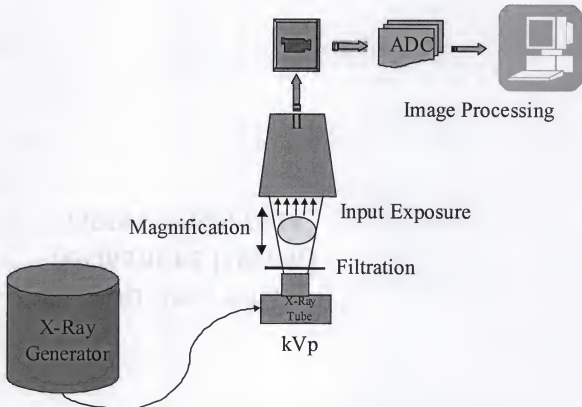


FIGURE 2-1: Key parameters that affect patient dose and image quality in x-ray imaging.

Tube Potential

Very early in the history of diagnostic radiology, tube voltage and the use of specialized K-edge filters were studied extensively to optimize patient dose and image quality (Trout *et al.*, 1952; Koedooder and Venema, 1985; Shrimpton *et al.*, 1988; Nagel, 1989). In general it was shown that an increase in tube voltage decreases patient exposure and degrades image quality. The optimal tube voltage for detecting large-area,

low-contrast iodinated objects was determined to be between 50-60 kVp (Tapiovaara and Sandborg, 1995). The same study also showed that for detecting thin, soft-tissue detail a tube voltage between 70-100 kVp should be used. Also, Thompson *et al.* (1983) concluded that high tube voltages between 100-110 kVp combined with increased contrast agent concentration are the optimal techniques for detecting stones in operative T-tube cholangiography.

The optimal tube potential depends on the imaging requirements of each imaging procedure. In interventional neuroradiologic procedures, where both visibility of small iodinated vessels and high spatial resolution are important, low tube voltage may be used to maintain adequate image quality. As a consequence, low tube voltage will contribute to high patient absorbed doses. As the tube voltage increases, both entrance absorbed dose and energy imparted to the patient decrease for a constant input exposure to the imaging detector. However, it should be noted that for a constant input exposure to the patient, increase in tube voltage would increase the energy imparted to the patient (Gkanatsios and Huda, 1997).

Input Exposure to the Image Receptor

The relationship between input exposure to the image receptor and patient absorbed dose is linear. The input exposure to the image intensifier also affects image quality. As the input exposure increases, the dose to the patient increases and the significance of the quantum mottle in a radiographic image decreases. Since most radiographic images are quantum limited, increasing the exposure to the image receptor will always improve contrast-to-noise (CNR) and signal-to-noise (SNR) ratios by

reducing image noise. However, as the input exposure increases to the point that other noise sources (i.e., structure mottle in single-frame digital radiographs) become as significant as quantum mottle, then any increase in input exposure will have a minor effect on image quality.

Any increase in input exposure to the image receptor at a given tube voltage will increase patient absorbed doses, proportionally. For a film-screen imaging system, where the input exposure to the system is controlled by an optimum optical density, there is negligible flexibility in varying the input exposure. In digital imaging systems, however, the range of input exposure can vary considerably and still produce a useful, diagnostic image. Thus, while operating in the range of input exposures where quantum mottle is the dominant noise component, increasing the input exposure for the purpose of improving contrast visibility is justifiable. However, if the input exposure to the image receptor is already high enough so that quantum mottle is not the primary component of radiographic noise, any increase in input exposure only increases patient absorbed doses. Such practice lowers the standard of patient care by not following the ALARA principle.

Magnification

Magnification and its effects on image quality have been studied in both conventional radiography and mammography (Doi and Rossmann, 1974; Wagner *et al.*, 1981a, 1981b; Sandrik and Wagner, 1982). In general, magnification improves visibility of small, low contrast objects. As the magnification increases, the effective noise in the image detector is reduced improving the signal-to-noise ratio, and visibility of small

structures improves (Doi and Imhof, 1977). Scatter radiation is also reduced with increased magnification, which improved contrast detectability (Sandor and Nott, 1980).

In neurointerventional radiologic procedures, magnification is often used as a tool to visualize small vasculature. Care should be taken, however, when magnification is used, since the entrance absorbed dose to the patient increases significantly with magnification. Energy imparted, on the other hand, is independent of magnification as both distance from the x-ray source and area of exposure decrease equally as magnification is employed. The choice between geometric—change of distance between patient and x-ray source—and electronic magnification—changing the input diameter of the image detector—should be considered every time magnification is required, and the possibility of dose savings between the two methods should be investigated in any imaging system.

CHAPTER 3 SURFACE DOSES

Neuroradiologic Imaging

Clinical Practice

Interventional neuroradiologic procedures are performed on patients suspected to have vascular anomalies in the brain (i.e., aneurysm, vasculitis or arteriovenous malformations), patients that have brain tumors, patients who have had a stroke episode or patients requiring certain types of psychological evaluation. A neurointerventional procedure may be a *diagnostic angiographic* or *therapeutic embolization* procedure. In diagnostic angiographic procedures, the vasculature and blood dynamics of certain parts of the brain are studied by imaging the kinetics of radio-opaque media injected in the vasculature of the brain. In therapeutic neurointerventional procedures, corrective action is taken to occlude vascular anomalies by injecting embolic agents such as gelatin sponges or metallic coils. Usually, a therapeutic embolization procedure is preceded by a diagnostic angiographic procedure. In both types of neurointerventional procedures, x-ray imaging is used extensively in the forms of fluoroscopy, conventional film and digital radiography.

The transfemoral artery technique is used to perform neurointerventional procedures, where a catheter is inserted into the common femoral or deep femoral artery from where it is driven to the vascular network of the brain. Limited amount of frontal

plane fluoroscopy is used on the trunk and thoracic regions to guide the catheter up to the vertebral or carotid arteries. Once there, further use of fluoroscopy in both imaging planes, frontal and lateral, is used to position the catheter at the appropriate site to be studied. Although biplane fluoroscopy is used in this stage, most of the fluoroscopy is still done using the frontal plane. Once the catheter is in place, radio-opaque contrast is injected to that location and a series of radiographic images are acquired in plain film or in digital format. In diagnostic angiographic procedures, the acquisition of radiographic images is done in biplane mode almost exclusively. In therapeutic embolization procedures, both biplane and single plane imaging, either frontal or lateral are used during different stages of the embolization progress evaluation. During each radiographic acquisition, the frame rate and number of frames may vary from 1-3 frames per second and 10-50 frames per acquisition, respectively.

Imaging Equipment

The x-ray imaging system used in this study consisted of a biplane Toshiba[†] KXO-80 high voltage diagnostic x-ray generator and the Toshiba DFP-2000A/A3 digital fluorography system configured for neuroradiologic procedures. The configurations of the two imaging planes, frontal and lateral, were identical. The frontal plane was built around the Toshiba KXO-80C high frequency x-ray generator. The lateral plane was based on its sister generator, the KXO-80D. Both generators were interfaced together to function as a biplane unit suited for neurointerventional applications.

[†] Toshiba America Medical Systems, Tustin, CA

Tri-focal metal Toshiba ROTANODE x-ray tubes having nominal focal spot sizes of 0.3 mm, 0.6 mm and 1.0 mm and inherent filtration of about 3.0 mm aluminum were used as the x-ray sources. The collimator assembly provided an almost circular x-ray field using a multi-blade collimating iris matched tightly to the size of the image intensifier input area. The collimator assembly provided total collimation with the help of four metal blades or partial collimation using wedge shaped, transparent filters. A support table with a comfort pad totaling an equivalent filtration of 3.0 mm aluminum at 80 kVp were placed between the x-ray beam and the patient.

Two image receptors were available. The first receptor was a biplane screen-film system rated as 600-speed and 400-speed for the frontal and lateral imaging planes, respectively. The second image receptor was a digital radiography detector. The digital radiography detector consisted of a CsI image intensifier tube with three effective input diameters of 31 cm, 23 cm and 15 cm. A carbon fiber interspaced grid with a ratio of 10:1 was used to remove scatter radiation to the input phosphor of the image intensifier. An automatic iris control adjusted the amount of light reaching the TV camera. The TV camera consisted of a high-resolution CCD head (1024 lines) and 10-bit analog to digital converter. Digital information was passed from the TV camera to the digital image processor. Analog video signals of 1024 lines at 60 Hz interlaced were passed to the live fluoroscopic high-resolution monitors. The digital image processor was a Toshiba DFP-2000A/A3 digital fluorography system capable of split display fluoroscopy, roadmap fluoroscopy, digital angiography and digital subtraction angiography.

Operation

The x-ray imaging system was capable of continuous fluoroscopy or pulsed fluoroscopy at 15 or 30 frames/sec. Pulsed fluoroscopy could operate at low or high kVp ranges when a high or low tube current (mA) was selected. Pulsed fluoroscopy at 30 frames/sec and high mA setting was primarily used as the default fluoroscopic technique during most neurointerventional procedures. Targeted input exposures to the image intensifier in fluoroscopy were measured at 1.9 $\mu\text{R/frame}$, 3.4 $\mu\text{R/frame}$ and 4.7 $\mu\text{R/frame}$ for the 31 cm, 23 cm and 15 cm input diameters, respectively, using a 2.0 mm copper filter.

Limited amount of frontal plane fluoroscopy was used on the trunk and thoracic regions to drive the catheter to the head region. On average, about thirty seconds (34 ± 11 sec) of fluoroscopy were spent along the trunk region. An additional two minutes (133 ± 77 sec), on average, were spent along the upper thoracic, lower neck region to enter the vertebral or carotid arteries. The remaining use of fluoroscopy was allocated to the head region during placement of the catheter in the appropriate arterial branch to be imaged. During this time, the majority of fluoroscopy was performed in the frontal plane. Lateral fluoroscopy was used in those cases where frontal imaging does not contain adequate information to help in catheter manipulation. Biplane fluoroscopy was used to verify target positioning prior to each contrast injection and imaging.

Digital subtraction angiography (DSA) was the primary imaging method during interventional neuroradiologic procedures and was mainly performed at a rate of 3.0 frames/sec. Rates up to 6.0 frames/sec were used to evaluate high flow dynamics. The input exposure to the image intensifier in digital subtraction angiography was user

selected and it could vary from 50 $\mu\text{R}/\text{frame}$ to 1000 $\mu\text{R}/\text{frame}$ with 500-700 $\mu\text{R}/\text{frame}$ being the default value.

In digital subtraction angiography, most diagnostic radiographic procedures used biplane imaging with the occasional use of single plane imaging during the evaluation of aneurysms of neck origin. In therapeutic embolization procedures, on the other hand, single plane radiography may provide enough information to evaluate the progress of the embolization during the intermediate stages of vessel occlusion. Thus, embolization procedures made extensive use of single plane radiography. Biplane radiography was still required to make definitive evaluation of the embolization result at the more critical stages of the procedure.

Imaging Techniques

In fluoroscopy, the automatic brightness control (ABC) adjusts the x-ray tube voltage to yield the appropriate amount of light at the output of the image intensifier. Figure 3-1 shows the relative frequency at which different tube voltages were used during fluoroscopy of a typical interventional neuroradiologic procedure. Relative frequencies were computed by determining the fraction of surface dose delivered to the patient at each kVp interval. In the frontal plane, the tube voltages mostly used during fluoroscopic imaging were distributed between 66 kVp and 95 kVp, most frequently in the 81-85 kVp range. In the lateral plane, tube voltages between 61 kVp and 85 kVp were equally used during fluoroscopy with a more frequent use of the 71-75 kVp range. In general, the tube voltages used in the frontal plane were shifted about 10 kVp higher to those of the lateral

plane. The difference in physical thickness of the head region between frontal and lateral views explains such differences.

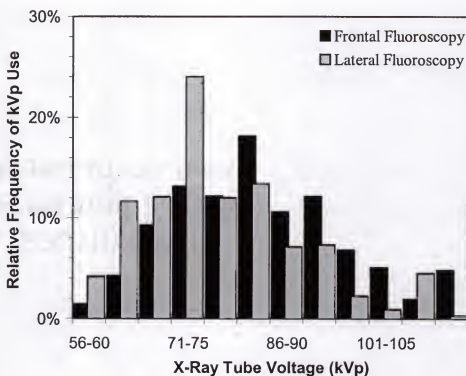


FIGURE 3-1: Histogram of surface dose contribution at different x-ray tube voltages from frontal plane (black bars) and lateral plane (gray bars) fluoroscopy for an average interventional neuroradiologic procedure.

In digital radiography, the tube voltage is determined from the associated fluoroscopic techniques. Figure 3-2 shows the relative frequency at which different tube voltages were used during radiography of a typical interventional neuroradiologic procedure. Similarly to fluoroscopy, the distribution of radiographic tube voltages in the frontal plane was shifted about 10 kVp higher to that of the lateral plane. The most frequently used voltages in the frontal plane were located at the 76-80 kVp range. Tube voltages at the 81-95 kVp range were also used extensively during radiography in the

frontal plane. In the lateral plane, voltages between 61-75 kVp and 86-90 kVp were most frequently used. The range of 66-70 kVp signifies the radiographic tube voltages primarily used in the lateral plane.

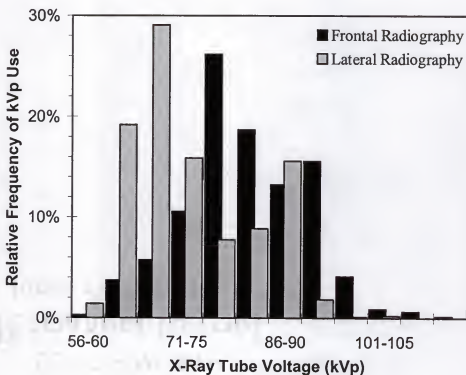


FIGURE 3-2: Histogram of surface dose contribution at different x-ray tube voltages from frontal plane (black bars) and lateral plane (gray bars) radiography for an average interventional neuroradiologic procedure.

The Patient Dosimetry System

System Description

A patient dosimetry system (PEMNET[†]) was installed in April 1995 on each of the two x-ray imaging planes of the Toshiba neurobiplane KXO-80C/D unit. The

[†] PEMNET: Patient Exposure Monitoring Network. Clinical Microsystems Inc., Arlington, VA.

PEMNET unit is a microprocessor-based system running its own on-board software. Eight units can be networked to a single PC server via RS-121 interfaces, through which they transfer patient dosimetric data to the PC server for storage and analysis, or receive calibration information from the PC. The PEMNET system does not measure surface doses directly, as may be the case of dose area product meters (Shrimpton and Wall, 1982). Instead, the system is passively hardwired to the x-ray generator to acquire the input signals listed in Table 3-1. These input signals permit the computation of surface doses that patients would receive, if it were assumed that the same skin area is continually exposed to the x-ray beam.

The PEMNET dosimetry system computed patient surface doses by using the x-ray tube radiation output at the selected technique factors (kVp and mA) together with information about the patient location relative to the x-ray tube and measured exposure times. The patient location was determined from the height of the x-ray table relative to the x-ray tube or by using an ultrasonic sensor at orientations where the position of the table was not relevant, as in lateral views. When the x-ray table intercepted the x-ray beam, x-ray attenuation by the table was taken into account. The surface dose was computed in digital radiography, whereas the surface dose rate was determined in fluoroscopy. In both digital radiography and fluoroscopy, the patient dosimetry system calculated surface dose rates by sampling the radiation technique factors every 5 ms, and by computing an average exposure rate every 800 ms. The surface skin exposure rate and the cumulative surface skin exposure were displayed in real time for each imaging plane

on two panel displays adjacent to the image display monitors and were readily visible by the neuroradiologic staff.

TABLE 3-1: List of the Input Signals Interfaced to the PEMNET Dosimetry System from the Toshiba Neurobiplane Imaging Unit

| Signal Description | Comments |
|--------------------------------------|--------------------------------------|
| Tube Potential (kV) | Radiographic or fluoroscopic |
| Tube Current (mA) | Radiographic or fluoroscopic |
| Pulsed Fluoroscopy Current (mA) | 20 mA or 50 mA |
| Table Height (cm) | Relative to the floor plane |
| C-Arm Height (cm) | Relative to the floor plane |
| C-Arm Angulation (°) | RAO and CAU rotations |
| Ultrasonic Distance Measurement (cm) | Active after a C-arm rotation of 15° |

NOTE: RAO = right anterior oblique; CAU = craniocaudal.

Calibration

The x-ray tube radiation output was determined from exposure measurements obtained using an MDH 1015C[§] radiation monitor with a 10×5-6 ionization chamber attached to the surface of an RSD RS-235^{**} anthropomorphic head phantom as depicted in Figure 3-3. For exposure calibrations, the ionization chamber was located at the isocenter of each C-arm and in direct contact with the head phantom. For frontal (PA) exposures, the ionization chamber was located at the occipital area of the

[§] Radcal Corporation, Monrovia, CA

^{**} Radiology Support Devices Inc; Long Beach, CA

anthropomorphic phantom, while for lateral exposures the chamber was located next to the temporal bone of the phantom. All measurements of entrance skin exposures included the contribution of backscatter radiation. The entrance skin exposure was converted to the surface dose using the expression

$$D = \frac{87.7}{10} \times \frac{\left(\frac{\mu_a}{\rho}\right)_{\text{muscle}}}{\left(\frac{\mu_a}{\rho}\right)_{\text{air}}} \times X \quad \text{mGy} \quad (3.1)$$

where D is dose to muscle in mGy for monoenergetic photons, and X is the exposure in roentgens; $(\mu_a/\rho)_{\text{muscle}}$ is the mass energy absorption coefficient of muscle, and $(\mu_a/\rho)_{\text{air}}$ is the mass energy absorption coefficient of air. The ratio of mass energy absorption coefficients of muscle to air does not change significantly with energy (about 4% between 30 keV and 100 keV x rays) and can be taken to be equal to 1.06 for polyenergetic, diagnostic x-ray spectra (Johns and Cunningham, 1983; Jones and Wall 1985; Wall *et al.*, 1988). The dose D to muscle from polyenergetic x-ray spectra then is given by

$$D = \frac{87.7}{10} \times 1.06 \times X = 9.30 \times X \quad \text{mGy} \quad (3.2)$$

where both the dose in muscle and the exposure in air include contribution from backscatter radiation.

X-ray generator signals fed to the patient dosimetry system were calibrated to read the correct technique factors, source-to-patient distance and tube orientation. The ultrasonic sensors attached to the side of each x-ray tube collimator were calibrated to measure the x-ray source-to-patient surface distance directly. Measured surface doses were entered into the patient dosimetry system and transferred to the PC server along

with kVp, mA, and exposure time information. A calibration program on the PC server generated corresponding surface dose curves (third and fourth degree polynomials) as a function of the applied kVp and mAs at different modes of operation (i.e., radiographic or fluoroscopic) and transferred the curve coefficients back to the system's microprocessor. Two calibrations were performed separately for each imaging plane, with and without the presence of the x-ray table, in order to derive the table attenuation coefficients.



FIGURE 3-3: Calibration setup of the frontal plane (left) and lateral plane (right) using an RSD RS-235 anthropomorphic head phantom.

Evaluation

The accuracy of the patient dosimetry system was evaluated in all fluoroscopic and radiographic modes of operation. In fluoroscopy, the Toshiba neurobiplane unit may be operated either in continuous or pulsed (15 or 30 frames/sec) mode. In the radiographic mode, the unit may be operated either in cut film (CF) mode or in digital subtraction angiography (DSA) mode. Each acquisition mode was investigated using the geometry of a typical patient setup. The ionization chamber was attached to the anthropomorphic phantom as shown in Figure 3-3. For the frontal plane system

evaluation, table attenuation and positioning were taken into consideration. There was no table attenuation during testing of the lateral plane. The source-to-patient distance was measured directly by the ultrasonic sensor in the lateral plane.

Measured surface doses were compared to the corresponding values computed by the patient dosimetry system for the experimental arrangements listed in Table 3-2. Table 3-3 shows ratios of the measured, X_M , to calculated, X_C , surface doses obtained with the patient dosimetry system. Average X_M/X_C ratios (\pm one standard deviation) over clinical kV and mAs ranges are given in Table 3-3, together with the total number of individual data points recorded. Changing the source to patient distance or the electronic magnification during continuous fluoroscopy resulted in an average X_M/X_C ratio of 1.04 ± 0.03 . Simulation of a non-standard examination performed in the frontal plane, with "maximized" changes made to all possible imaging parameters, resulted in a surface dose computed by the patient exposure system of 0.98 Gy whereas the measured value was 0.93 Gy (5% difference).

In general, these results demonstrated that the patient dosimetry system would normally generate surface doses, which are within 5% of the true surface dose. The uncertainties of threshold radiation doses for the induction of deterministic effects such as skin erythema or epilation are considerably larger than 5% (Wagner *et al.*, 1994; Rubin and Casarett, 1968; UNSCEAR, 1988) due to factors such as the anatomical location and size of the irradiated region, tissue vascularity and oxygenation, as well as the patient age, genetic background and hormonal status. Thus the accuracy of the patient dosimetry system is adequate for measuring surface doses to patients undergoing interventional neuroradiologic procedures.

TABLE 3-2: Experimental Arrangements for Evaluating the Patient Dosimetry System

| Arrangement | Variables | Purpose |
|---|-----------------------------------|---|
| Imaging techniques | Tube voltage | Evaluate the system response to technique changes |
| | Tube current | |
| | Exposure time | |
| | Frame rate | |
| | Electronic magnification | |
| Image Acquisition Modes | Geometric magnification | Evaluate the system response in different image acquisition modes |
| | Continuous fluoroscopy | |
| | Pulsed fluoroscopy | |
| | Cut film | |
| | Digital subtraction angiography | |
| Complete neurointerventional procedure (~1.0 Gy) | Image acquisition modes | Simulate a complete patient examination maximizing changes which are technically possible to determine an upper limit of the accuracy of the system |
| | Imaging techniques | |
| | Table height and location | |
| | Source-to-image receptor distance | |
| | C-arm rotation | |
| | Collimation | |

TABLE 3-3: Summary of the Ratios of the Measured to Calculated Surface Doses, X_M/X_C , Obtained During Testing of the Accuracy of the Patient Exposure System

| Operating Mode | Number of Tests | Frontal Plane | Lateral Plane | Comments |
|--------------------------|-----------------|-----------------|-----------------|---|
| Continuous Fluoroscopy | 28 | 0.99 ± 0.03 | 1.04 ± 0.02 | |
| Pulsed Fluoroscopy | 13 | 0.96 ± 0.02 | 0.96 ± 0.02 | kV and mAs techniques were varied |
| Radiography (CF and DSA) | 10 | 0.94 ± 0.05 | 1.01 ± 0.01 | |
| Continuous Fluoroscopy | 5 min | 1.03 | 1.01 | |
| Pulsed Fluoroscopy | 10 min | 0.93 | 1.03 | Automatic brightness control (ABC) was used |
| Radiography (CF and DSA) | 70 frames | 0.93 | 1.00 | |

NOTE: CF = cut film acquisition; DSA = digital subtraction acquisition

SOURCE: Gkanatsios *et al.*, 1997.

Data Acquisition

Following the introduction of the patient dosimetry system into clinical practice, dosimetry data were obtained for 175 patients undergoing interventional neuroradiologic examinations. At the end of each patient examination, the recorded surface dose data were automatically uploaded to the PC server for subsequent analysis. A database with information shown in Figure 3-4 was built. Dosimetry data were analyzed to provide cumulative doses for each imaging mode on both imaging planes for the complete patient neurointerventional procedure. In addition, dosimetry data were also obtained for discrete kV intervals, as well as for discrete dose rate intervals.

Additional information made available by the patient dosimetry system included the total fluoroscopic time, the number of times fluoroscopy was engaged, and the total number of radiographic (cut film and DSA) images acquired.

PEMNET Log ROOM 12: Toshiba Biplane
Tobias L. Hanelius

Patient ID: Attending Radiologist: Peter

Type of Exam: Cerebral Arteriogram Fellow: Stambor

Date of Exam: 12/2/95 Resident:

Age: 25 Biplane: ☒ Male ☒ Female ☐

FRONTAL PLANE

| CONTINUOUS FLUOROSCOPY | PULSED FLUOROSCOPY | DIGITAL SUBTRACTION | TOTALS |
|-------------------------------------|--------------------------------------|---------------------------------------|---------------------------------------|
| Time: <input type="text"/> 1.60 | Time: <input type="text"/> 4.10 | | Time: <input type="text"/> 5.70 |
| Exposure: <input type="text"/> 7.35 | Exposure: <input type="text"/> 11.47 | Exposure: <input type="text"/> 135.62 | Exposure: <input type="text"/> 154.44 |
| Engage: <input type="text"/> 11 | Engage: <input type="text"/> 5 | Frames: <input type="text"/> 294 | |
| R<10: <input type="text"/> 7.35 | R<10: <input type="text"/> 11.47 | R<10: <input type="text"/> 0.02 | R<10: <input type="text"/> 18.84 |
| R<20: <input type="text"/> 0.03 | R<20: <input type="text"/> 0.03 | R<20: <input type="text"/> 0.00 | R<20: <input type="text"/> 0.00 |
| R>20: <input type="text"/> 0.00 | R>20: <input type="text"/> 0.00 | R>20: <input type="text"/> 135.60 | R>20: <input type="text"/> 135.60 |

| | | |
|-----------------------------------|-----------------------------------|------------------------------------|
| <60 kV: <input type="text"/> 0.01 | <60 kV: <input type="text"/> 2.93 | <60 kV: <input type="text"/> 0.02 |
| 60 kV: <input type="text"/> 0.02 | 60 kV: <input type="text"/> 0.12 | 60 kV: <input type="text"/> 0.00 |
| 65 kV: <input type="text"/> 0.01 | 65 kV: <input type="text"/> 0.10 | 65 kV: <input type="text"/> 0.00 |
| 70 kV: <input type="text"/> 0.21 | 70 kV: <input type="text"/> 7.11 | 70 kV: <input type="text"/> 0.00 |
| 75 kV: <input type="text"/> 0.06 | 75 kV: <input type="text"/> 0.65 | 75 kV: <input type="text"/> 0.00 |
| 80 kV: <input type="text"/> 0.01 | 80 kV: <input type="text"/> 0.44 | 80 kV: <input type="text"/> 27.63 |
| 85 kV: <input type="text"/> 1.75 | 85 kV: <input type="text"/> 0.11 | 85 kV: <input type="text"/> 108.00 |
| 90 kV: <input type="text"/> 0.56 | 90 kV: <input type="text"/> 0.00 | 90 kV: <input type="text"/> 0.00 |
| 95 kV: <input type="text"/> 1.05 | 95 kV: <input type="text"/> 0.00 | 95 kV: <input type="text"/> 0.00 |
| 100 kV: <input type="text"/> 1.58 | 100 kV: <input type="text"/> 0.00 | 100 kV: <input type="text"/> 0.00 |
| 105 kV: <input type="text"/> 2.08 | 105 kV: <input type="text"/> 0.00 | 105 kV: <input type="text"/> 0.00 |
| 110 kV: <input type="text"/> 0.00 | 110 kV: <input type="text"/> 0.00 | 110 kV: <input type="text"/> 0.00 |

Record: 34 of 114

FIGURE 3-4: Sample page from the PEMNET database showing all recorded information for the frontal imaging plane.

Fluoroscopy

Dosimetric data including the surface dose received by the patient from use of fluoroscopy, the total time of fluoroscopy, and the rate at which dose was delivered to the patient were recorded by the patient dosimetry system. Additional recorded information included the number of times fluoroscopy was engaged and the x-ray tube voltages used in fluoroscopy during the course of a neuroradiologic procedure (seen in Figure 3-4).

X-Ray Beam Localization

During neurointerventional procedures, fluoroscopy was used to position the catheter next to the vessel anomaly in the brain in order to inject contrast and subsequently image the anomaly. Since the transfemoral artery technique was used to guide the catheter to the vertebral or carotid arteries, some fluoroscopy was performed over the truncal and thoracic regions of a patient. After studying the use of fluoroscopy for ten patients, it was determined that, on average, about thirty seconds (34 ± 11 sec) of frontal plane fluoroscopy were spent on the truncal region and an additional two minutes (133 ± 77 sec) at the upper thoracic, lower neck region.

The amount of fluoroscopy performed over the truncal and thoracic regions was relatively independent of the patient and the type of neurointerventional procedure. Therefore, the surface dose corresponding to 2.5 minutes of fluoroscopy was subtracted from the dose contributed by use of frontal plane fluoroscopy. The remaining dose was considered to be absorbed in the head region of the patient. To subtract this fraction from the surface dose to the head, the average dose rate was computed for each patient,

multiplied by 2.5 minutes and subtracted from the total surface dose corresponding to frontal plane fluoroscopy.

During interventional neuroradiologic procedures, a 20°-30° rotation of the x-ray source in the sagittal plane of the patient may be used when acquiring radiographic images. Although the central axis of the x-ray beam changes position on the surface of the head with rotation of the x-ray source, there are parts of the x-ray beam, which overlap before and after rotation. Such overlaps indicate that there are areas that will always be exposed to radiation regardless of the applied x-ray source rotation. Thus, any rotation of the x-ray source could be ignored when computing surface doses from radiographic exposures, since the maximum surface dose to any given area of the head is of interest.

Surface Doses

Figure 3-5 shows the histogram distribution of the patient surface doses received from fluoroscopy alone. The median values of the fluoroscopic surface doses were 0.32 Gy and 0.11 Gy for the frontal and lateral imaging planes, respectively. Maximum surface doses were computed at 2.4 Gy for the frontal plane and 2.7 Gy for lateral plane. The data shown in Figure 3-5 do not differentiate between diagnostic and therapeutic procedures.

The distribution of surface dose in frontal plane fluoroscopy was mainly spread over the range of 0.0-0.8 Gy. In the lateral plane, the majority of patients (70%) received less than 0.2 Gy with some patients (17%) receiving between 0.2-0.4 Gy. The lateral plane was mainly used for catheter position verification and less for catheter

manipulation, which kept the surface doses in the lateral plane low in comparison to the frontal plane. Surface doses at the tail of the dose distribution for each plane (above 0.6-0.8 Gy) corresponded to embolization neuroradiologic procedures. Such procedures require use of additional fluoroscopy for catheter positioning and verification at the site of occlusion. Twenty-seven (15%) out of 175 patients recorded underwent cerebral embolization.

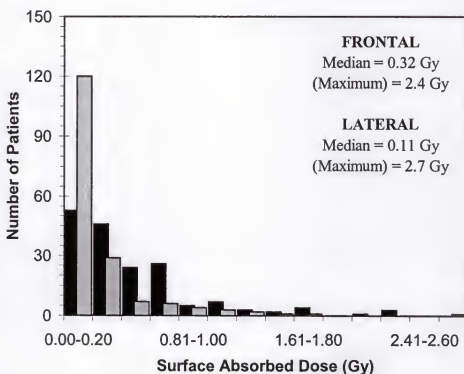


FIGURE 3-5: Histogram distribution of surface doses for 175 patients from frontal plane (black bars) and lateral plane (gray bars) fluoroscopy.

Surface Dose Rates

Figure 3-6 shows the histogram distribution of the rate at which surface doses were delivered to the patient during fluoroscopy. The median values of the fluoroscopic

surface dose rates were 37 mGy/min for the frontal plane and 43 mGy/min for the lateral plane. The maximum skin dose rates recorded by the patient dosimetry system were approximately 100 mGy/min for both planes. Since patient thickness is smaller in the lateral dimension of the head, the automatic brightness control selects a lower tube voltage (also seen in Figure 3-1), which increases the surface dose rate.

The histogram distribution of the surface dose rate in the frontal imaging plane presents a normal distribution shape, but is widely spread over the range of mGy/min to 55 mGy/min. The dose rate distribution in the lateral plane is more concentrated at the 16-30 mGy/min and 46-65 mGy/min. In general, fluoroscopic imaging may vary significantly from patient to patient due to variations in source-to-surface distance and the selection of imaging techniques (i.e., kVp/mA).

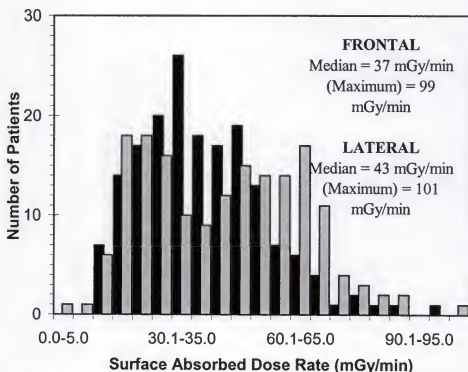


FIGURE 3-6: Histogram distribution of surface dose rates for 175 patients from frontal plane (black bars) and lateral plane (gray bars) fluoroscopy.

Fluoroscopic Times and Intervals

Other useful information recorded by the patient dosimetry system included the total time of fluoroscopy and the number of times fluoroscopy was engaged during an interventional neuroradiologic procedure. Figure 3-7 shows the histogram distribution of total fluoroscopic times in each imaging plane. The frontal plane was most frequently used with a median value of 12 minutes per patient examination compared to a median value of 3.0 minutes in the lateral plane. The fluoroscopic times in the frontal plane were more spread over the range of 5-20 minutes in comparison to the lateral plane, which used less than 5 min of fluoroscopy for the majority (73%) of the patients. The data shown in Figure 3-7 include both diagnostic and embolization neuroradiologic procedures with the higher values corresponding to the latter. For embolization procedures, the duration of fluoroscopy may be extended well beyond the median values to times as high as 70 minutes and 41 minutes for the frontal and lateral planes, respectively.

Figure 3-8 shows a histogram distribution of the number of times fluoroscopy was engaged on each imaging plane. The median number of times that the operator initiated fluoroscopy was 62 in the frontal plane and 26 in the lateral plane. This difference clearly indicates the extensive use of fluoroscopy in the frontal imaging plane during interventional neuroradiologic procedures. Increased number of fluoroscopic instances also indicate higher surface doses (seen in Figure 3-5) and longer fluoroscopic times (Figure 3-7) between the frontal and lateral imaging planes.

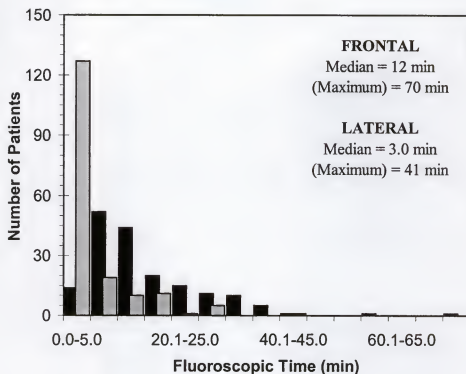


FIGURE 3-7: Histogram distribution of fluoroscopic times to 175 patients from frontal plane (black bars) and later plane (gray bars) fluoroscopy.

Catheter positioning primarily done using the frontal imaging plane varies widely from patient to patient. This difference between frontal and lateral imaging planes introduced a wider spread to the histogram distribution of fluoroscopic intervals corresponding to the frontal plane, as shown in Figure 3-8. Both distributions, however, show long tails with a maximum of 226 fluoroscopic intervals in the frontal plane and 170 intervals in the lateral plane. Such tails on the distribution may account for the need to use additional fluoroscopy during embolization procedures.

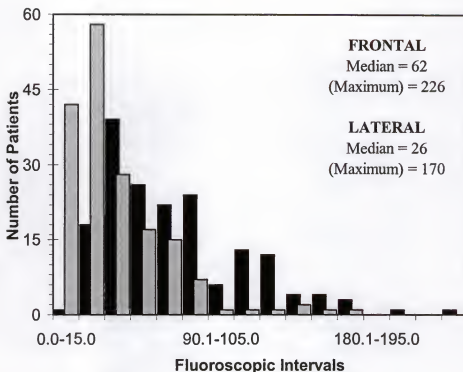


FIGURE 3-8: Histogram distribution of fluoroscopic intervals for 175 patients from frontal plane (black bars) and lateral plane (gray bars) fluoroscopy.

Radiography

Dosimetric data on the surface dose received by the patient from use of radiographic imaging (i.e., cut film and DSA images), the number of radiographic frames, and the dose per frame were recorded by the patient dosimetry system. Additional recorded information included the radiographic tube voltages used during the course of a neuroradiologic procedure (seen in Figure 3-4).

X-Ray Beam Localization

Radiographic image acquisitions are performed almost exclusively on the head region during interventional neuroradiologic procedures. The majority of them is

performed employing the digital subtraction angiography (DSA) technique. As discussed under x-ray beam localization for fluoroscopy, the main goal is to compute the maximum doses delivered to any surface of a patient's head. Similarly to fluoroscopy, radiography may also be considered unaffected by the small degree of x-ray source angulation usually applied to the frontal imaging plane in the sagittal plane of the patient.

Surface Doses

Figure 3-9 shows the histogram distribution of the patient surface doses received from radiographic acquisitions. The median values of the radiographic surface doses were 0.80 Gy and 0.50 Gy for the frontal and lateral planes, respectively. The maximum radiographic dose recorded in the frontal plane was 4.8 Gy, twice the maximum dose recorded in fluoroscopy for the same plane. In the lateral plane the maximum radiographic surface dose was 3.8 Gy, about 30% higher than the maximum dose from fluoroscopy in the same plane.

Although the histogram distribution of the radiographic surface doses in the frontal plane has a longer tail and a higher median value than the dose distribution in the lateral plane, both distributions are very similar. This supports the fact that frontal and lateral plane radiography are equally utilized during any type of interventional neuroradiologic procedure.

Surface Dose Rates

Figure 3-10 shows the histogram distribution of the surface dose per frame in radiographic imaging with median values of 2.5 mGy/frame and 1.8 mGy/frame for the

frontal and lateral planes, respectively. Maximum doses of 5.6 mGy/frame were recorded in the frontal plane and 4.9 mGy/frame in the lateral plane. In general, the size and densities of the head region do not vary significantly among patients. Similar tube voltages would be used for all radiographic imaging acquisitions. Therefore, the distribution of doses per frame depends mostly on changes to the source-to-surface distance (i.e., use of different degrees of magnification among patients). In the frontal plane where geometric magnification is more frequently used, the dose per frame distribution approaches that of a wide normal shaped distribution. In the lateral plane where magnification is not used as often, the distribution is steeper (less variability).

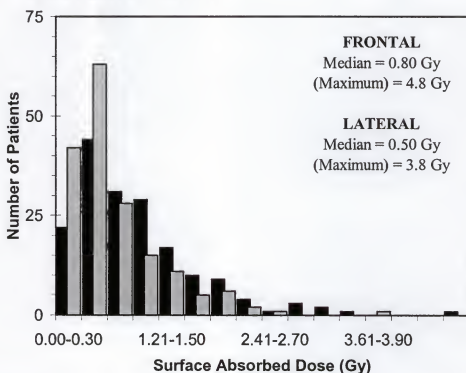


FIGURE 3-9: Histogram distribution of surface doses for 175 patients from frontal plane (black bars) and lateral plane (gray bars) radiography.

Radiographic Frames

Figure 3-11 shows the histogram distribution of the number of radiographic (DSA) frames acquired during diagnostic and therapeutic neuroradiologic procedures. Median values of 353 frames and 316 frames were recorded for the frontal and lateral plane, respectively. Due to the complexity of some embolization procedures, however, the number of frames acquired to evaluate the progress of an occlusion may run as high as 1400 in the frontal plane and 1000 in the lateral plane.

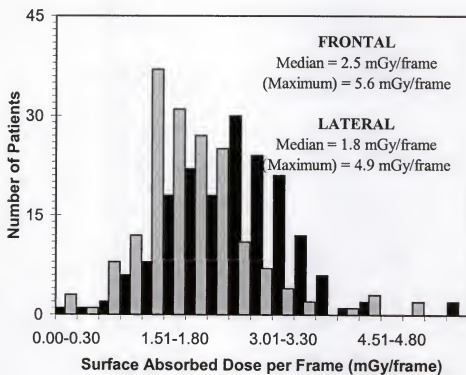


FIGURE 3-10: Histogram distribution of surface dose rates for 175 patients from frontal plane (black bars) and lateral plane (gray bars) radiography.

As shown by the distribution of radiographic frames in both planes, the number of imaging frames required in each procedure is variable. Depending on the degree of difficulty of extracting diagnostic information from the acquired images, as well as the

type of anomaly to be diagnosed, the number of radiographic images acquired is normally between 100 and 500 frames. Embolization procedures, on the other hand, may require two to four times the number of radiographic images to complete the associated tasks.

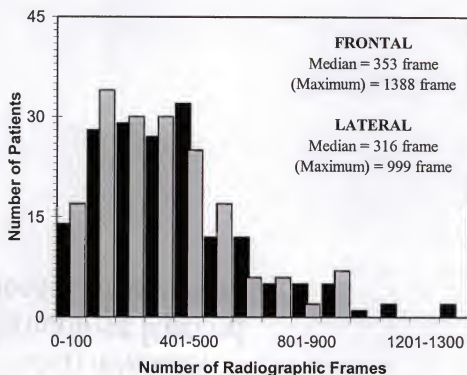


FIGURE 3-11: Histogram distribution of the number of radiographic frames for 175 patients from frontal plane (black bars) and lateral plane (gray bars) radiography.

Conclusions

Figure 3-12 shows the histogram distributions of the total surface dose to the patient from the use of fluoroscopy and radiography during an interventional neuroradiologic procedure. The medians of the total surface dose were 1.2 Gy and 0.64 Gy for the frontal and lateral plane, respectively. The maximum surface dose received by a patient was of the order of 5 Gy for both imaging planes. The majority of the doses

were concentrated between 0.2 Gy and 1.2 Gy for both imaging planes. A significant number of higher doses, however, was indicated by the tails of the two histogram distributions. Most of the dose was contributed by radiography, which accounts for the 67% of the total surface dose in the frontal plane and 78% of the total dose in the lateral plane. Fluoroscopy only accounted for the 33% and 22% of the total surface dose in the frontal and lateral plane, respectively.

Although 28% of the patients in this study may have exceeded the nominal threshold absorbed dose to the skin for the induction of deterministic effects (2 Gy), there were no cases of epilation or skin erythema observed in this series of 175 patients. This is not surprising since any erythema would be fleeting and faint. Epilation would only be identified by a slightly different amount of hair loss, as perceived when combing one's hair, and would not require total loss of hair. For acute radiation exposures, observable effects such as total epilation are more likely to occur at doses in excess of 6 Gy (Huda and Peters, 1994).

Several factors need to be considered in predicting the likelihood of deterministic effects to patients undergoing neuroradiologic examinations. One factor is the fact that radiation doses are delivered over an extended time period, which may be as long as several hours. Of great importance is also the fact that the radiation field is varied over the patient. For individuals with the highest radiation exposures, the neuroradiologist generally makes a concerted effort to either move the relative orientation of the x-ray beam or to utilize the orthogonal imaging plane in so far as these options do not adversely impact the required imaging information. Many of the neuroradiologic imaging procedures also make use of wedge shaped transparent filters which serve to reduce the

radiation doses at the periphery of the x-ray field of view whilst maintaining image quality within the central region. All these factors reduce the likelihood of deterministic injuries to patients and should be practiced during extended neuroradiologic procedures.

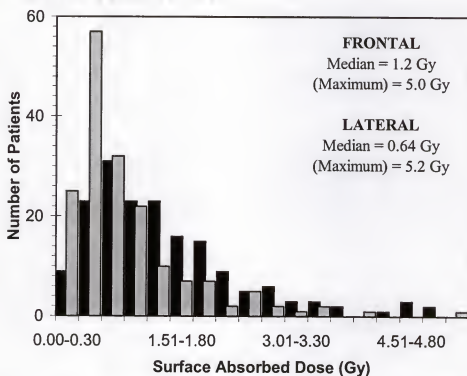


FIGURE 3-12: Histogram distribution of the total surface doses to 175 patients from frontal plane (black bars) and later plane (gray bars) fluoroscopy and radiography combined.

CHAPTER 4

ENERGY IMPARTED AND EFFECTIVE DOSE IN NEURORADIOLOGY

Introduction

The effective dose, E , is a dosimetric parameter which takes into account the doses received by all irradiated radiosensitive organs and may be taken to be measures of the stochastic risk (ICRP, 1977, 1991). Although the effective dose is an occupational dose quantity based on an age profile for radiation workers, this dose descriptor is being increasingly used to quantify the amount of radiation received by patients undergoing diagnostic examinations which use ionizing radiation (ICRP, 1987; NCRP, 1989; UNSCEAR, 1993). Notwithstanding the fact that there are problems associated with converting effective doses to a corresponding detriment (Huda and Bews, 1990), there are important benefits to be gained by using effective dose to quantify patient doses in diagnostic radiology. One advantage is that the effective dose attempts to measure the stochastic risk to the patient, which is the motivation for all patient dosimetry studies in diagnostic radiology. In addition, the effective dose to a patient undergoing any examination may be compared to that of any other radiologic procedure as well as natural background exposure and regulatory dose limits (ICRP, 1991; NRC, 1995a, 1995b).

Measurements or computations of effective doses from x-ray examinations are difficult and time consuming. An additional problem is that most measurements or calculations make use of a standard phantom based on the reference man as defined by the International Commission on Radiological Protection (ICRP, 1975). Although the

importance of patient size for medical radiation dosimetry has been recognized (Lindskoug, 1992; Chappel *et al.*, 1995), it is not obvious how to scale the effective dose computed for standard man to different size patients, such as pediatric patients, who undergo similar examinations. These limitations impede the wider use of effective dose in radiology. Huda and Gkanatsios (1997) developed a more practical approach to compute effective doses from energy imparted for a variety of radiologic examinations and different size patients including infants and children. This method was used in this chapter to compute effective doses from computed values of energy imparted to patients undergoing interventional neuroradiologic procedures.

Exposure-area products to different regions of the body and at different tube voltages were used to compute values of energy imparted, ε , from interventional neuroradiologic procedures (Gkanatsios, 1995; Gkanatsios and Huda, 1997). Values of energy imparted were converted to patient effective dose, E , using E/ε conversion factor corresponding to the projections and body regions irradiated during interventional neuroradiologic procedures. Values of E/ε for the postero-anterior (PA) projections of the abdomen, chest and cervical spine and for the PA and lateral (LAT) views of the head were obtained from radiation dosimetry data computed using Monte Carlo calculations on an adult anthropomorphic phantom (Hart *et al.*, 1994a). This method was extended to determine effective doses to pediatric patients who differ in mass from the adult sized phantom.

Method

Energy Imparted

The energy imparted, ε , to a patient undergoing any radiologic x-ray examination can be estimated by modeling the phantom as a slab of water with thickness z using the expression

$$\varepsilon = \omega \times ESE \times A \quad \text{J} \quad (4.1)$$

where ω is the energy imparted per entrance exposure-area product, ESE is the exposure measured free-in-air at the beam entrance plane of the phantom, and A is the area of exposure also measured at the entrance plane (Gkanatsios, 1995; Gkanatsios and Huda, 1997).

The parameter ω depends on the water phantom thickness z , the x-ray tube voltage and x-ray beam half-value layer (Gkanatsios, 1995; Gkanatsios and Huda, 1997). Values of ω can be computed from

$$\omega = \alpha \times \text{HVL} + \beta \quad \text{J R}^{-1} \text{ cm}^{-2} \quad (4.2)$$

where α and β are coefficients that depend on tube voltage and phantom thickness, and HVL is the half-value layer of the x-ray beam at a given tube voltage in mm of aluminum. Figure 4-1 shows the behavior of ω as a function of water phantom thickness for x-ray tube voltages of 60 kVp, 80 kVp and 100 kVp as apply to the x-ray tube and table filtration of the neuro-biplane Toshiba imaging system. Examples of α and β coefficients and half-value layers of the x-ray beams at different tube voltages are given in Table 4-1.

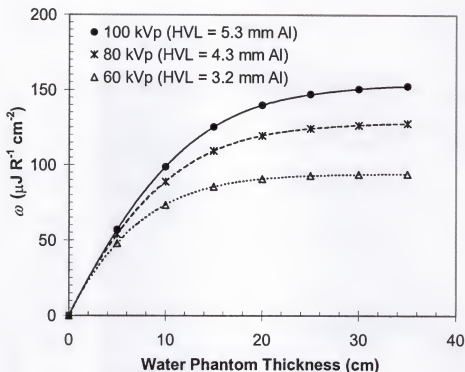


FIGURE 4-1: Values of ω as a function of water phantom thickness for tube voltages of 60 kVp, 80 kVp and 100 kVp.

NOTE: The values of ω were computed for constant voltage waveforms, an x-ray tube anode angle of 11° and 6.0 mm Al filtration (x-ray tube filtration plus table filtration of the Toshiba frontal imaging plane).

The free-in-air entrance exposures to the patient, *ESE*, were obtained from the patient exposure data recorded by the frontal and lateral patient exposure meters at 5 kVp intervals (Figure 3-4). The recorded exposures included the contribution of backscatter radiation from an RSD RS-235^{††} anthropomorphic head phantom. Therefore, backscatter fractions measured using the same phantom were subtracted from the recorded exposures. Table 4-2 lists measured backscatter fractions for the RSD RS-235 anthropomorphic head phantom as a function of tube voltage for the frontal and lateral imaging planes.

^{††} Radiology Support Devices Inc; Long Beach, CA

TABLE 4-1: Computed α and β Coefficients and Half-Value Layers for X-Ray Beams as a Function of Tube Voltage

| Tube Voltage (kVp) | α Coefficient | β Coefficient | HVL—Frontal (mm Al) | HVL—Lateral (mm Al) |
|-----------------------|----------------------|---------------------|------------------------|------------------------|
| 50 | 2.275E-05 | 1.300E-05 | 2.64 | 1.85 |
| 60 | 2.229E-05 | 1.895E-05 | 3.23 | 2.23 |
| 70 | 2.147E-05 | 2.521E-05 | 3.77 | 2.59 |
| 80 | 2.031E-05 | 3.215E-05 | 4.32 | 2.96 |
| 90 | 1.899E-05 | 3.910E-05 | 4.85 | 3.35 |
| 100 | 1.771E-05 | 4.557E-05 | 5.34 | 3.74 |
| 110 | 1.654E-05 | 5.145E-05 | 5.80 | 4.12 |
| 120 | 1.549E-05 | 5.673E-05 | 6.23 | 4.51 |

NOTE: α and β coefficients were computed for a water phantom thickness of 20 cm. The half-value layers were determined for constant voltage waveforms, an x-ray tube anode angle of 11°, 6.0 mm Al filtration for the frontal imaging system (x-ray tube filtration plus table filtration) and 3.0 mm Al filtration for the lateral imaging system (x-ray tube filtration).

Energy imparted values were computed separately for fluoroscopy and radiography. In frontal plane fluoroscopy, the abdominal, upper thoracic, lower neck and head regions were irradiated. As determined in Chapter 3, about thirty seconds of frontal plane fluoroscopy were spent on average on the abdominal region and an additional two minutes at the upper thoracic, lower neck region. The exposures corresponding to these fluoroscopic times were used to compute the energy imparted to the abdomen and upper chest, lower neck body regions. The remaining fluoroscopic exposure was focused over the head region and was used to compute the energy imparted to the head. In lateral

fluoroscopy, frontal radiography and lateral radiography all exposure was taken to be incident on the head region.

TABLE 4-2: Backscatter Fractions of Radiation Exposure at Different Tube Voltages

| Tube Voltage (kVp) | Backscatter Factor (Frontal) | Backscatter Factor (Lateral) |
|-------------------------------|---|---|
| 50 | 0.056 | 0.119 |
| 60 | 0.073 | 0.130 |
| 70 | 0.084 | 0.135 |
| 80 | 0.096 | 0.140 |
| 90 | 0.107 | 0.143 |
| 100 | 0.110 | 0.147 |
| 110 | 0.116 | 0.154 |
| 120 | 0.121 | 0.157 |

NOTE: Backscatter fractions were determined using the RSD RS-235 anthropomorphic head phantom.

For the purpose of computing energy imparted, the water equivalent thickness of the irradiated region as well as the area of exposure at the x-ray beam entrance surface were required. Table 4-3 lists the water equivalent thickness and exposure area of the head regions corresponding to different age groups used to compute energy imparted to the head. Table 4-4 lists the water equivalent thickness and exposure area for different age groups used to compute energy imparted to the abdominal and upper thoracic, lower neck regions.

TABLE 4-3: Patient Thickness and Area of Exposure Corresponding to the Head Region of Different Age Groups

| Patient Age | Head Density (g/cm ³) | PA Thickness (cm) | LAT Thickness (cm) | PA Area of Exposure (cm ²) |
|-------------|-----------------------------------|-------------------|--------------------|--|
| Newborn | 1.057 | 12.3 | 9.51 | 86.7 |
| 1-yr-old | 1.071 | 16.7 | 13.1 | 160 |
| 5-yr-old | 1.090 | 19.8 | 15.5 | 221 |
| 10-yr-old | 1.095 | 20.6 | 16.2 | 239 |
| 15-yr-old | 1.104 | 21.6 | 17.2 | 265 |
| Adult | 1.112 | 22.2 | 17.8 | 279 |

NOTE: PA thickness and LAT thickness represent the equivalent thickness of a water phantom computed from the physical dimensions and density of the head. The area of exposure for each patient group in the PA projection was computed using the physical dimensions of the head. The area of exposure in the LAT projection was estimated to be equivalent to 1.2 of the corresponding areas in the PA projection.

SOURCE: Densities and physical diameters of the head region at different age groups were taken from Huda *et al.*, 1997.

Adult Effective Doses

The National Radiological Protection Board (NRPB) have performed a comprehensive series of Monte Carlo dose calculations for the most common x-ray projections (Hart *et al.*, 1994a). The Monte Carlo runs made use of a hermaphrodite anthropomorphic phantom with a mass of 70.9 kg and a height of 174 cm, which included the female breasts, ovaries, uterus and testes. Each Monte Carlo run tracked the pattern of energy deposition in the anthropomorphic phantom from primary and scattered photons for total 4,000,000 photons used with each x-ray projection. A total of 68 separate views were obtained using x-ray spectra generated between 50 kVp and 120 kVp

with added filtration ranging from 2 mm Al to 5 mm Al. X-ray spectral data were obtained using an updated version of a computer program published by Iles (1987).

TABLE 4-4: Patient Thickness and Area of Exposure Corresponding to the Trunk Region of Different Age Groups

| Patient Age | Trunk Density (g/cm ³) | Abdomen Thickness —PA— (cm) | Chest/Neck Thickness —PA— (cm) | PA Area of Exposure (cm ²) |
|-------------|------------------------------------|-----------------------------|--------------------------------|--|
| Newborn | 0.995 | 9.75 | 9.00 | 175 |
| 1-yr-old | 1.002 | 13.0 | 11.2 | 175 |
| 5-yr-old | 1.000 | 15.0 | 13.2 | 175 |
| 10-yr-old | 1.005 | 16.9 | 13.8 | 175 |
| 15-yr-old | 1.030 | 20.2 | 14.6 | 175 |
| Adult | 1.018 | 20.4 | 15.0 | 175 |

NOTE: The PA thickness represents the equivalent thickness of a water phantom computed from the physical diameters and density of the trunk.

SOURCE: Densities and physical diameters of the trunk region at different age groups were taken from Huda *et al.*, 1997.

For each x-ray examination, the Monte Carlo dosimetry data generated by the NRPB permitted the computation of the effective dose, E , as defined by the International Commission on Radiological Protection (ICRP, 1977, 1991). The phantom breast dose and the mean of the testes and ovary doses were used to determine the contributions to the effective dose from the breast and gonads, respectively. The Monte Carlo dosimetry data also provided the mean doses to three body regions consisting of the head, D_h , trunk,

D_p and legs, D_l . Mean doses to these three body regions were used to compute the mean energy imparted to the patient, ϵ , using the equation

$$\epsilon = D_h \times 5.8 + D_t \times 43.0 + D_l \times 22.1 \quad \text{J} \quad (4.3)$$

where the mass^{††} of the head is 5.8 kg, the mass of the trunk, including the arms, is 43.0 kg and the mass of the legs is 22.1 kg.

The complete dosimetry results of these Monte Carlo simulations have been made available in a software format (Hart *et al.*, 1994b) and were used to obtain the values of effective dose and energy imparted for specific projections as applied to radiation exposures during interventional neuroradiologic procedures. These projections were the postero-anterior projections of the abdomen, chest, cervical spine, and head regions, as well as the right lateral projection of the head region. For each x-ray projection, values of E/ϵ were computed at eight tube voltages ranging between 50 kV and 120 kV and generated at 10 kV intervals with a beam filtration equivalent to 3.0 mm aluminum (lateral plane) and 6.0 mm aluminum (frontal plane). The effective dose per unit energy imparted, E/ϵ (mSv J⁻¹), for the projections of the trunk and head regions are given in Table 4-5. The average E/ϵ ratios of the chest and C-spine projections at each kVp were used to determine effective doses from irradiation of the upper thoracic, lower neck region.

^{††} Wall BF. Private communication (1996).

Pediatric Effective Dose

By definition, 1 Gy of uniform whole body irradiation to x-rays results in an effective dose of 1 Sv and is independent of the mass of the exposed individual. For a 70.9 kg anthropomorphic adult subject to uniform whole body irradiation, energy imparted can be directly converted into effective dose with one joule corresponding to an effective dose of 14.1 mSv. For uniform whole body irradiation, the effective dose $E(M)$ to an individual with a mass M (Table 4-6) who absorbs a total of ε J is given by

$$E(M) = \varepsilon \times 14.1 \times \frac{70.9}{M} \quad \text{mSv} \quad (4.4)$$

Figure 4-2 shows how the effective dose varies with the patient mass for uniform whole body irradiation with a total of one joule imparted to the individual.

For nonuniform exposures normally encountered in diagnostic radiology, the relative radiosensitivity of the irradiated region needs to be taken into account when obtaining the effective dose. The relative radiosensitivity of any body region remains approximately constant with age (ICRP, 1991; Almén and Mattsson, 1996). For instance, if the head accounts for $x\%$ of the total stochastic risk in adults uniformly exposed to x-rays, this body region will also account for approximately $x\%$ of the total stochastic risk for any other age group. As a result, the effective dose to a patient of mass M kg for a given x-ray projection i who absorbs ε joules of energy is obtained using

$$E(M) = \varepsilon \times \left(\frac{E}{\varepsilon} \right)_i \times \frac{70.9}{M} \quad \text{mSv} \quad (4.5)$$

where $(E/\varepsilon)_i$ is the ratio of effective dose to energy imparted (mSv J^{-1}) obtained for the same projection i in the adult anthropomorphic phantom with a mass of 70.9 kg. Standard masses of patients of different ages are given in Table 4-6.

TABLE 4-5: Values of Effective Dose per Unit Energy Imparted, E/ε in mJ/Sv , for Different Body Projections as a Function of Tube Voltage

| kVp | Abdomen (PA) | Chest (PA) | C-Spine (PA) | Head (PA) | Head (LAT) |
|-----|--------------|------------|--------------|-----------|------------|
| 50 | 10.7 | 12.8 | 4.19 | 4.06 | 4.08 |
| 60 | 12.0 | 13.6 | 4.67 | 4.62 | 4.56 |
| 70 | 13.2 | 14.1 | 5.04 | 5.00 | 4.94 |
| 80 | 13.9 | 14.6 | 5.40 | 5.40 | 5.29 |
| 90 | 14.5 | 15.0 | 5.66 | 5.68 | 5.61 |
| 100 | 14.9 | 15.4 | 5.92 | 5.90 | 5.87 |
| 110 | 15.4 | 15.6 | 6.11 | 6.17 | 6.06 |
| 120 | 15.8 | 15.8 | 6.27 | 6.32 | 6.24 |

NOTE: The values of E/ε corresponding to PA views were computed for 6.0 mm Al filtration (frontal imaging plane). The values of E/ε corresponding to the Head LAT view were computed for 3.0 mm Al filtration (lateral imaging plane).

TABLE 4-6: Standard Patient Mass for Different Age Groups

| Age Group | Newborn | 1-yr-old | 5-yr-old | 10-yr-old | 15-yr-old | Adult |
|-------------------|---------|----------|----------|-----------|-----------|-------|
| Patient Mass (kg) | 3.4 | 9.8 | 19 | 32 | 55 | 70.9 |

SOURCE: Huda *et al.*, 1997.

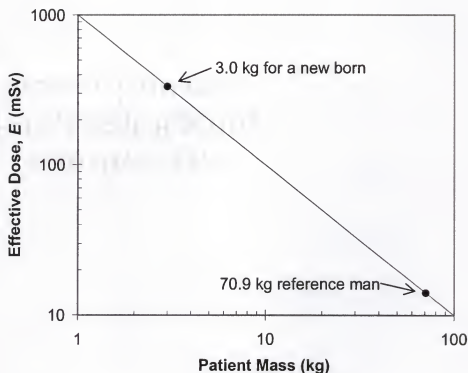


FIGURE 4-2: Effective dose as a function of patient mass for one joule of uniform whole body irradiation.

Adult Patient Doses

The following sections summarize the energy imparted and effective doses to adult patients from interventional neuroradiologic procedures. One hundred and forty nine adult patients, 132 of them underwent diagnostic angiographic and seventeen underwent therapeutic embolization procedures, were studied. Fluoroscopy and radiographic acquisitions were reviewed separately.

Energy Imparted

Figure 4-3 shows the histogram distribution of the energy imparted to patients from use of fluoroscopy during interventional neuroradiologic procedures. The median

value of energy imparted was 1.77 J with energy imparted in the frontal plane being the major component of fluoroscopy. The distribution of energy imparted in fluoroscopy was mainly spread over the range of 0-5 J. Fourteen (9%) of 149 adult patients received more than 5 J with three (2%) patients receiving more than 10 J of energy imparted from fluoroscopy with a maximum value of 12.6 J. Although there was no separation done in the distribution between diagnostic angiographic and therapeutic embolization procedures, the median value of energy imparted to patients who underwent embolizations was 3.48 J. Six of the seventeen embolization patient exceeded the value of 5 J.

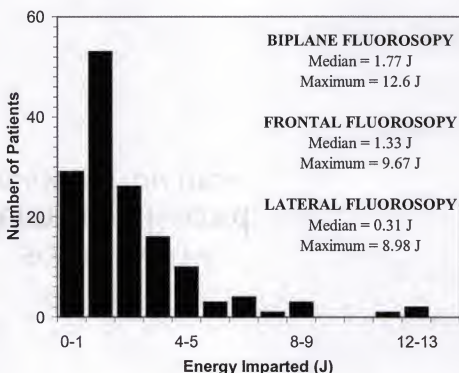


FIGURE 4-3: Histogram distribution of energy imparted to patients from use of fluoroscopy during interventional neuroradiologic procedures.

Figure 4-4 shows the histogram distribution of the energy imparted to patients from radiographic acquisitions during interventional neuroradiologic procedures. The median value of energy imparted was 4.30 J. The distribution of energy imparted from radiographic acquisitions was mainly spread over the range of 0-10 J. Sixteen (11%) of 149 adult patients received between 10 J and 15 J. A maximum value of 21.2 J was recorded. The median value of energy imparted to patients who underwent therapeutic embolization procedures was 8.40 J. Seven of the seventeen embolization patients received energy imparted from radiographic acquisitions greater than 10 J.

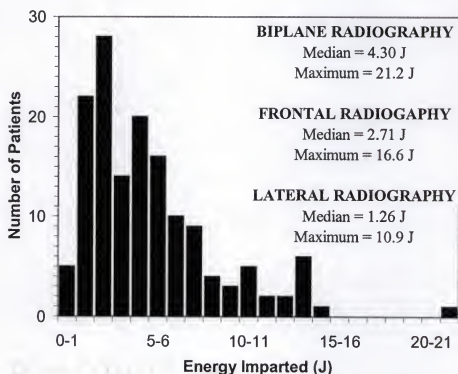


FIGURE 4-4: Histogram distribution of energy imparted to patients from radiographic acquisitions during interventional neuroradiologic procedures.

Figure 4-5 shows the histogram distributions of the total energy imparted to adult patient from diagnostic angiographic and therapeutic embolization neuroradiologic

procedures. The median value of the total energy imparted was 6.69 J. The maximum energy imparted received by a patient was 26.9 J. The majority of the patients who underwent interventional neuroradiologic procedures received up to 14 J of energy imparted. Fifteen (10%) of the adult patients shown by the tail of the distribution in Figure 4-5 received energy imparted between 14 J and 27 J. The median value of the total energy imparted to patients who underwent therapeutic embolization procedures was 13.3 J. Eight of the seventeen embolization patients exceeded the 14 J value of total energy imparted. The largest fraction of energy imparted was produced by radiographic acquisitions. The average fraction of energy imparted from radiographic acquisitions was about 66% of the total energy imparted. Only one third of the total energy imparted was accounted for use of fluoroscopy.

Effective Doses

Figure 4-6 shows the histogram distributions of the total effective dose to adult patient from diagnostic angiographic and therapeutic embolization neuroradiologic procedures. The median value of the total effective doses was 36 mSv. The majority of the patients who underwent interventional neuroradiologic procedures received between 10 mSv and 70 mSv of effective dose. The tail of the histogram distribution shown in Figure 4-6 corresponds to nineteen (13%) patients who received effective doses greater than 70 mSv. The median value of the total effective dose to patients who underwent therapeutic embolization procedures was 74 mSv. Ten of the seventeen embolization patients exceeded the 70 mSv value of total effective dose. As in surface doses and energy imparted, radiographic acquisitions accounted for the largest fraction of the

effective dose to adult patients. On average, about 64% of the effective dose corresponded to radiographic acquisitions. Use of fluoroscopy accounted for only one third of the total effective dose received by patients during interventional neuroradiologic procedures.

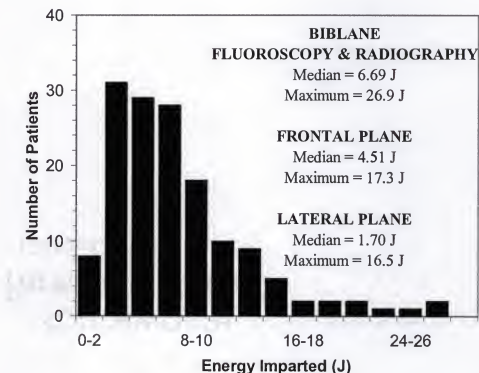


FIGURE 4-5: Histogram distribution of the total energy imparted to patients undergoing diagnostic angiographic and therapeutic embolization neuroradiologic procedures.

Pediatric Patient Doses

The following sections summarize the energy imparted and effective doses to pediatric patients from interventional neuroradiologic procedures. Twenty-six pediatric patients (younger than 20 years of age), sixteen of them underwent diagnostic

angiographic and ten underwent therapeutic embolization procedures, were studied.

Fluoroscopy and radiographic acquisitions were reviewed separately.

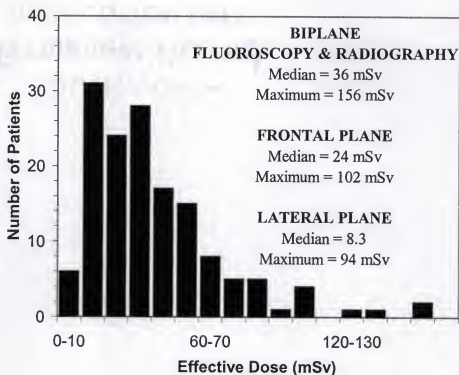


FIGURE 4-6: Histogram distribution of the total effective dose to patients from biplane neuroradiologic examinations.

Energy Imparted

Figure 4-7 plots the energy imparted to pediatric patients from fluoroscopy as a function of patient mass. The mass of each patient was interpolated from Table 4-6 according to the age of the patient. As Figure 4-7 shows, there is no significant correlation of energy imparted to patient mass. The median value of energy imparted from fluoroscopy to all pediatric interventional neuroradiologic procedures was 1.04 J. Pediatric patients who underwent therapeutic embolization procedures had a median of

1.62 J. The median value of energy imparted from fluoroscopy to adult patients who underwent interventional neuroradiologic procedures was 1.77 J.

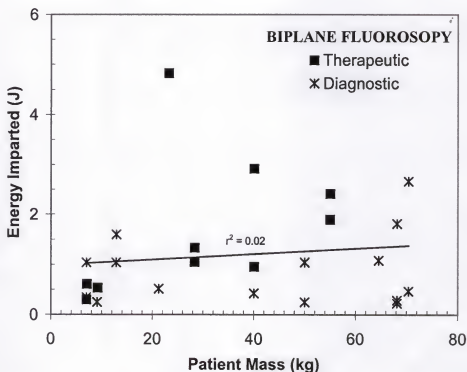


FIGURE 4-7: Energy imparted as a function of patient mass from fluoroscopy during interventional neuroradiologic procedures on pediatric patients. Line shows the linear fit between energy imparted and patient mass.

Figure 4-8 plots the energy imparted to pediatric patients from radiographic acquisitions as a function of patient mass. As was the case for fluoroscopy, there was no significant correlation between the energy imparted from radiographic acquisitions and patient mass. The median value of energy imparted from radiographic acquisitions to all pediatric interventional neuroradiologic procedures was 2.01 J. Pediatric patients who underwent therapeutic embolization procedures had a median value of energy imparted of

2.61 J. The median value of energy imparted from radiographic acquisitions to adult patients who underwent interventional neuroradiologic procedures was 4.30 J.

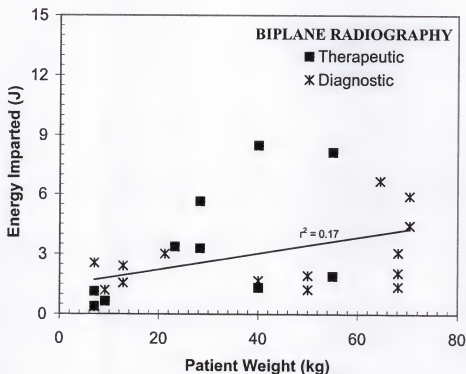


FIGURE 4-8: Energy imparted as a function of patient mass from radiographic acquisitions during interventional neuroradiologic procedures on pediatric patients. Line shows the linear fit between energy imparted and patient mass.

Figure 4-9 plots the total energy imparted to pediatric patients during interventional neuroradiologic procedures as a function of patient mass. As Figure 4-9 shows, there was no significant correlation between total energy imparted from interventional neuroradiologic procedures and patient mass. The median value of total energy imparted to all pediatric interventional neuroradiologic procedures was 3.45 J. Pediatric patients who underwent therapeutic embolization procedures had a median value of energy imparted of 4.09 J. The median value of energy imparted from

radiographic acquisitions to adult patients who underwent interventional neuroradiologic procedures was 6.69 J.

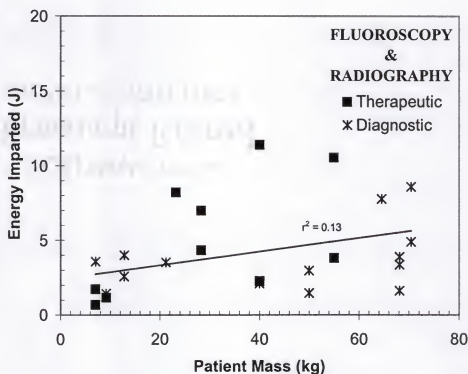


FIGURE 4-9: Energy imparted as a function of patient mass from interventional neuroradiologic procedures on pediatric patients. Line shows the linear fit between energy imparted and patient mass.

Effective Doses

Figure 4-10 plots the total effective dose to pediatric patients from interventional neuroradiologic procedures as a function of patient mass. Although the pediatric data of the total effective doses are widely scattered ($r^2 = 0.3$), a linear correlation between effective dose and patient mass is evident. The median value of total effective dose to all pediatric interventional neuroradiologic procedures was 44 mSv and was higher compared to the median value of 36 mSv effective dose to adult patients. Pediatric

patients who underwent therapeutic embolization procedures had a median value of 66 mSv effective dose.

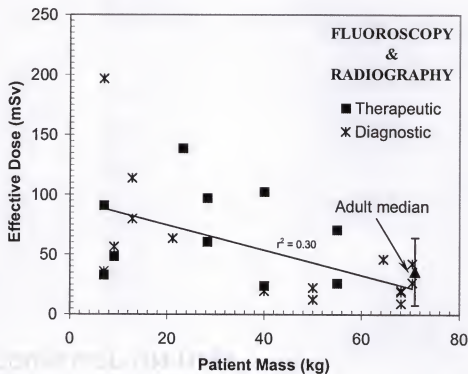


FIGURE 4-10: Effective dose as a function of patient mass from interventional neuroradiologic procedures on pediatric patients. Line shows the linear fit between effective dose and patient mass.

Discussion

Major errors in determining energy imparted to patients result when estimating the equivalent water phantom thickness, z , and due to the implicit differences between a (finite) heterogeneous patient and a semi-infinite homogeneous water phantom. Figure 4-1 shows the energy imparted per unit exposure-area product, ω , as a function of phantom thickness for a range of x-ray tube voltages. The largest increase of ω with phantom thickness is expected at small thicknesses, given that the mean free path of

monoenergetic photons in water ranges from 4.4 cm at 50 keV to 6.6 cm at 140 keV. Once the phantom thickness reaches about three or four mean free paths, most of the x-ray photons will have been absorbed and any further increase of the phantom thickness will have little affect on ω .

Figure 4-1 shows that at 80 kV, the thickness of the water phantom used to simulate a patient for the purposes of estimating energy imparted generally will not be a critical parameter for applications with phantom thicknesses greater than 15 cm. Since the water equivalent size of an adult head is between 18 cm (lateral view) and 22 cm (frontal view), small deviations from the average sizes given in Table 4-3 will have a minimal effect on the computation of energy imparted. A difference between a 20 cm and 22 cm phantom thickness at 80 kVp is of the order of 2%. Even for pediatric patients where the size of the head is smaller (13 cm to 17 cm for 1-yr-olds), a 2 cm error in estimating the water equivalent thickness will result in a maximum error of about 5% when computing energy imparted.

Minor errors in computing energy imparted to patients arise from the use of diverging x-ray beams in clinical applications and the presence of nonuniformities in x-ray beam intensity due to the heel effect. The former is likely to be of negligible importance whereas the latter could easily be accounted for by experimentally obtaining an average entrance skin exposure over the beam area. Measuring the exposure at the centerline of the x-ray beam is also a good approximation of the average exposure over the entire field. Another error in determining energy imparted from irradiation to the head region results from occasional use of wedge shaped transparent filters which serve to reduce the radiation doses at the periphery of the x-ray field of view whilst maintaining

image quality within the central region. Such filters are used during imaging of the frontal view of the head and can attenuate the entrance exposure by about 50% at 80 kVp. As these filters cover an area between 10% and 20%, an overestimate of the energy imparted from frontal imaging plane fluoroscopy of the order of 5% to 10% can occur.

Use of Equation (4.4) permits the determination of the approximate values of effective doses to pediatric patients who undergo radiologic examinations. The NRPB has recently published dosimetric data on pediatric patients ranging from the newborn to 15 year olds (Hart *et al.*, 1996). Figure 4-11 shows a comparison between the E/ε values obtained using Equation (4.4) (continuous line) with the NRPB data (solid circles), which were determined by performing Monte Carlo calculations in a range of anthropomorphic phantoms of different age. Differences between these two data sets, when averaged over the five ages investigated, were 17% with the largest differences shown for the 1-yr-old (31%) and 5-yr-old (36%) phantoms. Such differences may be due to pediatric heads accounting for a markedly larger fraction of the total body masses in these ages compared to adults. It is of interest to note, however, that use of different types of anthropomorphic phantoms to determine pediatric effective doses in planar radiography can result in differences in effective dose of the order of 30% (Hart *et al.*, 1996b).

In general, the effective doses computed in this work compare three to six times higher to values published by others for similar interventional neuroradiologic procedures (Feygelman *et al.*, 1992; Bergeron *et al.*, 1994; McParland, 1998; Berthelson and Cederblad, 1991). However, all other reported values refer to limited number of 8-28 procedures, and none of them made use of means of recording radiation exposures in real time. Different imaging equipment, setup and imaging procedures among institutions

play a major role to how different effective doses may be among institutions. The fact that Shands hospital at the University of Florida is an academic institution that trains new neurointerventional radiologists may also account for some of the differences between the recorded effective doses in this work and others.

Conclusions

Values of energy imparted from interventional neuroradiologic procedures were high due to the demands and complexity of these procedures. The median value of the total energy imparted to adult patients who underwent interventional neuroradiologic procedures was 6.69 J. Pediatric patients received a median value of energy imparted of 3.45 J from interventional neuroradiologic procedures. In the case of therapeutic embolization procedures, additional use of fluoroscopy is required for catheter manipulation and positioning at the site of occlusion, as well as extensive radiographic acquisitions to evaluate the progress of the occlusion. Such demands increased the median values of energy imparted to adults undergoing therapeutic embolization procedures to 13.3 J. Pediatric embolizations received a median value of 4.09 J. Overall, radiographic acquisitions accounted for two thirds of the total energy imparted, with fluoroscopy contributing only one third. There was no significant correlation between energy imparted from interventional neuroradiologic procedures and patient mass.

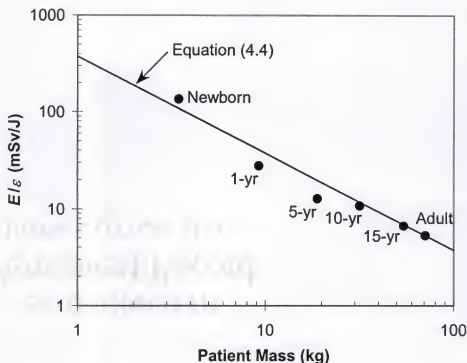


FIGURE 4-11: Comparison of E/ϵ values vs. patient age as determined by Equation (4.4) and by using the dosimetry data from Hart et al. (1996a).

NOTE: Values of E/ϵ were computed for the right lateral projection of the head.

Effective doses computed for the 149 adult patients who underwent interventional neuroradiologic procedures had a median value of 36 mSv. Pediatric patients received a median effective dose of 44 mSv from interventional neuroradiologic procedures. The median effective dose to adults undergoing therapeutic embolization procedures was 74 mSv. Pediatric embolizations received a median effective dose of 66 mSv. As was the case for energy imparted, radiographic acquisitions accounted for two thirds of the total effective dose, with fluoroscopy contributing only one third. Unlike energy imparted, effective doses showed a good linear correlation with patient mass.

The use of the effective dose permits an estimate of stochastic risk to be obtained by using current stochastic risk coefficients (ICRP, 1991; UNSCEAR, 1993; NAS, 1990). At the last attempt of the ICRP (1991) to estimate absolute stochastic risks from whole-body irradiation, a risk coefficient of 5×10^{-5} cancers per mSv of effective dose was derived. Using this risk coefficient, the median effective dose of 36 mSv to adult patients would result in one fatal cancer for every 555 interventional neuroradiologic procedures. An effective dose of 74 mSv to adults undergoing therapeutic embolization procedures would result in one fatal cancer for every 270 such procedures. The immediate, life saving benefits of interventional neuroradiologic procedures, however, far outweigh the risk of distant stochastic effects associated with these procedures. Also, such risk coefficients need to be treated with great caution given the current uncertainties associated with the extrapolation of radiation risks from high doses to those normally encountered in diagnostic radiology (Fry, 1996; Puskin and Nelson, 1996).

In the case of pediatric patients undergoing interventional neuroradiologic procedures, it is important to note that any resultant stochastic detriment will depend on the age of the exposed individual. The stochastic radiation risks of carcinogenesis and genetic effects are generally greater for children than for adults to at least a factor of two (ICRP, 1991; NCRP, 1985). These factors would need to be taken into account when converting any pediatric effective doses into a value of risk or detriment. As a result, direct comparisons of pediatric doses with those of adults need to be treated with circumspection.

CHAPTER 5 IMAGE QUALITY

Image Acquisition

A phantom made of acrylic incorporating 1.0 mm diameter cylindrical vessels filled with iodinated contrast was used to investigate signal detection during digital subtraction angiography (DSA). The detection of signal from iodinated vessels was evaluated by studying the threshold iodine contrast concentration detected in images acquired under specified parameters using digital image subtraction.

Phantom Description

Figure 5-1 illustrates the phantom used to simulate 1.0 mm diameter vessels for the purpose of evaluating image quality in neuroradiology. The phantom consists of stacked acrylic blocks with dimensions of 30 cm \times 30 cm \times 1.3 cm. An insert holder made of acrylic with a thickness of 1.3 cm is positioned at the center of the phantom to accommodate a vessel insert. A *blank* and a *vessel* insert measuring 30 cm \times 9.0 cm \times 1.3 cm were made out of acrylic. The blank insert was used to acquire mask images during digital subtraction angiography. The vessel insert had thirty cylindrical vessels 1.0 mm in diameter and 35 mm in length drilled along its midplane at intervals of 8.0 mm apart. The total phantom thickness was 16.5 cm of acrylic, which was taken to be

equivalent to about 20 cm of water taking the density of acrylic to be 1.19 g/cm^3 (Shleien, 1992).

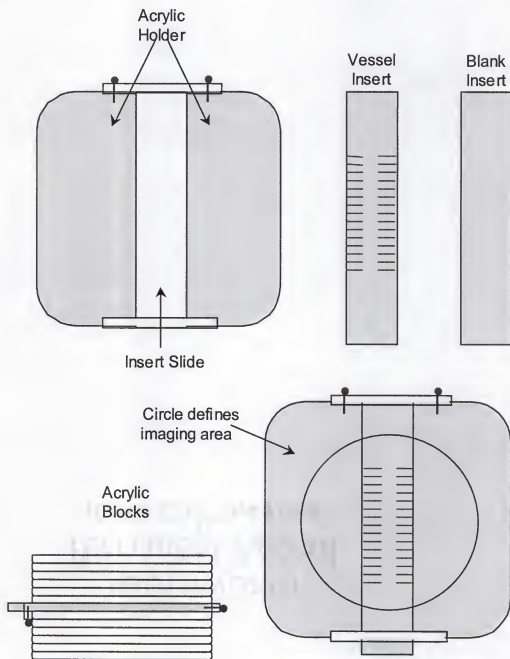


FIGURE 5-1: Schematic diagram of the acrylic phantom with the *vessel* and *blank* inserts used to simulate small vessels for the purpose of evaluating image quality in neuroradiology.

The vessels on the acrylic insert were filled with iodinated contrast prepared from Ultravist^{§§} 300 iopromide solution diluted in heparin solution. The iodine concentrations in the contrast medium used to fill each vessel ranged from 50 mg/cc iodine in contrast solution to about 5.0 mg/cc as given in Table 5-1. The iodine concentration in each vessel was made to be 92% of the previous concentration.

Acquisition of Digitally Subtracted Images

The general experimental setup shown in Figure 5-2 used an x-ray source to image receptor distance (SID) of 105 cm (maximum SID) with the acrylic phantom positioned so that the geometric magnification of the vessel insert was 1.2. A 10×5-6 ionization chamber of an MDH 1015C^{***} exposure meter was attached to the beam entrance surface of the phantom to record entrance exposure. A 10×5-60^{†††} ionization chamber of a second MDH 1015C exposure meter was attached to the surface of the image intensifier behind the grid to record the input exposure to the image receptor. Both ionization chambers were positioned carefully not to overlap with the vessels of the vessel insert as shown in Figure 5-3.

The 23 cm diameter image intensifier mode was used for all image acquisitions. The generator was set to manual techniques allowing fine adjustments of the tube voltage (kVp), tube current (mA) and exposure time (ms). The optical gain was electronically adjusted by changing the diameter of the iris located between the image intensifier output phosphor and TV camera lens to produce a constant video level. All digital subtraction

^{§§} Berlex Laboratories, Wayne, NJ

^{***} Radcal Corporation, Monrovia, CA.

angiography acquisitions were performed using the 0.6 mm focal spot size. The window and level of the displayed images were adjusted to optimize signal detection during each DSA image acquisition, so that the resulting images would not be contrast limited.

TABLE 5-1: Iodine Contrast Concentration in Each Vessel of the Vessel Insert

| | | | | | | | |
|---------------|----|------|---------------------------------------|---------------------------------------|------|----|---------------|
| Vessel Number | 15 | 15.6 | Iodine contrast concentration (mg/cc) | Iodine contrast Concentration (mg/cc) | 14.3 | 16 | Vessel Number |
| | 14 | 16.9 | | | 13.2 | 17 | |
| | 13 | 18.4 | | | 12.1 | 18 | |
| | 12 | 20.0 | | | 11.1 | 19 | |
| | 11 | 21.7 | | | 10.3 | 20 | |
| | 10 | 23.6 | | | 9.43 | 21 | |
| | 9 | 25.7 | | | 8.68 | 22 | |
| | 8 | 27.9 | | | 7.99 | 23 | |
| | 7 | 30.3 | | | 7.35 | 24 | |
| | 6 | 33.0 | | | 6.76 | 25 | |
| | 5 | 35.8 | | | 6.22 | 26 | |
| | 4 | 38.9 | | | 5.72 | 27 | |
| | 3 | 42.3 | | | 5.26 | 28 | |
| | 2 | 46.0 | | | 4.84 | 29 | |
| | 1 | 50.0 | | | 4.45 | 30 | |

NOTE: The iodine concentration in each vessel was made to be 92% of the previous concentration.

††† The 10x5-60 ionization chamber has a gain of $\times 10$ for better resolution.

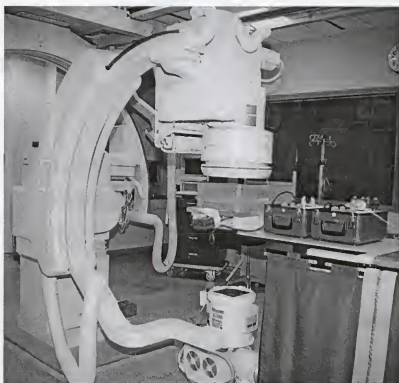


FIGURE 5-2: Experimental setup for DSA acquisitions.



FIGURE 5-3: Position of the two ionization chambers relative to the vessel insert (left).
Subtracted image (right).

The tube voltage was adjusted on the generator and monitored using a Machlett Dynalyser III^{†††} with a digital display. The input exposure to the image intensifier was set by adjusting the product of tube current and exposure time (mAs). The input exposure was verified by the ionization chamber attached to the surface of the image intensifier. The optical gain was controlled by electronic adjustments of the iris diameter to produce a constant video level during all DSA image acquisitions.

The effects of *tube voltage*, *image intensifier input exposure* and *geometric object magnification* were studied by varying the appropriate parameters. The following setup was used for each selected parameter:

Tube voltage (kVp). Baseline techniques were set at a tube voltage of 70 kVp, where the input exposure was adjusted to 120 μ R/frame and the electronic iris was adjusted to produce a mean pixel value between 2000-2100. Then the tube voltage was varied from 50 kVp to 100 kVp and the input exposure was adjusted appropriately to maintain an average pixel value between 2000 and 2100, as shown in Table 5-2. To repeat the experiment at a higher image intensifier input exposure, the baseline techniques were reset at a tube voltage of 70 kVp, where the input exposure was adjusted to 440 μ R/frame and the electronic iris was adjusted to produce a mean pixel value between 2000 and 2100. Then the tube voltage was varied from 50 kVp to 100 kVp and the input exposure was adjusted to maintain the same average pixel value, as shown in Table 5-2.

^{†††} Greenwich Instrument CO., Inc., Greenwich, CT.

TABLE 5-2: Imaging Techniques During Tube Voltage Experiments

| kVp | 120 μ R/frame | | | 440 μ R/frame | | |
|-----|-------------------|------------------------------|----------------|-------------------|------------------------------|----------------|
| | mAs | II Expos (μ R/frame) | Video Level | mAs | II Expos (μ R/frame) | Video Level |
| 50 | 28.0 | 204 | 2075 | 80.0 | 709 | 1914 |
| 56 | 14.4 | 170 | 2018 | 47.5 | 623 | 2052 |
| 60 | 9.28 | 152 | 2104 | 33.0 | 564 | 2031 |
| 66 | 5.40 | 130 | 2028 | 20.5 | 505 | 2085 |
| 70 | 4.00 | 119 | 2068 | 17.0 | 444 | 2018 |
| 80 | 2.24 | 115 | 2054 | 7.50 | 405 | 2056 |
| 90 | 1.50 | 116 | 2117 | 4.60 | 388 | 2080 |
| 100 | 0.960 | 113 | 2079 | 3.20 | 382 | 2075 |

Image intensifier input exposure. The input exposure to the image intensifier was varied from about 50 μ R/frame to 1000 μ R/frame. A tube voltage of 70 kVp was used during all DSA image acquisitions. The optical gain was adjusted accordingly to maintain an average pixel value between 2000 and 2100 for all selected image intensifier input exposures, as such pixel values correspond to clinical practice.

Geometric object magnification. The position of the phantom was varied to achieve a range of geometric object magnification from 1.15⁸⁸ to 2.0. A tube voltage of 70 kVp was used during all DSA image acquisitions. The image intensifier input exposure was first set to 120 μ R/frame and the experiment was

repeated at 440 $\mu\text{R}/\text{frame}$. The mAs was adjusted accordingly to produce a mean pixel value between 2000 and 2100 as shown in Table 5-3.

TABLE 5-3: Imaging Techniques During Geometric Object Magnification Experiments

| Mag | 120 $\mu\text{R}/\text{frame}$ | | | 440 $\mu\text{R}/\text{frame}$ | | |
|------|--------------------------------|--|----------------|--------------------------------|--|----------------|
| | mAs | II Exp ($\mu\text{R}/\text{frame}$) | Video Level | mAs | II Exp ($\mu\text{R}/\text{frame}$) | Video Level |
| 1.15 | 4.40 | 120 | 2100 | 16.3 | 446 | 2100 |
| 1.20 | 4.60 | 119 | 2068 | 17.0 | 444 | 2018 |
| 1.40 | 4.80 | 118 | 2008 | 17.8 | 440 | 2000 |
| 1.60 | 5.00 | 116 | 2036 | 18.3 | 435 | 2010 |
| 1.80 | 5.40 | 122 | 2000 | 18.8 | 435 | 2000 |
| 2.00 | 5.80 | 118 | 2072 | 19.3 | 434 | 2000 |

During all digital subtraction acquisitions, a mask of a single frame was acquired at 3 frames/sec acquisition rate using the blank phantom insert. The blank insert was then replaced by the vessel insert and twenty additional frames were acquired with no frame integration at the same acquisition rate of 3 frames/sec. The tenth frame of each DSA image acquisition was always used for image evaluation. The beam entrance exposures to the phantom and to the image intensifier were recorded during each DSA acquisition sequence.

^{†††} Geometry limited.

Dosimetry and Image Quality

Dosimetry

The exposure to the phantom was measured at the x-ray beam entrance plane using a 10×5-6 ionization chamber of an MDH 1015C. The measured exposure included backscatter radiation coming from the acrylic phantom. The entrance exposure per frame was obtained from the integral exposure measured for each image acquisition sequence divided by the number of acquired frames. A conversion factor of 2.58×10^{-4} C/kg (1R) corresponding to an absorbed dose of 9.3 mGy for muscle tissue was used to convert the beam entrance exposure to surface dose as was shown in Equation 3-2.

The energy imparted was computed using Eqs. 4-1 and 4-2 for the applied tube voltage and corresponding half-value layer. The water equivalent phantom thickness needed to determine energy imparted was taken to be 20 cm for all energy imparted computations. The exposure was obtained from direct exposure measurements during each image acquisition sequence and included backscatter. The backscatter radiation fraction was measured for the corresponding phantom and applied tube voltages and was subtracted from the measured exposures to obtain the free-in-air exposure. The exposure area at the beam entrance plane of the phantom was computed from geometry assuming that the beam area at the image intensifier plane was a circle with a diameter of 23 cm. The diameter and shape of the x-ray beam area were verified using film.

Image Quality Evaluation

For the purpose of evaluating signal detection of small iodinated vessels during digital subtraction angiography, the threshold iodine contrast concentration was determined from the subtracted images of the vessel insert. An independent observer was used for this task. The criteria used to evaluate signal detection by the observer are given in Table 5-4 where a scale of 1-5 was defined to characterize the visibility of a given iodine concentration.

The observer was trained on the criteria of scoring each iodine concentration using ten subtracted images similar to those asked to evaluate. All the images were then presented in a random order to the trained observer. For each image, the observer identified the first vessel that was not visible and scored the consecutive vessels up to the first vessel that was perfectly visible. The lowest concentration that was assigned a score of three was taken to be the threshold iodine concentration of each image.

TABLE 5-4: Score Describing the Visibility of Each Iodine Contrast Concentration

| Score | Comment |
|--------------|--|
| 1 | Iodine concentration was not resolved |
| 2 | Iodine concentration was barely resolved |
| 3 | Iodine concentration was resolved to a confidence level of 50% |
| 4 | Iodine concentration was well resolved |
| 5 | Iodine concentration was perfectly resolved |

Precision of Measurements

A set of technique parameters, which delivered an exposure of approximately 300 $\mu\text{R/frame}$ to the input phosphor and produced a video level of 2000-2100 at 70 kVp, was used to acquire five digital subtraction acquisition sequences. These sequences were acquired at different stages of the experiment. The five image acquisition sequences were used to determine the measurement precision of the computed dosimetric parameters, as well as the precision of the reader performance when evaluating the threshold contrast concentration of the subtracted images.

The exposure to the phantom was measured at the x-ray beam entrance plane and the surface doses and energy imparted were computed for each acquisition. The average entrance exposure measured was $97.6 \pm 0.7 \text{ mR/frame}$. The average video level was 2046 ± 9 . An average surface dose of $0.908 \pm 0.006 \text{ mGy/frame}$ and an average energy imparted of $2.39 \pm 0.02 \text{ mJ/frame}$ were computed from the five image acquisition sequences.

The subtracted images of the five acquisition sequences used to determine the precision were presented to the observer in a random order mixed with other similar subtracted images. The standard deviation of the five readings was taken to be the precision of the threshold contrast concentration and was computed to be $\pm 12\%$ of the threshold contrast concentration ($8.0 \pm 0.96 \text{ mg/cc}$).

Results

Tube Voltage

Table 5-5 (119 $\mu\text{R}/\text{frame}$ at 70 kVp) and Table 5-6 (444 $\mu\text{R}/\text{frame}$ at 70 kVp) summarize the results of surface dose, energy imparted and threshold iodine contrast concentration for varying tube voltage under constant video level during digital subtraction angiography.

Figure 5-4 shows the surface dose and energy imparted as a function of tube voltage. To both low and high input exposures, the surface dose decreased by about 80% and the energy imparted dropped by almost 70% as the tube voltage increased from 50 kVp to 100 kVp. The largest decrease in doses occurred between 50 kVp and 66 kVp.

Figure 5-5 shows the threshold iodine concentration as a function of tube voltage. The threshold concentration increased faster with tube voltage at 120 $\mu\text{R}/\text{frame}$ compared to the 440 $\mu\text{R}/\text{frame}$. At 120 $\mu\text{R}/\text{frame}$, the threshold iodine concentration was proportional to the $kVp^{2.07}$, and increased about 100% when the tube voltage increased from 50 kVp to 70 kVp and another 60% from 80 kVp to 100 kVp. At 440 $\mu\text{R}/\text{frame}$, the threshold concentration became less sensitive to tube voltage changes and was proportional to $kVp^{1.56}$. At this input exposure, changes to the tube voltage from 50 kVp to 70 kVp increased threshold iodine concentration by about 70%. Changes to the tube voltage from 80 kVp to 100 kVp increased threshold contrast by another 40%.

TABLE 5-5: Tube Voltage Dependency at 120 $\mu\text{R}/\text{frame}$

| kVp | II Input Exposure ($\mu\text{R}/\text{frame}$) | Video Level (mean pixel value) | Surface Dose (mGy/frame) | Energy Imparted (mJ/frame) | Threshold Iodine Concentration (mg/cc) |
|-----|--|--------------------------------|--|--|--|
| 50 | 204 | 2075 | 1.22 | 1.55 | 8.0 |
| 56 | 170 | 2018 | 0.811 | 1.17 | 11 |
| 60 | 152 | 2104 | 0.615 | 0.950 | 13 |
| 66 | 130 | 2028 | 0.439 | 0.739 | 12 |
| 70 | 119 | 2068 | 0.377 | 0.657 | 18 |
| 80 | 115 | 2054 | 0.279 | 0.543 | 28 |
| 90 | 116 | 2117 | 0.236 | 0.496 | 30 |
| 100 | 113 | 2079 | 0.196 | 0.438 | 30 |

TABLE 5-6: Tube Voltage Dependency at 440 $\mu\text{R}/\text{frame}$

| kVp | II Input Exposure ($\mu\text{R}/\text{frame}$) | Video Level (mean pixel value) | Surface Dose (mGy/frame) | Energy Imparted (mJ/frame) | Threshold Iodine Concentration (mg/cc) |
|-----|--|--------------------------------|--|--|--|
| 50 | 709 | 1914 | 3.94 | 5.03 | 6.2 |
| 56 | 623 | 2052 | 2.95 | 4.26 | 6.8 |
| 60 | 564 | 2031 | 2.36 | 3.65 | 8.7 |
| 66 | 505 | 2085 | 1.79 | 3.02 | 8.8 |
| 70 | 444 | 2018 | 1.34 | 2.33 | 10 |
| 80 | 405 | 2056 | 0.955 | 1.86 | 12 |
| 90 | 388 | 2080 | 0.653 | 1.37 | 17 |
| 100 | 382 | 2075 | 0.656 | 1.47 | 17 |

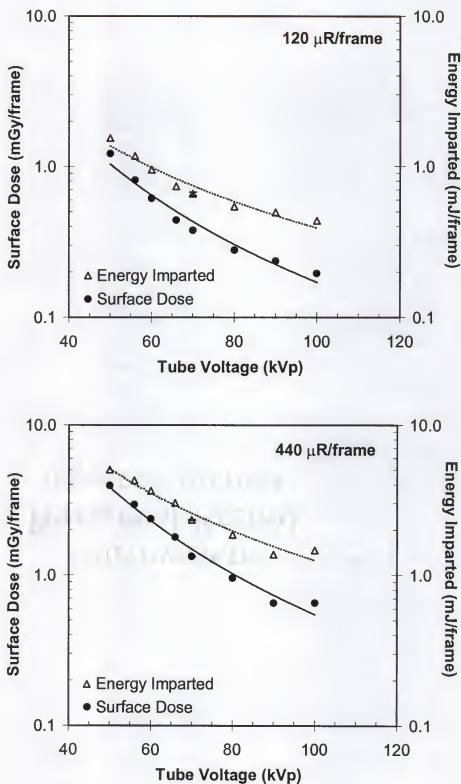


FIGURE 5-4: Surface dose and energy imparted as a function of tube voltage.

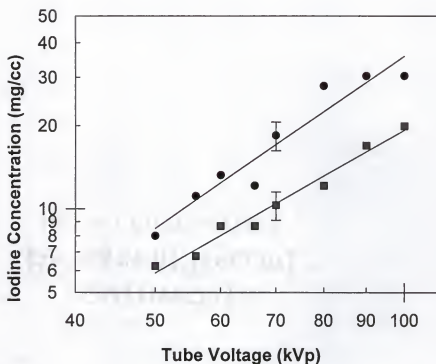


FIGURE 5-5: Threshold iodine concentration as a function of tube voltage. The circles correspond to the 120 $\mu\text{R}/\text{frame}$ and have been fitted to $kVp^{2.07}$. The squares correspond to the 440 $\mu\text{R}/\text{frame}$ and have been fitted to $kVp^{1.56}$.

Image Intensifier Input Exposure

Table 5-7 summarizes the results of surface dose, energy imparted and threshold iodine contrast concentration for varying input exposure to the image intensifier under constant video level and tube voltage during digital subtraction angiography.

Figure 5-6 shows the surface dose and energy imparted as a function of image intensifier input exposure at a tube voltage of 70 kVp. At a given tube voltage, both parameters are directly proportional to the input exposure. For the particular DSA phantom and geometry used, the surface dose per 100 $\mu\text{R}/\text{frame}$ input exposure to the image intensifier was about 0.310 mGy. The energy imparted for the same 100 $\mu\text{R}/\text{frame}$ input exposure was about 0.540 mJ.

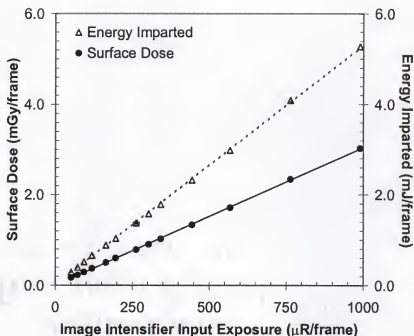


FIGURE 5-6: Surface dose and energy imparted as a function of image intensifier input exposure at 70 kVp.

Figure 5-7 shows the threshold iodine concentration as a function of image intensifier input exposure. In general, as the input exposure increases, the threshold concentration decreases. The data below 250 $\mu\text{R/frame}$ were fitted separately and showed to be proportional to $D^{-0.59}$, where D is the input exposure. Such proportionality indicates a behavior very similar to the theoretical quantum limited curve plotted as $D^{-0.50}$. The data above 250 $\mu\text{R/frame}$ showed proportionality to $D^{-0.27}$. At input exposures below 250 $\mu\text{R/frame}$, increasing input exposure by a factor of two improved threshold concentration by 34%. An improvement of only 17% could be achieved by doubling the input exposure after 300 $\mu\text{R/frame}$.

TABLE 5-7: Image Intensifier Input Exposure Dependency

| Input Exposure ($\mu\text{R}/\text{frame}$) | Mean Video Level (pixel value) | Surface Dose (mGy/frame) | Energy Imparted (mJ/frame) | Threshold Iodine Concentration (mg/cc) |
|--|--------------------------------------|---|--|---|
| 51 | 2016 | 0.172 | 0.299 | 28 |
| 72 | 2060 | 0.232 | 0.404 | 26 |
| 92 | 2092 | 0.296 | 0.516 | 22 |
| 119 | 2068 | 0.377 | 0.657 | 18 |
| 164 | 2032 | 0.506 | 0.882 | 14 |
| 196 | 2040 | 0.598 | 1.04 | 13 |
| 262 | 2036 | 0.908 | 1.38 | 12 |
| 303 | 2052 | 0.903 | 1.57 | 11 |
| 343 | 2012 | 1.026 | 1.79 | 11 |
| 444 | 2018 | 1.336 | 2.33 | 10 |
| 568 | 2084 | 1.72 | 2.99 | 9.4 |
| 764 | 2076 | 2.35 | 4.09 | 8.7 |
| 990 | 2080 | 3.03 | 5.28 | 8.7 |

NOTE: A constant tube voltage of 70 kVp was used for all image intensifier input exposures.

Geometric Object Magnification

Table 5-8 (119 $\mu\text{R}/\text{frame}$) and Table 5-9 (444 $\mu\text{R}/\text{frame}$) summarize the results of surface dose, energy imparted and threshold iodine contrast concentration for varying geometric magnification under constant video level and tube voltage during digital subtraction angiography.

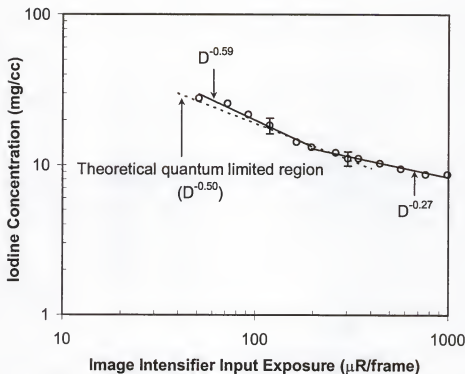


FIGURE 5-7: Threshold iodine concentration as a function of image intensifier input exposure for a constant video level at 70 kVp.

Figure 5-8 shows the surface dose and energy imparted as a function of geometric object magnification at 120 $\mu\text{R}/\text{frame}$ and 440 $\mu\text{R}/\text{frame}$. Surface dose increased as the square of increase in geometric magnification due to its inverse proportionality to the square of the source-to-surface distance. On the other hand, energy imparted remained almost constant with geometric magnification. The 10% increase in energy imparted across the magnification range shown in Figure 5-8 was caused by the increased in imaging techniques to maintain a constant video level (Table 5-3). The increase in radiographic techniques was caused by the reduced scatter reaching the image intensifier by moving the phantom farther away from the image intensifier to increase magnification.

TABLE 5-8: Geometric Object Magnification Dependency at 120 $\mu\text{R}/\text{frame}$

| Geom Object Mag | II Input Exposure ($\mu\text{R}/\text{frame}$) | Video Level (mean pixel value) | Surface Dose (mGy/frame) | Energy Imparted (mJ/frame) | Threshold Iodine Concentration (mg/cc) |
|-----------------|--|--------------------------------|--|--|--|
| 1.15 | 120 | 2100 | 0.320 | 0.638 | 13 |
| 1.20 | 119 | 2068 | 0.364 | 0.656 | 18 |
| 1.40 | 118 | 2008 | 0.531 | 0.674 | 12 |
| 1.60 | 116 | 2036 | 0.745 | 0.688 | 10 |
| 1.80 | 122 | 2000 | 0.960 | 0.711 | 8.7 |
| 2.00 | 118 | 2072 | 1.36 | 0.757 | 10 |

TABLE 5-9: Geometric Object Magnification Dependency at 440 $\mu\text{R}/\text{frame}$

| Geom Object Mag | II Input Exposure ($\mu\text{R}/\text{frame}$) | Video Level (mean pixel value) | Surface Dose (mGy/frame) | Energy Imparted (mJ/frame) | Threshold Iodine Concentration (mg/cc) |
|-----------------|--|--------------------------------|--|--|--|
| 1.15 | 446 | 2100 | 1.18 | 2.27 | 10 |
| 1.20 | 444 | 2018 | 1.35 | 2.35 | 10 |
| 1.40 | 440 | 2000 | 1.96 | 2.39 | 9.4 |
| 1.60 | 435 | 2010 | 2.71 | 2.42 | 8.7 |
| 1.80 | 435 | 2000 | 3.56 | 2.42 | 6.2 |
| 2.00 | 434 | 2000 | 4.65 | 2.46 | 6.2 |

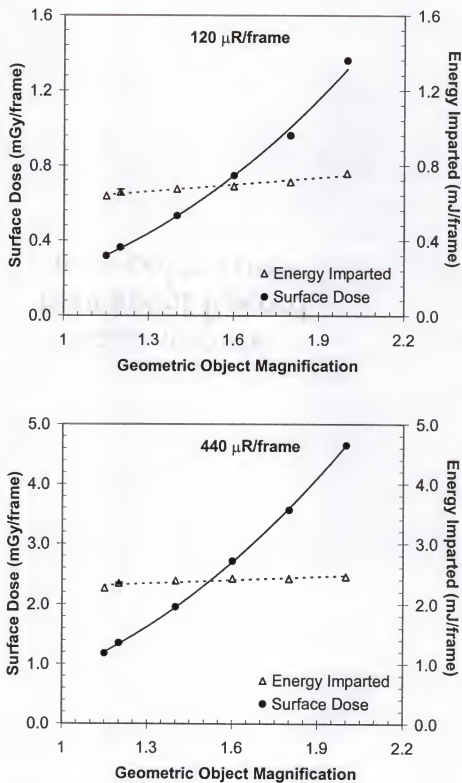


FIGURE 5-8: Surface dose and energy imparted as a function of image intensifier input exposure at 70 kVp.

Figure 5-9 shows the threshold iodine concentration as a function of geometric object magnification at 120 $\mu\text{R}/\text{frame}$ and 440 $\mu\text{R}/\text{frame}$. The difference in threshold concentration between the 120 $\mu\text{R}/\text{frame}$ and 440 $\mu\text{R}/\text{frame}$ input exposures was about 30% across the magnification range shown in Figure 5-9. The relationship between magnification and threshold iodine contrast was approximately linear. An increase by a factor of two to geometric magnification decreased threshold concentration by half.

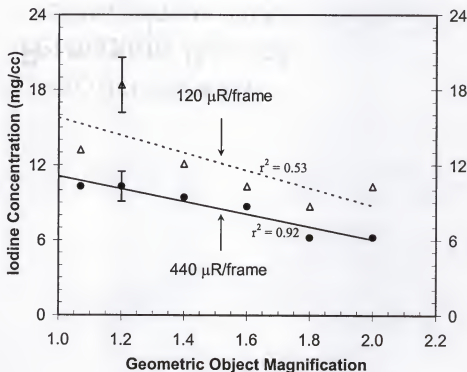


FIGURE 5-9: Threshold iodine concentration as a function of geometric object magnification at 70 kVp.

Discussion

Patient Surface Dose

The effects of tube voltage, input exposure and geometric magnification on surface dose were demonstrated in Figure 5-4, Figure 5-6 and Figure 5-8, respectively. A comparison of the changes introduced to the surface dose by varying these parameters to achieve a given change in threshold iodine concentration is given in Table 5-10 and Table 5-11. The changes in surface dose listed in Table 5-10 have been computed using 70 kVp, 119 $\mu\text{R}/\text{frame}$ and $\times 1.2$ magnification as the starting point. The changes in surface dose given in Table 5-11 have been computed using 70 kVp, 444 $\mu\text{R}/\text{frame}$ and $\times 1.2$ magnification as the starting point.

Figure 5-10 plots the changes in surface dose introduced by the tube voltage, input exposure and geometric magnification versus the corresponding changes in threshold iodine concentration. In general, the smallest increase in surface dose for the same decrease in threshold concentration can be achieved by lowering the tube voltage. At 120 $\mu\text{R}/\text{frame}$ of input exposure where quantum mottle is the primary source of noise (Figure 5-7), magnification becomes the most inefficient parameter to improve signal detection. For achieving the same improvement in threshold concentration, magnification increased surface dose twice as much compared to input exposure and three to four times compared to tube voltage. In the case of 440 $\mu\text{R}/\text{frame}$ input exposure, however, where quantum mottle does not appear to be the primary source of noise, input exposure becomes the most inefficient parameter to improve signal detection.

TABLE 5-10: Comparison of the Effects of Tube Voltage, Input Exposure and Geometric Magnification on the Surface Dose for a Range of Changes in Threshold Iodine Concentration at 120 $\mu\text{R/frame}$

| Change in Threshold Concentration | Change in SD with kVp | Change in SD with II Exposure | Change in SD with Magnification |
|-----------------------------------|-----------------------|-------------------------------|---------------------------------|
| 0.0% | 0.0% | 0.0% | 0.0% |
| (17.3 mg/cc) | (70 kVp) | (119 $\mu\text{R/frame}$) | ($\times 1.2$) |
| -10% | 14% | 19% | 49% |
| (15.6 mg/cc) | (67 kVp) | (142 $\mu\text{R/frame}$) | ($\times 1.4$) |
| -20% | 32% | 45% | 111% |
| (13.9 mg/cc) | (63 kVp) | (173 $\mu\text{R/frame}$) | ($\times 1.6$) |
| -30% | 59% | 81% | 186% |
| (12.1 mg/cc) | (56 kVp) | (216 $\mu\text{R/frame}$) | ($\times 1.8$) |
| -40% | 55% | 135% | 276% |
| (10.4 mg/cc) | (52 kVp) | (280 $\mu\text{R/frame}$) | ($\times 2.0$) |

NOTE: Values in parenthesis indicate the threshold concentration and imaging techniques required to achieve the quoted change in threshold iodine contrast concentration.

TABLE 5-11: Comparison of the Effects of Tube Voltage, Input Exposure and Geometric Magnification on the Surface Dose for a Range of Changes in Threshold Iodine Concentration at 440 $\mu\text{R/frame}$

| Change in Threshold Concentration | Change in SD with kVp | Change in SD with II Exposure | Change in SD with Magnification |
|-----------------------------------|-----------------------|-------------------------------|---------------------------------|
| 0.0% | 0.0% | 0.0% | 0.0% |
| (10.2 mg/cc) | (70 kVp) | (444 $\mu\text{R/frame}$) | ($\times 1.2$) |
| 10% | 21% | 47% | 45% |
| (9.20 mg/cc) | (65 kVp) | (661 $\mu\text{R/frame}$) | ($\times 1.4$) |
| 20% | 49% | 127% | 101% |
| (8.18 mg/cc) | (61 kVp) | (1020 $\mu\text{R/frame}$) | ($\times 1.6$) |
| 30% | 90% | 271% | 168% |
| (7.15 mg/cc) | (56 kVp) | (1670 $\mu\text{R/frame}$) | ($\times 1.8$) |
| 40% | 151% | 554% | 247% |
| (6.13 mg/cc) | (50 kVp) | (2940 $\mu\text{R/frame}$) | ($\times 2.0$) |

NOTE: Values in parenthesis indicate the threshold concentration and imaging techniques required to achieve the quoted change in threshold iodine contrast concentration.

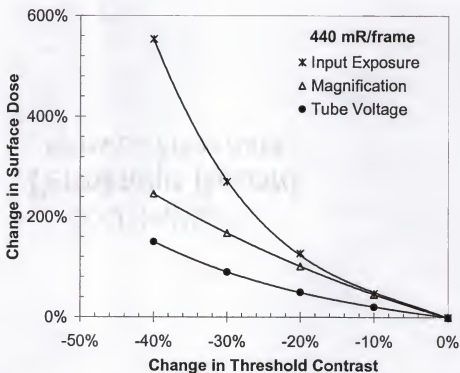
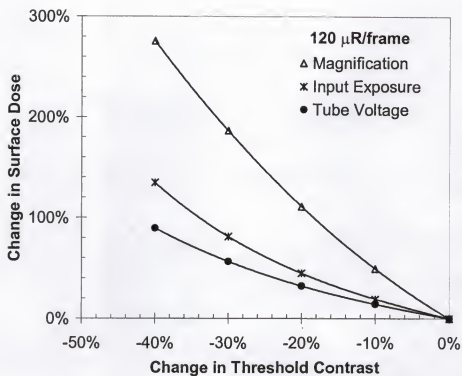


FIGURE 5-10: Change in surface dose versus change in threshold iodine concentration with tube voltage input exposure and magnification.

Energy Imparted

The effects of tube voltage, input exposure and geometric magnification on energy imparted were demonstrated in Figure 5-4, Figure 5-6 and Figure 5-8, respectively. A comparison of the changes introduced to the energy imparted by varying these parameters to achieve a given change in threshold iodine concentration is given in Table 5-12 and Table 5-13. The changes listed in Table 5-12 have been computed using 70 kVp, 119 μ R/frame and $\times 1.2$ magnification as the starting point. The changes in Table 5-13 have been computed using 70 kVp, 444 μ R/frame and $\times 1.2$ magnification as the starting point.

Figure 5-11 shows the changes in energy imparted introduced by the tube voltage, input exposure and geometric magnification versus the corresponding changes in threshold iodine concentration. Unlike the case of surface dose, geometric magnification has a very limited effect on energy imparted and a linear effect on threshold contrast concentration (Figure 5-9). Thus, geometric magnification becomes the parameter of choice to improve signal detection with the least impact on energy imparted. The most inefficient parameter in terms of energy imparted to improve signal detection is the input exposure to the image intensifier. When quantum mottle is the primary noise source on an image, input exposure increases energy imparted two to three times more than tube voltage does for the same threshold contrast changes. As quantum mottle becomes less important to image noise, input exposure increases energy imparted dramatically without a significant increase in image quality.

TABLE 5-12: Comparison of the Effects of Tube Voltage, Input Exposure and Geometric Magnification on the Energy Imparted for a Range of Changes in Threshold Iodine Concentration at Low Input Exposures

| Change in Threshold Concentration | Change in EI with kVp | Change in EI with II Exposure | Change in EI with Magnification |
|-----------------------------------|-----------------------|-------------------------------|---------------------------------|
| 0.0% | 0.0% | 0.0% | 0.0% |
| (17.3 mg/cc) | (70 kVp) | (119 μ R/frame) | ($\times 1.2$) |
| -10% | 9.6% | 19% | 3.9% |
| (15.6 mg/cc) | (67 kVp) | (142 μ R/frame) | ($\times 1.4$) |
| -20% | 21% | 45% | 7.7% |
| (13.9 mg/cc) | (63 kVp) | (173 μ R/frame) | ($\times 1.6$) |
| -30% | 36% | 81% | 12% |
| (12.1 mg/cc) | (56 kVp) | (216 μ R/frame) | ($\times 1.8$) |
| -40% | 56% | 135% | 15% |
| (10.4 mg/cc) | (52 kVp) | (280 μ R/frame) | ($\times 2.0$) |

NOTE: Values in parenthesis indicate the threshold concentration and imaging techniques required to achieve the quoted change in threshold iodine contrast concentration.

TABLE 5-13: Comparison of the Effects of Tube Voltage, Input Exposure and Geometric Magnification on the Energy Imparted for a Range of Changes in Threshold Iodine Concentration at High Input Exposures

| Change in Threshold Concentration | Change in EI with kVp | Change in EI with II Exposure | Change in EI with Magnification |
|-----------------------------------|-----------------------|-------------------------------|---------------------------------|
| 0.0% | 0.0% | 0.0% | 0.0% |
| (10.2 mg/cc) | (70 kVp) | (444 μ R/frame) | ($\times 1.2$) |
| 10% | 15% | 47% | 1.6% |
| (9.20 mg/cc) | (65 kVp) | (661 μ R/frame) | ($\times 1.4$) |
| 20% | 33% | 127% | 3.1% |
| (8.18 mg/cc) | (61 kVp) | (1020 μ R/frame) | ($\times 1.6$) |
| 30% | 58% | 271% | 4.7% |
| (7.15 mg/cc) | (56 kVp) | (1670 μ R/frame) | ($\times 1.8$) |
| 40% | 93% | 554% | 6.3% |
| (6.13 mg/cc) | (50 kVp) | (2940 μ R/frame) | ($\times 2.0$) |

NOTE: Values in parenthesis indicate the threshold concentration and imaging techniques required to achieve the quoted change in threshold iodine contrast concentration.

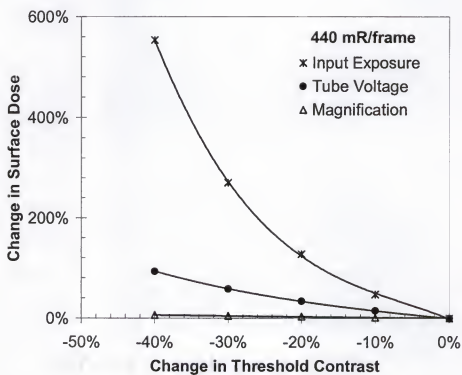
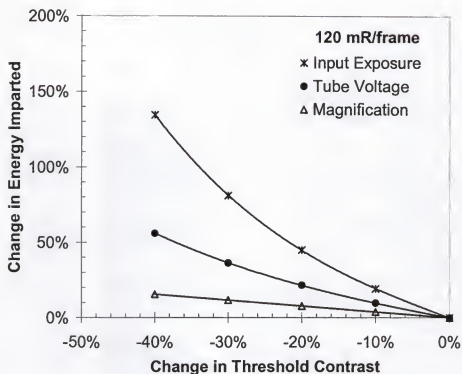


FIGURE 5-11: Change in energy imparted versus change in threshold iodine concentration with tube voltage input exposure and magnification.

Image Quality

Figure 5-5 showed that tube voltage has a significant effect on the threshold iodine concentration. In both 120 $\mu\text{R}/\text{frame}$ and 440 $\mu\text{R}/\text{frame}$ image intensifier input exposures, the tube voltage demonstrated a good power relationship of kVp^n with threshold concentration, where $n \cong 1.8$. The high absorption of iodine at low tube voltages due to its 33 keV K-edge is the primary factor of decreased threshold contrast at low tube voltages. As the tube voltage decreases, the mean energy of the x-ray beam decreases from about 54 keV at 100 kVp (HVL = 5.34 mm Al) to 35 keV at 50 kVp (HVL = 2.65 mm Al). Thus, a 50 kVp x-ray beam with a mean energy just above the K-edge of iodine is expected to produce the highest image contrast. A second factor affecting contrast is scatter radiation. Scatter radiation increases with increased tube voltage and degrades contrast and the signal-to-noise ratio of the images.

In Figure 5-7 where the threshold contrast is given as a function of input exposure to the image intensifier, two regions can be distinguished. The first region extends to an input exposure of about 250 $\mu\text{R}/\text{frame}$ and can be characterized as quantum noise limited ($D^{0.5}$), where quantum mottle is the primary source of image noise. Any increase to input exposure in this region will improve image quality by decreasing quantum mottle. Beyond the input exposure of 250 $\mu\text{R}/\text{frame}$, the relationship between threshold iodine concentration and input exposure deviates from being quantum limited to $D^{0.27}$. At this region of input exposures, other noise factors (i.e., electronic noise, time jitter and structure noise) become equally important to quantum mottle. Such factors are not affected by any increase to input exposure. Additional increases to input exposure beyond 250 $\mu\text{R}/\text{frame}$ is not as effective in improving image quality. Thus, it is sensible

to select an input exposure of about 250 $\mu\text{R}/\text{frame}$ for all image acquisitions in digital subtraction angiography.

Figure 5-9 shows that geometric object magnification has a linear effect on threshold concentration. In both 120 $\mu\text{R}/\text{frame}$ and 440 $\mu\text{R}/\text{frame}$ input exposures, doubling geometric magnification decreased threshold concentration by a factor of two. The major factor that improves contrast with geometric magnification is the increase in the projected area of the imaged object (i.e., iodinated vessel). The increase of signal area improves the signal-to-noise ratio of the imaged object and improves signal detection. Another factor that improves threshold iodine concentration with increased magnification is the increased air-gap. Air-gaps act as scatter removal media. As the air-gap between the phantom and the image receptor increases with magnification, less scatter radiation reaches the image receptor and contrast is improved.

The wide variability of readings at low input exposures may be explained by the significant image noise on those images, which makes image quality evaluation difficult. Possible variation of distance between the image and the observer will also introduce some variability during image evaluation. As the distance of the observer from the image varies, the perceived diameter of the vessel changes affecting signal detection (Burgess and Humphrey, 1997).

Conclusions

Reducing the x-ray tube voltage offered the largest improvement in image quality for a given increase in patient dose. Increasing the image intensifier input exposure beyond 250 $\mu\text{R}/\text{frame}$ provided very little improvement in image quality. This image

intensifier input exposure level should not be exceeded in interventional neuroradiologic imaging, unless a valid justification is explicitly given. A linear relationship was observed between magnification and threshold concentration, which offers significant patient benefits when surface doses are not expected to exceed the threshold doses for the induction of deterministic effects. In cases when stochastic effects may be significant (i.e., pediatric cases), and deterministic effects can be tolerated, a significant increase in image quality can be achieved by increasing geometric magnification without introducing any significant changes to energy imparted.

During digital subtraction angiography, the amount of iodine contrast that can be tolerated by a patient may also be of concern. Due to continuous dilution of the iodine contrast in the blood stream, the iodine concentration in the imaged blood vessel decreases significantly with distance. A higher iodine concentration would be required to image distant vessels especially during the capillary phase. Instead of increasing the iodine concentration in such cases, use of lower tube voltages will decrease the threshold concentration significantly to allow use of less of an amount of iodine. Changing the tube voltage from 70 kVp to 50 kVp, for example, will decrease the threshold concentration by more than 50%, which translates to 50% less iodine used on the patient. Such a decrease in tube voltage, however, results in about 140% increase in surface dose and 90% increase in energy imparted.

CHAPTER 6 CONCLUSIONS

Patient Dosimetry

Surface Doses

Patients undergoing interventional neuroradiologic procedures receive significant radiation doses due to the complexity of such procedures and the amount of diagnostic information required to evaluate neuroradiologic abnormalities. The median values for the recorded surface doses to the 175 patients undergoing interventional neuroradiologic procedures were 1.2 Gy in the frontal imaging plane (occipital region of the head) and 0.64 Gy in the lateral imaging plane (next to temporal bone). The maximum surface dose received by a patient was of the order of 5 Gy in either imaging plane. The majority of the patients received surface doses between 0.3 Gy and 2.3 Gy. Thirty-three percent of the patients exceeded the dose taken to be the threshold surface dose (2 Gy) for deterministic injuries of the skin. Most of the surface dose was contributed by radiographic acquisitions, which accounted for the 67% of the total surface dose in the frontal plane and 78% of the total dose in the lateral plane. Fluoroscopy contributed only 33% and 22% of the total surface dose in the frontal and lateral planes, respectively.

Although about 33% of the patients in this study may have exceeded the nominal threshold surface dose to the skin for the induction of deterministic effects, there were no

cases of epilation or skin erythema observed among the 175 patients who underwent interventional neuroradiologic procedures. When determining the likelihood of deterministic effects to patients undergoing neuroradiologic examinations, it should be noted that the radiation doses are delivered over an extended time period, which may be as long as several hours and the radiation field may vary over the patient. For acute radiation exposures, observable effects such as total epilation are more likely to occur at doses much higher than 2 Gy, which is considered to be the threshold for the induction of deterministic effects.

Effective Doses

Patients who underwent interventional neuroradiologic procedures received typically between 10 mSv and 70 mSv of effective dose. The distribution of effective doses to these patients had a median value of 36 mSv with a maximum effective dose of 156 mSv. Patient who underwent diagnostic procedures had a median value of 38 mSv total effective dose. The median value of the total effective dose to patients who underwent therapeutic embolization procedures was 74 mSv. Ten of the seventeen adult embolization procedures exceeded the 70 mSv value of total effective dose. Two thirds of the effective dose was contributed by imaging in the frontal imaging plane. As was the case for surface dose, radiographic acquisitions accounted for the largest fraction of the effective dose to adult patients. On average, about 64% of the effective dose corresponded to radiographic acquisitions. Use of fluoroscopy accounted for only one third of the total effective dose received by patients during interventional neuroradiologic procedures.

Using the recent risk coefficient of 5×10^{-5} cancers per mSv of effective dose (ICRP 1991), the effective doses computed in this study can be converted to a stochastic detriment. The median effective dose of 36 mSv to adult patients undergoing interventional neuroradiologic procedures would result in one fatal cancer for every 555 such procedures. An effective dose of 74 mSv to adults undergoing therapeutic embolization procedures would result in one fatal cancer for every 270 embolizations. In general, these stochastic risks are low compared to the life saving benefits the patients receive by undergoing interventional neuroradiologic procedures.

In the case of pediatric patients undergoing interventional neuroradiologic procedures, the effective dose was found to have a linear correlation to patient mass (age). This correlation resulted to higher effective doses to pediatric patients compared to the corresponding adult effective doses. The median effective dose to pediatric patients was 44 mSv. Pediatric patients undergoing embolization procedures received a median effective dose of 66 mSv.

Any resultant stochastic detriment depends on the age of the exposed individual. The stochastic radiation risks of carcinogenesis and genetic effects are generally greater for children than for adults to at least a factor of two (ICRP 1991, NCRP 1985). These factors would need to be taken into account when converting any pediatric effective doses into a value of risk or detriment. In general, pediatric patients receive approximately the same effective doses as adult patients do from interventional neuroradiologic procedures. The fact that stochastic risks associated with children are higher than the risks associated with adults requires that we should focus our attention to reducing doses to pediatric patients undergoing interventional neuroradiologic procedures.

Image Quality

The tube voltage had the strongest effect on image quality for the same increase of patient dose among the three technique parameters studied—tube voltage, image intensifier input exposure and geometric object magnification. The photoelectric effect of iodine at low tube voltages improves contrast detectability and thus signal detection as tube voltage decreases. This strong correlation between tube voltage and threshold concentration can be expressed as a power relationship of kVp^n where $n \approx 1.8$. Tube voltage also has a significant effect on patient doses. A decrease of 70%-80% in surface dose and effective dose can be achieved by increasing the tube voltage from 50 kVp to 100 kVp while the other two parameters remain constant, with the largest decrease in doses occurring between 50 kVp and 66 kVp.

Two regions of image intensifier input exposures were observed regarding changes in threshold concentration. The first region was extended below 250 $\mu R/\text{frame}$ and was quantum mottle limited. Increasing input exposure by a factor of two in this region improved threshold concentration by 34%. The second region was observed above 250 $\mu R/\text{frame}$, where less improvement in image quality could be achieved beyond this point, since quantum mottle did not appear to be the primary source of image noise. An improvement of only 17% could be achieved by doubling the input exposure at the region beyond 250 $\mu R/\text{frame}$. Thus, it is sensible to select an input exposure of 250 $\mu R/\text{frame}$ as the input exposure for all image acquisitions in digital subtraction angiography to capitalize in the improvement of image quality without significantly increasing patient doses.

Geometric object magnification was found to be linearly correlated to threshold contrast. Increasing geometric magnification by a factor of two improved image quality by decreasing threshold iodine contrast by a factor of two. This increase in image quality by applying geometric magnification can be achieved with a minimal increase in effective dose to the patient. Thus, magnification can be used to improve signal detection where stochastic risks may be of concern. On the other hand, geometric magnification had a strong effect on surface dose. Geometric magnification should be minimized where there is a concern of deterministic injuries.

In general, the three imaging parameters studied in this work to quantify their effects on image quality and patient dose indicated that reducing the x-ray tube voltage offered the largest improvement in image quality for a given increase in patient dose. Increasing the image intensifier input exposure beyond 250 $\mu\text{R}/\text{frame}$ provided very little improvement in image quality. A linear relationship was observed between magnification and threshold concentration, which offers significant patient benefits when surface doses are not expected to exceed the threshold doses for the induction of deterministic injuries. These facts should be considered every time a selection of imaging techniques is required for optimization purposes.

Future Work

The traditional threshold for the induction of deterministic injuries to the skin was proposed to be of the order of 2 Gy (Wagner *et al.*, 1994). A significant number (28%) of patients undergoing interventional neuroradiologic procedures studied in this work exceeded the proposed threshold for deterministic effects without noticing any radiation

injuries such as epilations and erythemas. This suggests that a higher threshold value should be considered as the triggering point of such deterministic injuries. More work is required to re-evaluate these thresholds and determine a better value.

In this work, there was no image processing other than window and level applied to the digitally subtracted images during the evaluation of image quality. A multitude of processing algorithms and techniques are available that may be able to improve image quality without affecting patient dose. Such image processing techniques may be studied to evaluate their effects on signal detection as they may apply on digital subtraction angiography.

Digital subtraction angiography uses the photoelectric effect in iodine occurring at 33 keV to differentiate between angiographic structures and other anatomy. Different contrast agents with higher atomic numbers and K-edge energies will be able to reduce patient dose for the same image quality. However, the toxicity of higher atomic number agents may limit such effects. Such contrast agents need to be evaluated for applications in interventional neuroradiology to quantify their effects on image quality and the corresponding changes in patient dose.

The already high quantum detective efficiency (DQE) of current image intensifier systems used in x-ray imaging sets a limit to further improvement in signal detection with the current imaging equipment used in interventional neuroradiology. It is likely that a direct digital detector that will be able to exceed the efficiency of current image intensifiers, improve signal detection and decrease patient dose will replace the image intensifier in the future. The application of such digital x-ray image receptors requires further development and evaluation.

BIBLIOGRAPHY

- Almén A, Mattsson S. "On the calculation of effective doses to children and adolescents." *Journal of Radiation. Protection*. **16**: 81-89 (1996).
- Arnold BA, Scheibe PO. "Noise analysis of a digital radiography system." *American Journal of Roentgenology* **142**: 609-613 (1984).
- Balter S, Ergun D, Tscholl E, Buchmann F, Verhoeven L. "Digital subtraction angiography: fundamental noise characteristics." *Radiology* **152**: 195-198 (1984).
- Baxter WT, Davidenko JM, Loew LM, Wuskell JP, Jalife J. "Technical features of a CCD video camera system to record cardiac fluorescence data." *Ann Biomed Eng* **25**: 713-725 (1997).
- Bengtsson G, Blomgren P, Bergman K, Åberg L. "Patient exposures and radiation risks in Swedish diagnostic radiology." *Acta Radiologica Oncology* **17**: 81-105 (1978).
- Bergeron P, Carrier R, Roy D, Blais N, Raymond J. "Radiation doses to patients in neurointerventional procedures." *American Journal of Neuroradiology* **15**: 1809-1812 (1994).
- Berthelsen B, Cederblad Å. "Radiation doses to patients and personnel involved in embolization of intracerebral arteriovenous malformations." *Acta Radiologica* **32**: 492-497 (1991).
- Boone JM. "Parametrized x-ray absorption in diagnostic radiology from Monte Carlo calculations: Implications for x-ray detector design." *Medical Physics* **19**: 1467-1473 (1992).
- Boone JM, Shaber GS, Tecotzky M. "Dual-energy mammography: a detector analysis." *Medical Physics* **17**: 665-675 (1990).
- Burgess AE. "Effect of quantization noise on visual signal detection in noisy images." *J Opt Soc Am [A]* **2**: 1424-1428 (1985).
- Burgess AE, Humphrey K. "Visual perception limits in angiography." *Proceedings of the Society of Photo-Optical Instrumentation Engineers* **127**: 51-59 (1997).
- Burkhart RL. *Patient Radiation Exposures in Diagnostic Radiology Examinations: An Overview*. HHS Publication (FDA), Rockville, MD 82-8219 (1983).

- Cameron, J. "Dose equivalent out—Imparted energy in." *HPS Newsletter* 7-8 (1992).
- Carlsson C. "Determination of integral absorbed dose from exposure measurements." *Acta Radiologica* 1: 433-458 (1963).
- Carlsson C. "Integral absorbed doses in roentgen diagnostic procedures. I. The dosimeter." *Acta Radiologica Therapy Physics Biology* 3: 310-326 (1965a).
- Carlsson, C. "Integral absorbed doses in roentgen diagnostic procedures. II. Measurement of integral doses in two roentgen diagnostic departments." *Acta Radiologica Therapy Physics Biology* 3: 384-408 (1965b).
- Carlsson G, Carlsson C. "Relations between effective dose equivalent and mean absorbed dose (energy imparted) to patients in diagnostic radiology." *Physics in Medicine and Biology* 31: 911-921 (1986).
- Carlsson G, Carlsson C, Persliden, J. "Energy imparted to the patients in diagnostic radiology: calculation of conversion factors for determining the energy imparted from measurements of the air collision kerma integrated over beam area." *Physics in Medicine and Biology* 29: 1329-1341 (1984).
- Chappel CL, Broadhead DA, Faulkner K. "A phantom based method for deriving typical patient doses from measurements of dose-area product on populations of patients." *British Journal of Radiology* 68: 1083-1086 (1995).
- Chapple C, Faulkner K, Hunter E. "Energy imparted to neonates during X-ray examinations in a special care baby unit." *British Journal of Radiology* 67: 366-370 (1994).
- Chopp M, Portnoy HD, Schuring R, Croisaant P. "Clinical dosimetry during cerebral arteriography." *Neuroradiology* 20: 79-81 (1980).
- Cohen G, Wagner L, Rauschkolb E. "Evaluation of a digital subtraction angiography unit." *Radiology* 144: 613-617 (1982).
- Doi K, Imhof K. "Noise reduction by radiographic magnification." *Radiology* 122: 479-487 (1977).
- Doi K, Rossmann K. "The effect of radiographic magnification on blood vessel imaging with various screen-film systems." *Medical Physics* 1: 257-261 (1974).
- Esthappan J, Harauchi H, Hoffmann KR. "Evaluation of imaging geometries calculated from biplane images." *Medical Physics* 25: 965-975 (1998).
- Faulkner K, Harrison R. "Estimation of effective dose equivalent in diagnostic radiology." *Physics in Medicine and Biology* 33: 83-91 (1988).

- Feygelman VM, Huda W, Peters KR. "Effective dose equivalents to patients undergoing cerebral angiography." *American Journal of Neuroradiology* 13: 845-849 (1992).
- Field SB, Upton AC. "Non-stochastic effects: Compatibility with present ICRP recommendations." *Int J Radiat Biol* 48: 81-94 (1985).
- Fry RJM. "Effects of low doses of radiation." *Health Physics* 70: 823-827 (1996).
- Fujita H, Doi K, Giger ML. "Investigation of basic imaging properties in digital radiography. 6. MTFs of II-TV digital imaging systems." *Medical Physics* 12: 713-720 (1985).
- Gibbs S, Pujol A, Chen T, Malcolm A, James E. "Patient risk from interpatient radiography." *Oral Surgery* 58: 347-354 (1984).
- Giger ML. *Investigation of Basic Imaging Properties in Digital Radiography*. Ph.D. Dissertation, University of Chicago, Chicago, IL (1985).
- Giger ML, Doi K. "Investigation of basic imaging properties in digital radiography. 1. Modulation transfer function." *Medical Physics* 11: 287-295 (1984).
- Giger ML, Doi K, Fujita H. "Investigation of basic imaging properties in digital radiography. 7. Noise Wiener spectra of II-TV digital imaging systems." *Medical Physics* 13: 131-138 (1986a).
- Giger ML, Ohara K, Doi K. "Investigation of basic imaging properties in digital radiography. 9. Effect of displayed gray levels on signal detection." *Medical Physics* 13: 312-318 (1986b).
- Gkanatsios NA. *Computation of Energy Imparted in Diagnostic Radiology*. Master Thesis University of Florida, Gainesville, FL (1995).
- Gkanatsios NA, Huda W. "Computation of energy imparted in diagnostic radiology." *Medical Physics* 24: 571-579 (1997).
- Gkanatsios NA, Huda W, Peters KR, Freeman JA. "Evaluation of an on-line patient exposure meter in neuroradiology." *Radiology* 203: 837-842 (1997).
- Grosswendt B. "Backscatter factors for x-rays generated at voltages between 10 and 100 kV." *Physics in Medicine and Biology* 29:579-591 (1984).
- Grosswendt B. "Dependence of the photon backscatter phantom for water on source-to-phantom distance and irradiation field size." *Physics in Medicine and Biology* 35:1233-1245 (1990).
- Harrison R. "A re-evaluation of the 'saturated scatter' method for estimating the energy imparted to patients during diagnostic radiology examinations." *Physics in Medicine and Biology* 28: 701-707 (1983).

- Hart D, Jones DG, Wall BF. *NRPB Report 262: Estimation of Effective Dose in Diagnostic Radiology from Entrance Surface Dose and Dose-Area Product Measurements*. National Radiological Protection Board, Chilton, Oxon, UK (1994a).
- Hart D, Jones DG, Wall BF. *NRPB Software SR262: Normalized Organ Doses for Medical X-Ray Examinations Calculated Using Monte Carlo Techniques*. National Radiological Protection Board, Didcot, Oxon (1994b).
- Hart D, Jones DG, Wall BF. *NRPB Software SR279: Normalized Organ Doses for Pediatric X-Ray Examinations Calculated Using Monte Carlo Techniques*. National Radiological Protection Board, Didcot, Oxon (1996a).
- Hart D, Jones DG, Wall BF. *NRPB Report R279: Coefficients for Estimating Effective Doses from Pediatric X-Ray Examinations*. National Radiological Protection Board, Didcot, Oxon (1996b).
- Hasagawa BH. *The Physics of Medical X-Ray Imaging*. Medical Physics Publishing, Madison, WI (1991).
- Haus AG (editor). *AAPM Monograph #2. The Physics of Medical Imaging: Recording System Measurements and Techniques*. American Institute of Physics, New York, NY (1979).
- Huda W. "Is energy imparted a good measure of the radiation risk associated with CT examinations?" *Physics in Medicine and Biology* 29: 1137-1142 (1984).
- Huda W, Bews J. "Population irradiation factors (PIFs) in diagnostic medical dosimetry." *Health Physics* 59: 345-347 (1990).
- Huda W, Bissessur K. "Effective dose equivalents, H_E , in diagnostic radiology." *Medical Physics* 17: 998-1003 (1990).
- Huda W, Gkanatsios NA. "Effective doses and energy imparted in diagnostic radiology." *Medical Physics* 24: 1311-1316 (1997).
- Huda W, Gkanatsios NA. "Effective doses associated with extremity radiographic examinations." *Health Physics* 75: 492-499 (1998).
- Huda W, Lentle B, Sutherland J. "The effective dose equivalent in radiology." *Journal of the Canadian Association of Radiologists* 40: 3-4 (1989a).
- Huda W, McLellan J, McLellan Y. "How will the new definition of 'effective dose' modify estimates of dose in diagnostic radiology?" *Journal of Radiation Protection* 11: 241-247 (1991).
- Huda W, Peters KR. "Radiation-induced temporary epilation after a neuroradiologically guided embolization procedure." *Radiology* 193:642-644 (1994).

- Huda W, Sandison G, Palser R, Savoie D. "Radiation doses and detriment from chest x-ray examinations." *Physics in Medicine and Biology* 34: 1477-1492 (1989b).
- Hummel R, Wesenberg R, Amundson G. "A computerized x-ray dose-monitoring system." *Radiology* 156: 231-234 (1985).
- Iles WJ. *NRPB Report R204: The Computation of Bremsstrahlung X-Ray Spectra Over an Energy Range 15 keV to 300 keV*. National Radiological Protection Board, Didcot, Oxon (1987).
- Institute of Physical Sciences in Medicine. *Report 55: Are X-Rays Safe Enough? Patient Doses and Risks in Diagnostic Radiology*. The Institute of Physical Sciences in Medicine, York, England (1988).
- International Commission on Radiological Protection (ICRP). *Publication 23: Report of the Task Group on Reference Man*. Pergamon Press, Oxford (1975).
- International Commission on Radiological Protection (ICRP). *Publication 26: Annals of the ICRP 1(3). Recommendations of the International Commission on Radiological Protection*. Pergamon Press, Oxford, England (1977).
- International Commission on Radiological Protection (ICRP). *Annals of the ICRP 2(1). Statement for the 1978 Stockholm Meeting of the International Commission on Radiological Protection*. Pergamon Press, Oxford, England (1978).
- International Commission on Radiological Protection (ICRP). *Publication 34: Protection of the Patient in Diagnostic Radiology*. Pergamon Press, Oxford (1982).
- International Commission on Radiological Protection (ICRP). *Publication 36: Annals of the ICRP 10(2/3). Cost-Benefit Analysis in the Optimization of Radiation Protection*. Pergamon Press, Oxford (1983).
- International Commission on Radiological Protection (ICRP). *Publication 47: Annals of the ICRP 14(3). Non-Stochastic Effects of Ionizing Radiation*. Pergamon Press, Oxford (1984).
- International Commission on Radiological Protection. *Publication 53: Radiation Doses to Patients from Radiopharmaceuticals, Annals of the ICRP 18 No 1-4*. Pergamon Press, Oxford, England (1987).
- International Commission on Radiological Protection (ICRP). *Publication 60: Annals of the ICRP 21(1-3). 1990 Recommendations of the International Commission on Radiological Protection*. Pergamon Press, Oxford (1991).
- Johns HE, Cunningham JR. *The Physics of Radiology, 4th Edition*. Charles C Thomas, Springfield, IL (1983).

- Jones D, Wall B. *NRPB Report 186: Organ Doses from Medical X-Ray Examinations Calculated Using Monte Carlo Techniques*. National Radiological Protection Board, Chilton, UK (1985).
- Klevenhagen SC. "The built-up of backscatter at the energy range 1 mm Al to 8 mm Al HVL." *Physics in Medicine and Biology* 27: 1035-1043 (1982).
- Koedooder K, Venema HW. "Filter materials for dose reduction in screen-film radiography." *Physics in Medicine and Biology* 31: 585-600 (1986).
- Le Heron J. "Estimation of effective dose to the patient during medical x-ray examinations from measurements of the dose-area products." *Physics in Medicine and Biology* 37: 2117-2126 (1992).
- Lindskoug BA. "The reference man in diagnostic radiology dosimetry." *British Journal of Radiology* 65: 431-437 (1992).
- Manny EF, Burkhart RL. *Measurement Techniques for Use With Technique/Exposure Guides*. HHS Publication (FDA) 85-8248, Rockville, MD (1985).
- McParland BJ. "A study of patient radiation doses in interventional radiological procedures." *British Journal of Radiology* 71: 175-185 (1998).
- Merriam GR Jr, Focht EF. "A clinical study of radiation cataracts in relationship to dose." *American Journal of Roentgenology* 77: 759-785 (1957).
- Metz CE, Doi K. "Transfer function analysis of radiographic imaging systems." *Physics in Medicine and Biology* 24: 1079-1106 (1979).
- Nagel HD. "Comparison of performance characteristics of conventional and K-edge filters in general diagnostic radiology." *Physics in Medicine and Biology* 34: 1269-1287 (1989).
- National Academy of Sciences. *BEIR V: Health Effects of Exposure to Low Levels of Ionizing Radiation*. National Academy Press, Washington DC (1990).
- National Council on Radiation Protection and Measurements. *Report No. 80: Induction of Thyroid Cancer by Ionizing Radiation*. National Council on Radiation Protection and Measurements, Bethesda, MD (1985).
- National Council on Radiation Protection and Measurements. *Report No. 100: Exposure of the US Population from Diagnostic Medical Radiation*. National Council on Radiation Protection and Measurements, Bethesda, MD (1989).
- Norbash AM, Busick D, Marks MP. "Techniques for reducing interventional neuroradiologic skin dose: tube position rotation and supplemental beam filtration." *American Journal of Neuroradiology* 17: 41-49 (1996).

- Nuclear Regulatory Commission. *10CFR19: Notices, Instructions, and Reports to Workers: Inspection and Investigations*. Nuclear Regulatory Commission, Washington, DC (1995a).
- Nuclear Regulatory Commission. *10CFR20: Standards for Protection Against Radiation*. Nuclear Regulatory Commission, Washington, DC (1995b).
- Padovani R, Contento G, Fabretto M, Malisan MR, Barbina V, Gozzi G. "Patient doses and risks from diagnostic radiology in North-east Italy." *British Journal of Radiology* **60**: 155-165 (1987).
- Patrocínio HJ, Bissonnette JP, Bussière MR, Schreiner LJ. "Limiting values of backscatter factors for low-energy x-ray beams." *Physics in Medicine and Biology* **41**: 239-253 (1996).
- Persliden J, Carlsson G. "Energy imparted to water slabs by photons in energy range 5-300 keV. Calculations using Monte Carlo photon transport model." *Physics in Medicine and Biology* **29**: 1075-1088 (1984).
- Puskin JS, Nelson CB. "Estimates of radiogenic cancer risks." *Health Physics* **69**: 93-101 (1996).
- Rajapakshe R, Shalev S. "Noise analysis in real-time portal imaging. I. Quantization noise." *Medical Physics* **21**: 1263-1268 (1994).
- Roehrig H, Nudelman S, Fisher HD, Frost MM, Capp MP. "Photoelectronic imaging for radiology." *IEEE Transactions on Nuclear Science* **28**: 190-204 (1981).
- Rubin P, Casarett GW. *Clinical Radiation Pathology. Vol I and II*. WB Saunders Philadelphia, PA (1968).
- Rudin S, Bednarek DR. "Non-hardening x-ray beam attenuating filters." Abstract, AAPM Annual Meeting Program. *Medical Physics* **20**:918 (1993).
- Sandor T, Natt P. "Effect of radiographic magnification on image contrast of blood vessels." *American Journal of Roentgenology* **134**: 159-192 (1980).
- Sandrik JM, Wagner RF. "Absolute measures of physical image quality: measurement and application to radiographic magnification." *Medical Physics* **9**: 540-549 (1982).
- Shleien B (editor). *The Health Physics and Radiological Health Handbook*. Scinta, Inc, Silver Spring, MD (1992).
- Shope TB. "Radiation-induced skin injuries from fluoroscopy." *Radiographics* **16**: 1195-1199 (1996).

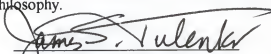
- Shrimpton P, Wall B. "An evaluation of the Diamantor transmission ionization chamber in indicating exposure-area product ($R \text{ cm}^2$) during diagnostic radiological examinations." *Physics in Medicine and Biology* 27: 871-878 (1982).
- Shrimpton PC, Jones DJ, Wall BF. "The influence of tube filtration and potential on patient dose during x-ray examinations." *Physics in Medicine and Biology* 33: 1205-1212 (1988).
- Shrimpton P, Wall B, Jones D, Fisher E. "The measurement of energy imparted to patients during diagnostic x-ray examinations using the Diamantor exposure-area product meter." *Physics in Medicine and Biology* 19: 1199-1208 (1984).
- Suleiman OH, Antonsen R, Conway B, McGrohan J, Rueter F, Slayton R. "Assessing patient exposure in fluoroscopy." *Radiation Protection and Dosimetry* 43:251-252 (1992).
- Tapiovaara MJ, Sandborg M. "Evaluation of image quality in fluoroscopy by measurements and Monte Carlo calculations." *Physics in Medicine and Biology* 40: 589-607 (1995).
- Thompson WM, Halvorsen RA, Gedgaudas RK, Kelvin FM, Rice RP, Woodfield S, Johnson GA, Hedlung LW, Jorgensen DB. "High kVp vs. low kVp for T-tube operative cholangiography." *Radiology* 146: 635-642 (1983).
- Trout ED, Kelley JP, Cathey GA. "The use of filters to control radiation exposure to the patient in diagnostic roentgenology." *American Journal of Roentgenology, Radium Therapy and Nuclear Medicine* 57: 946-963 (1952).
- Tucker M, Barnes G, and Chakraborty D. "Semi-empirical model for generating tungsten target x-ray spectra." *Medical Physics* 18: 211-218 (1991).
- United Nations Scientific Committee on the Effects of Atomic Radiation (UNSCEAR). *Report to the General Assembly: Sources, Effects and Risks of Ionizing Radiation*. United Nations, New York, NY (1988).
- United Nations Scientific Committee on the Effects of Atomic Radiation (UNSCEAR). *1993 Report to the General Assembly: Medical Radiation Exposures*. United Nations, New York, NY (1993).
- Vano E, Arranz L, Sastre JM, Moro C, Ledo A, Garate MT, Minguez I. "Dosimetric and radiation protection considerations based on some cases of patient skin injuries in interventional cardiology." *British Journal of Radiology* 71: 510-516 (1998).
- Wagner, L. "Absorbed dose in imaging: Why measure it?" *Radiology* 178: 622-623 (1991).

- Wagner LK, Cohen G, Wong WH, Amtey SR. "Dose efficiency and the effects of resolution and noise on detectability in radiographic mammography." *Medical Physics* 8: 24-32 (1981a).
- Wagner LK, Cohen G, Wong WH, Amtey SR. "Resolution in radiographic magnification." *Medical Physics* 8: 382-384 (1981b).
- Wagner LK, Eifel PJ, Geise RA. "Potential biological effects following high x-ray dose interventional procedures." *J of Vasc Int Rad* 5: 71-84 (1994).
- Wall B, Fisher E, Paynter R, Hudson A, Bird P. "Doses to patients from phantomographic and conventional dental radiography." *British Journal of Radiology* 52: 727-734 (1979).
- Wall B, Harrison R, Spiers F. *ISPM Report #53: Patient Dosimetry Techniques in Diagnostic Radiology*. The Institute of Physical Science in Medicine, York, England (1988).


BIOGRAPHICAL SCHETCH

Nikolaos A. Gkanatsios was born in Greece in 1970 to Argyrios and Anastasia Gkanatsios. He came to the United States in 1988 and earned a bachelor's degree in nuclear engineering from Worcester Polytechnic Institute, Worcester, MA, in 1992. The same year he joined the graduate program of the University of Florida, where he earned his Master of Science in medical physics in August of 1995. He was accepted as a Ph.D candidate in the Department of Nuclear and Radiological Sciences at the University of Florida. Nikolaos Gkanatsios earned his Doctor of Philosophy degree from the University of Florida in 1998.


I certify that I have read this study and that in my opinion it conforms to acceptable standards of scholarly presentation and is fully adequate, in scope and quality, as a dissertation for the degree of Doctor of Philosophy.


James S. Tulenko, Chair
Professor of Nuclear and Radiological
Engineering


I certify that I have read this study and that in my opinion it conforms to acceptable standards of scholarly presentation and is fully adequate, in scope and quality, as a dissertation for the degree of Doctor of Philosophy.


Walter Huda, Cochair
Associate Professor of Nuclear and
Radiological Engineering


I certify that I have read this study and that in my opinion it conforms to acceptable standards of scholarly presentation and is fully adequate, in scope and quality, as a dissertation for the degree of Doctor of Philosophy.


Wesley E. Bolch
Associate Professor of Nuclear and
Radiological Engineering

I certify that I have read this study and that in my opinion it conforms to acceptable standards of scholarly presentation and is fully adequate, in scope and quality, as a dissertation for the degree of Doctor of Philosophy.


Janice C. Honeyman
Associate Professor of Computer and
Information Science and Engineering

I certify that I have read this study and that in my opinion it conforms to acceptable standards of scholarly presentation and is fully adequate, in scope and quality, as a dissertation for the degree of Doctor of Philosophy.


Keith R. Peters
Associate Professor of Radiology

I certify that I have read this study and that in my opinion it conforms to acceptable standards of scholarly presentation and is fully adequate, in scope and quality, as a dissertation for the degree of Doctor of Philosophy.




Irvin F. Hawkins
Professor of Radiology

This dissertation was submitted to the Graduate Faculty of the College of Engineering and to the Graduate School and was accepted as partial fulfillment of the requirements for the degree of Doctor of Philosophy.

December, 1998



Winfred M. Phillips
Dean, College of Engineering



M.J. Ohanian
Dean, Graduate School

LD
1780
199₈
.G539

